

A Far Ultraviolet Spectroscopic Explorer Survey of Interstellar Molecular Hydrogen in the Galactic Disk

J. Michael Shull, Charles W. Danforth

*Department of Astrophysical and Planetary Sciences and CASA
University of Colorado, 389-UCB, Boulder, CO 80309*

Katherine L. Anderson

Green Mountain High School, Lakewood, CO 80228, USA

michael.shull@colorado.edu, charlesdanforth@gmail.com,
kalander@jeffcoschools.us

ABSTRACT

We report results from a *Far Ultraviolet Spectrographic Explorer (FUSE)* survey of interstellar molecular hydrogen (H_2) in the Galactic disk toward 139 O-type and early B-type stars at Galactic latitudes $|b| \leq 10^\circ$, with updated photometric and parallax distances. The H_2 absorption is measured using the far-ultraviolet Lyman and Werner bands, including strong R(0), R(1), and P(1) lines from rotational levels $J = 0$ and $J = 1$ and excited states up to $J = 5$ (sometimes $J = 6$ and 7). For each sight line, we report column densities N_{H_2} , N_{HI} , $N(J)$, $N_{\text{H}} = N_{\text{HI}} + 2N_{\text{H}_2}$, and molecular fraction, $f_{\text{H}_2} = 2N_{\text{H}_2}/N_{\text{H}}$. Our survey extends the 1977 *Copernicus* H_2 survey up to $N_{\text{H}} \approx 5 \times 10^{21} \text{ cm}^{-2}$. The lowest rotational states have excitation temperatures and rms dispersions, $\langle T_{01} \rangle = 88 \pm 20 \text{ K}$ and $\langle T_{02} \rangle = 77 \pm 18 \text{ K}$, suggesting that $J = 0, 1, 2$ are coupled to the gas kinetic temperature. Populations of higher- J states exhibit mean excitation temperatures, $\langle T_{24} \rangle = 237 \pm 91 \text{ K}$ and $\langle T_{35} \rangle = 304 \pm 108 \text{ K}$, produced primarily by UV radiative pumping. Correlations of f_{H_2} with $E(B - V)$ and N_{H} show a transition to $f_{\text{H}_2} \geq 0.1$ at $N_{\text{H}} \gtrsim 10^{21} \text{ cm}^{-2}$ and $E(B - V) \gtrsim 0.2$, interpreted with an analytic model of H_2 formation-dissociation equilibrium and attenuation of the far-UV radiation field by self-shielding and dust opacity. Results of this disk survey are compared to previous *FUSE* studies of H_2 in translucent clouds, at high Galactic latitudes, and in the Magellanic Clouds. Using updated distances to the target stars, we find average sightline values $\langle f_{\text{H}_2} \rangle = 0.20$ and $\langle N_{\text{H}}/E(B - V) \rangle = 6.07 \times 10^{21} \text{ cm}^{-2} \text{ mag}^{-1}$.

1. Introduction

Molecular hydrogen (H_2) is the most abundant molecule in the universe, constituting the majority of the interstellar molecular clouds that eventually form stars. Even though H_2 plays an important role in the chemistry of the interstellar medium (ISM), many questions remain about its distribution, formation, and destruction in both diffuse and protostellar clouds. The *Copernicus* satellite in the 1970s provided the first large-scale survey of interstellar H_2 (Spitzer et al. 1974; Savage et al. 1977). With the 1999 launch of the *Far Ultraviolet Spectrographic Explorer (FUSE)* satellite, astronomers once again gained access to the far-ultraviolet (FUV) wavelengths needed to study H_2 in its resonance absorption lines. This survey extends these studies to 139 OB-type stars, many of them fainter and more distant than observed by *Copernicus*.

From the inception of the *FUSE* mission, H_2 studies were part of the science plan. The *FUSE* satellite, its mission, and its on-orbit performance were described in Moos et al. (2000) and Sahnou et al. (2000).

Initial FUSE studies of H₂ were reported in papers from the Early Release Observations (Snow et al. 2000; Shull et al. 2000). Later studies included a survey of 70 sight lines to OB stars probing H₂ in the Large and Small Magellanic Clouds (Tumlinson et al. 2002), surveys of 38 sight lines through translucent clouds (Rachford et al. 2002, 2009), studies of chemical relationships of H₂ with other molecules (CO, CH, CH⁺, CN) and atomic species (Burgh et al. 2007; Sheffer et al. 2008; Jensen et al. 2010), and observations of H₂ in the low Galactic halo (Gillmon et al. 2006; Wakker 2006; Gillmon & Shull 2006). At high redshift, H₂ Lyman/Werner lines have been detected in damped Ly α absorbers (Noterdaeme et al. 2008; Jorgenson et al. 2014; Balashev et al. 2019).

We present the results of a *FUSE* survey of interstellar H₂ absorption in the Galactic disk, using transitions from the ground electronic state, $X^1\Sigma_g^+$, to excited electronic states, $B^1\Sigma_u^+$ (Lyman bands) and $C^1\Pi_u$ (Werner bands). These lines are rovibrational transitions from lower states (v_l, J_l) to upper states (v_u, J_u). In the cold, low-density ISM, essentially all the molecules are in the ground vibrational state ($v_l = 0$). Absorption lines were observed up to $J_l = 5 - 6$ and occasionally $J_l = 7$. Because the wavefunction for the homonuclear H₂ is anti-symmetric under interchange of the identical (fermionic) protons, the even-parity rotational states ($J = 0, 2, 4, \dots$) have total nuclear spin $S = 0$ (spin anti-symmetric para-H₂) while odd-parity states ($J = 1, 3, 5, \dots$) have $S = 1$ (spin-symmetric ortho-H₂). The statistical weights of these states are $g_J = (2S + 1)(2J + 1)$, with odd- J states having a factor of three higher weight. Absorption bands leading to the upper level are identified by changes in vibrational state ($v_u - v_l$) and rotational angular momentum ($J_u - J_l$). The upper electronic state ($^1\Sigma_u^+$) of the Lyman bands has angular momentum $\Lambda = 0$ along the internuclear axis. Dipole-allowed changes in rotational state ($\Delta J = \pm 1$) are denoted as R-branch ($J_u = J_l + 1$) and P-branch ($J_u = J_l - 1$). The upper electronic state ($^1\Pi_u$) of Werner bands has $\Lambda = 1$, allowing a Q-branch ($J_u = J_l$) in addition to the R and P branches.

We observed multiple lines in the Lyman and Werner bands in the FUV (930–1126 Å) towards background OB stars located near the Galactic disk plane at $|b| \leq 10^\circ$. Several target stars were outside this latitude range, but all show strong H₂ absorption. Lines from $J = 0$ and $J = 1$ nearly always exhibit damping wings. Analysis of absorption-line equivalent widths and damping wings yields column densities, $N(J)$, in individual rotational states. **Figure 1** shows a *FUSE* spectrum of the sight line to HD 46150, an O5 Vf star at 1.5 kpc distance and $E(B - V) = 0.45$, with the Lyman and Werner bands labeled including a close-up of the (4-0) Lyman band. The total H₂ column density, N_{H_2} , is found by summing over all observed J states. Typically, 98% to 99% of the molecules reside in the lowest two levels, $J = 0$ and $J = 1$.

Observations of H₂ column densities, the molecular fraction in diffuse clouds, and its rotational excitation provide diagnostics of diffuse ISM (Shull & Beckwith 1982). The excitation temperature, T_{01} , of the lowest rotational states (para-H₂ in $J = 0$ and ortho-H₂ in $J = 1$) is an approximate measure of the gas kinetic temperature. In many cases, the three lowest levels ($J = 0, 1, 2$) appear to be thermalized, with both T_{01} and T_{02} coupled to the kinetic temperature (Gry et al. 2002; Le Petit et al. 2006). In diffuse interstellar clouds, thermal equilibration requires sufficiently large gas densities for proton interchange collisions to produce ortho-para conversion between $J = 0$ and $J = 1$ (Dalgarno et al. 1973; Gerlich 1990). Column densities $N_{\text{H}_2} \geq 10^{18} \text{ cm}^{-2}$ are needed to produce strong self-shielding in absorption lines from the dissociating FUV radiation. The current observations show that both T_{01} and T_{02} provide estimates of the heating and cooling processes in the diffuse ISM. The excitation temperature, T_{exc} , of higher rotational states ($J = 3 - 6$) is influenced by the FUV radiation field, which excites and photodissociates H₂ (Jura 1974; Black & Dalgarno 1976). From *FUSE* data on these excited states, we compute temperatures, T_{24} and T_{35} , based on population ratios of $J = 2$ to 4 and $J = 3$ to 5, respectively.

Section 2 begins with a description of the OB-star sample and our methods of data acquisition and

analysis. Section 3 provides the survey results, including H_2 and H I column densities, molecular fractions, rotational excitation temperatures, and gas-to-dust ratio, $N_{\text{H}}/E(B - V)$. We also present a simple analytic model of the transition from H I to H_2 , including H_2 formation rates, FUV dissociation, self-shielding, and dust opacity. The transition occurs at $f_{\text{H}_2} \approx 0.1$ at dust optical depth $\tau_d \approx 1$ and is controlled primarily by the ratio of FUV flux to gas density. The lowest rotational states exhibit mean excitation temperatures $\langle T_{01} \rangle = 88 \pm 20$ K and $\langle T_{02} \rangle = 77 \pm 18$ K. Higher rotational states ($J \geq 3$) have larger excitation temperatures, $T_{\text{exc}} \approx 150 - 650$ K, arising from fluorescent cascade following FUV radiative excitation in the Lyman and Werner bands. Section 4 summarizes our findings, with comparisons to the *Copernicus* survey of H_2 (Savage et al. 1977) and the $N_{\text{H}}/E(B - V)$ ratio (Bohlin et al. 1978). The *FUSE* mean value for the Galactic disk, $\langle N_{\text{H}}/E(B - V) \rangle = (6.07 \pm 1.01) \times 10^{21} \text{ cm}^{-2} \text{ mag}^{-1}$, is lower than estimates from 21-cm/far-IR studies at high Galactic latitudes (Liszt 2014a,b), suggesting that gas and dust have different spatial distributions above the disk.

2. Data Acquisition and Reduction

2.1. FUSE Observations

The 139 targets in this survey were drawn primarily from *FUSE* programs designed to study OB stars and interstellar gas in the Milky Way. **Figure 2** shows the target distribution in Galactic longitude and latitude, with color coding for their distances. Most stars are O-type and early B-type (B0, B0.5) and generally more distant than those in the 1977 *Copernicus* survey. Many were part of *FUSE* science team projects to study O VI from hot gas in the Galactic disk (Bowen et al. 2008), interstellar D/H (Moos et al. 2002; Hoopes et al. 2003; Hébrard et al. 2005), and hot stars and their winds (Massa et al. 2003). Several stars were analyzed specifically for their interstellar H_2 (Shull et al. 2000; Snow et al. 2000).

Table 1 lists information on the 139 stellar targets and their observational characteristics. These stars have updated spectral types (SpT) and both photometric and *Gaia*-DR2 parallax distances determined by Shull & Danforth (2019) using new information from the Galactic O-star Spectroscopic Survey (Maíz Apellániz et al. 2004). The GOS project generated a large sample of O stars within several kiloparsecs of the Sun with updated spectral classification (Sota et al. 2011, 2014), together with digital photometry and optical-NIR dust extinction (Maíz-Apellániz & Barbá 2018). The first ten columns of Table 1 provide our internal target ID, star name, Galactic coordinates (ℓ , b), photometry (B and V magnitudes), color excess $E(B - V)$, SpT, and both photometric and parallax distances. The last two columns list the *FUSE* program ID and exposure time of the primary observation. In some cases, we used other *FUSE* observations to supplement or confirm our measurements. Footnotes explain the sources for photometry and distances.

All column densities are expressed in units of cm^{-2} and often quoted in logarithmic format ($\log N$). The total hydrogen column density, $N_{\text{H}} = N_{\text{HI}} + 2N_{\text{H}_2}$, is used to derive the molecular fraction, $f_{\text{H}_2} = 2N_{\text{H}_2}/N_{\text{H}}$, and explore its correlations with $E(B - V)$ and line-of-sight pathlength. Most H I column densities, N_{HI} , were taken from previous $\text{Ly}\alpha$ profile-fitting surveys (Shull & Van Steenberg 1985; Diplas & Savage 1994; Jenkins 2019) supplemented by a few individual $\text{Ly}\alpha$ measurements. **Table 2** presents our adopted values of N_{HI} and a comparison to previous measurements. We adopted N_{HI} in priority order of: (J19) 57 stars from Jenkins (2019); (DS94) 51 stars from Diplas & Savage (1994); (FM90) two stars from Fitzpatrick & Massa (1990); and three stars from other sources. A comparison between J19 and DS94 found generally good agreement, within 0.03 – 0.08 in $\log N$. Only seven sight lines differed by larger amounts (0.09 – 0.19). For 26 sight lines with no available no $\text{Ly}\alpha$ fits, we estimated N_{HI} from the scaling relation (Bohlin et al.

1978) of total hydrogen column density with color excess, $N_{\text{H}} = (5.8 \times 10^{21} \text{ cm}^{-2} \text{ mag}^{-1})E(B - V)$, where $N_{\text{HI}} = N_{\text{H}} - 2N_{\text{H}_2}$.

2.2. Data Analysis

The data analysis for this survey used numerous absorption lines from H_2 Lyman and Werner transitions between 930 - 1126 Å. Our methodology is identical to that used in the *FUSE* survey of H_2 in the LMC and SMC (Tumlinson et al. 2002), and we refer readers to that paper for details. We search for absorption lines from $J = 0 - 7$ and typically detect lines up to $J = 5$. Most lines exhibit shifts in wavelength (0.03–0.13 Å) with offsets determined by measuring narrow interstellar metal lines such as Ar I (1048.218 Å, 1066.660 Å), Fe II (1055.269 Å, 1063.177 Å, 1144.938 Å), Si II (1020.699 Å), P II (1152.818 Å), and other lines of Fe II, O I, N I. This procedure is similar to that employed by Tumlinson et al. (2002), Wakker (2006), and Gillmon et al. (2006). We also considered the R(0) lines of HD in its (3-0), (4-0), (5-0) bands at 1066.271 Å, 1054.286 Å and 1042.847 Å, respectively. However, the HD lines were often offset in velocity from H_2 , possibly because of its presence in only one of the components of the H_2 line profile.

The most accurate determinations of column densities N come from weak lines where equivalent width $W_\lambda \propto N$, or from strong lines with damping wings where $W_\lambda \propto N^{1/2}$. In both limits, the column density can be determined without knowledge of the Doppler parameter (b). Between these two regimes, from line-center optical depth $\tau_0 \approx 1$ up to $\tau_{\text{damp}} \approx 10^{3-4}$, one must employ curve-of-growth (CoG) methods¹ that require an estimation of b . The linear relation between W_λ and N and the onset of line saturation are measured by optical depth at line center,

$$W_\lambda = \left(\frac{\pi e^2}{m_e c} \right) \frac{N f \lambda^2}{c} = (88.53 \text{ Å}) N_{15} \lambda_{1000} \left[\frac{f \lambda}{10 \text{ Å}} \right] \quad (1)$$

$$\tau_0 = \left(\frac{\pi e^2}{m_e c} \right) \frac{N f \lambda}{\sqrt{\pi} b} = (1.497) N_{15} b_{10}^{-1} \left[\frac{f \lambda}{10 \text{ Å}} \right]. \quad (2)$$

Here, we scaled to column density $N = (10^{15} \text{ cm}^{-2})N_{15}$, Doppler parameter $b = (10 \text{ km s}^{-1})b_{10}$, and wavelength $\lambda = (1000 \text{ Å})\lambda_{1000}$. Line strengths are normalized to $f\lambda = 10 \text{ Å}$, a typical value for many lines in the Lyman and Werner bands.

Equivalent widths of the highly saturated lines from $J = 2$ and $J = 3$ are frequently quite large, with dimensionless values $W_\lambda/\lambda \approx (1 - 3) \times 10^{-4}$. On the flat portion of the CoG, these widths are primarily determined by the effective b -value, with asymptotic values $W_\lambda/\lambda \approx (2b/c)[\ln(\tau_0/\ln 2)]^{1/2}$. As shown in the CoG suite prepared by McCandliss (2003), strong lines on the equivalent width plateau often require Doppler parameters, $b = 10 - 20 \text{ km s}^{-1}$, much higher than the expected thermal values, $b_{\text{th}} = (2kT/m)^{1/2} \approx (0.9 \text{ km s}^{-1})T_{100}^{1/2}$, for H_2 at temperatures $T = (100 \text{ K})T_{100}$. They likely result from velocity components within the absorber and micro-turbulence. Several previous studies (Jenkins & Peimbert 1997; Gry et al. 2002; Lacour et al. 2005) suggested that b -values increase with rotation level. Although we found several

¹The equivalent width (W_λ) of a saturated absorption line rises slowly with increasing column density N and line-center optical depth τ_0 . As shown by asymptotic analysis, $W_\lambda/\lambda \approx (2b/c)[\ln(\tau_0/\ln 2)]^{1/2}$ for large τ_0 and a Doppler-broadened Gaussian velocity profile, $\phi(v) \propto \exp(-v^2/b^2)$. Draine (2011) noted that this formula is accurate to 5% for $1.254 < \tau_0 < \tau_{\text{damp}}$, up to the onset of damping wings. Inverting this relation, we find $\tau_0 \approx (0.693) \exp[(W_\lambda/\lambda)^2/(2b/c)^2]$. Clearly, τ_0 and N are exponentially sensitive to measurements of W_λ and b . When equivalent widths of the accessible lines lie on a flat CoG, errors can exceed ± 0.40 for $\log N = 16 - 17$ and ± 0.50 for $\log N = 17 - 19$.

cases where the higher- J lines required larger b -values, we saw no evidence of a uniform trend in the current survey or in our study of H_2 in the Magellanic Clouds (Tumlinson et al. 2002).

For absorbers with $N(J) \leq 10^{18} \text{ cm}^{-2}$, we measured equivalent widths of the accessible H_2 lines, producing a CoG that yields a b value and column densities, $N(J)$, in rotational states $J = 0 - 5$, and occasionally $J = 6$ and $J = 7$. **Table 3** lists column densities in $J = 0 - 6$ and the inferred b -value when measurable. Most column densities range from $\log N(J) \approx 19.0 - 21.5$ in $J = 0 - 1$ to $\log N(J) \approx 13.7 - 15.5$ in $J = 4 - 6$. In 48 targets, we found detectable column densities in $J = 6$. For other sight lines, we quote upper limits, which range from $\log N(6) < 13.85 - 14.40$ depending on the data quality. Six targets had detectable column densities in $J = 7$, described in footnote (a) to Table 3.

For absorbers with damping wings in $R(0)$, $R(1)$, and $P(1)$ lines, we fitted line profiles to derive $N(0)$ and $N(1)$, a technique used in previous studies of H_2 (Savage et al. 1977; Tumlinson et al. 2002; Jenkins 2019). The errors on these column densities depend on data quality, both the signal-to-noise (S/N) and our ability to define the continuum on either side of the blended $R(0)$, $R(1)$, $P(1)$ complex (see the bottom panel of Figure 1 for an example). Based on our experience with fitting damping wings, we define three levels of S/N ratio and corresponding errors, $\sigma_{\log N}$, on $\log N(0)$ and $\log N(1)$: (1) $S/N \geq 15$ (0.03–0.05 errors); (2) $5 \leq S/N \leq 15$ (0.05–0.10); and (3) $S/N \leq 5$ (0.10–0.20).

A key aspect of our analysis software is the rapid and consistent measurement of as many individual H_2 absorption lines as possible in each sight line. We then use CoGs to derive column densities for the undamped lines in $J \geq 2$. The programs are written to consistently measure all available (unblocked) absorption lines in the spectra. In many instances, lines from $J = 2$ and $J = 3$ were strongly saturated, with equivalent widths lying on the flat (Doppler-broadened) portion of the CoG where column densities are difficult to determine. In this case, W_λ depends primarily on the Doppler parameter, which is often much larger than the thermal value because of multiple velocity components. The process of measuring the numerous lines that enter the CoG fitting cannot be automated completely. Our software requires the user to decide on a line-by-line basis which H_2 lines will be fitted. We ignore H_2 lines in spectral regions near strong interstellar absorption or bright geocoronal emission. For example, the H_2 Lyman (6-0) band is obscured by strong damping wings of the interstellar $\text{Ly}\beta$ line (1025.722 Å), and the Lyman (5-0) band lies among the resonance absorption lines of C II (1036.337 Å) and C II* (1037.018 Å). We neglect these bands except when the higher- J lines are separated from the intervening absorption.

For the higher- J lines, the software steps through the expected positions of the lines, band by band, shifted by the approximate velocity offset from the metal lines. Going through each complete band of lines consecutively, the routine displays the area where a line should appear. If the line is present and unblended with any other transitional or metal line, it is fitted to a Gaussian, and its equivalent width, errors, wavelength, full width half maximum, and velocity offset are entered into a table. The Lyman (6-0) band is typically omitted, and the Lyman (5-0) band is measured only partially, because of overlap with C II $\lambda 1036$ absorption. In these bands, lines that are observable and undistorted are measured and included in the tables. This routine is executed for each detector segment, creating four tables of data, with maximum redundancy over the critical range between 1000 Å and 1126 Å. The four tables are then merged, and a CoG is generated with a single Doppler parameter. An error routine is run to calculate the smallest errors over a range of b -values. Asymmetric error bars are generated for b and column densities.

As noted above, column densities from $J = 2$ and $J = 3$ are difficult to measure, because most of their lines are highly saturated. To alleviate CoG uncertainties and determine an accurate b -value it is helpful to measure the weakest available lines, with strengths $f\lambda \leq 4$ Å. These weak lines are useful in anchoring the

CoG for more saturated lines. Unfortunately, we were unable to measure the weakest lines from $J = 2$: (0-0) P(2) at 1112.495 Å ($f\lambda = 0.740$ Å); (0-0) R(2) at 1110.120 Å ($f\lambda = 1.199$ Å); and (1-0) R(2) 1094.244 Å ($f\lambda = 4.016$ Å). These lines are blended with (0-0) P(1), (0-0) R(3), and (1-0) P(1), respectively. For $J = 3$, we were unable to measure the two weakest lines: (0-0) P(3) at 1115.896 Å ($f\lambda = 0.784$ Å) blended with (0-0) R(4) at 1116.013 Å, and (0-0) R(3) at 1112.584 Å ($f\lambda = 1.135$ Å) blended with (0-0) P(2) at 1112.495 Å. The weakest line that could be measured was (1-0) P(3) at 1099.788 Å ($f\lambda = 2.639$ Å). For $J = 4$, the weakest lines, (0-0) P(4) at 1120.247 Å ($f\lambda = 0.808$ Å) and (0-0) R(4) at 1116.013 Å ($f\lambda = 1.116$ Å), are blended with (0-0) P(3) 1115.896 Å and (0-0) R(5) 1120.300 Å, respectively. In some cases we were able to separate (0-0) P(4). In general the most accessible lines were the P(4) lines in (1-0), (2-0), (3-0), (4-0), (5-0), (7-0) bands and the R(4) lines in (3-0), (4-0), (5-0) bands. For $J = 5$, we found a sufficient number of lines with a range of strengths for a reliable CoG.

A systematic uncertainty in our results comes from the possibility of multiple components in the absorption lines caused by more than one cloud in the line of sight. Many spectra (~ 40 sight lines) have velocity components that make the neighboring lines visually identifiable, but not separable without careful profile fitting using other information from higher resolution optical lines. Some absorbers in this survey have components that are not resolvable; those lines are treated as though they are a single component. The spectra of 15 targets exhibited obvious multiple components separated by $\Delta v \geq 20$ km s $^{-1}$. We measured those individually using a double Voigt profile fit. The components have their values entered into separate data tables, enabling us to generate two CoGs with individual b values. In these cases, we report the total column densities measured for saturated lines or lines without visible structure and individual column densities where components are measurable. Lines at $J \leq 3$ are often saturated and too strong to show component structure. These lines are fitted as a single component, and a total column density is returned.

3. Results

3.1. Molecular Abundances

The *FUSE* survey finds H₂ everywhere in the disk of the galaxy (**Figure 2**) at typical Galactic latitudes $|b| < 4^\circ$. The H₂ column density rises rapidly above $N_{\text{H}_2} \geq 10^{19.5}$ cm $^{-2}$ for sight lines with color excess $E(B - V) \gtrsim 0.2$, as illustrated in **Figure 3**. The molecular fraction, $f_{\text{H}_2} = 2N_{\text{H}_2}/N_{\text{H}}$, quantifies the number of hydrogen nuclei bound into H₂ molecules, where $N_{\text{H}} = N_{\text{HI}} + 2N_{\text{H}_2}$ is the total hydrogen column density. Later in this section, we will adopt $N_{\text{H}_2} = 10^{19.5}$ cm $^{-2}$ and $f_{\text{H}_2} = 0.1$ as nominal values of the atomic-to-molecular transition in the absorbing gas. With the exception of sight lines toward HD 3827 ($\log N_{\text{H}_2} = 17.48$), HD 201638 ($\log N_{\text{H}_2} = 18.23$), and HD 92554 ($\log N_{\text{H}_2} = 18.93$), all targets in the survey have $\log N_{\text{H}_2} \geq 19.0$. **Table 4** summarizes the column densities (N_{HI} , N_{H_2} , N_{H}) together with the molecular fractions and rotational excitation temperatures inferred from populations in levels $J = 0 - 5$. Rotational excitation temperatures, T_{01} , T_{02} , T_{24} , and T_{35} , are discussed further in Sections 3.4 and 3.5.

The atomic-to-molecular transition arises from both H₂ self-shielding in optical thick lines and dust attenuation of the dissociating FUV radiation (Browning et al. 2003; Krumholz et al. 2008, 2009; Sternberg et al. 2014). The *Copernicus* survey of 61 stellar targets (Savage et al. 1977) noted that f_{H_2} rises rapidly above 1% at $E(B - V) \geq 0.08$ and $N_{\text{H}} \geq 5 \times 10^{20}$ cm $^{-2}$. A transition to $f_{\text{H}_2} = 0.1$ appeared at lower hydrogen column densities ($\log N_{\text{H}} \approx 20.4$) in sight lines at high Galactic latitude (Gillmon et al. 2006). In the lower-metallicity LMC and SMC (Tumlinson et al. 2002; Browning et al. 2003) the transition shifted to higher column densities ($\log N_{\text{H}} \approx 21.3 - 22.0$), consistent with models with lower metallicity but a larger

ratio of FUV radiation to gas density. A lower grain abundance, owing to fewer refractory heavy elements, will reduce the H_2 formation rate. It also allows deeper penetration of FUV photons into the cloud, resulting in more H_2 dissociation. These effects are discussed further in Section 3.3.

Figure 4 presents the distributions of molecular fraction vs. $E(B - V)$ and N_{H} for 139 targets in the *FUSE* survey. **Figure 5** plots mean values of f_{H_2} and hydrogen density $n_{\text{H}} = N_{\text{H}}/D$ along the sight lines vs. target distance D . These averages were evaluated as $\langle n_{\text{H}} \rangle = \sum N_{\text{H}} / \sum D$ and $\langle f_{\text{H}_2} \rangle = \sum 2N_{\text{H}_2} / \sum [N_{\text{HI}} + 2N_{\text{H}_2}]$. Both parallax and photometric distance are shown in the figure, with error bars reflecting formal parallax uncertainties from *Gaia*-DR2. With many sight lines to bright OB stars ($D \leq 2$ kpc), the *Copernicus* survey showed an increase of $f_{\text{H}_2} \geq 0.01$ at $E(B - V) \geq 0.08$ (Savage et al. 1977). The *FUSE* survey includes more distant sight lines, with column densities up to $\log N_{\text{H}} \approx 21.65$. We found a transition at $f_{\text{H}_2} \geq 0.1$ at $E(B - V) \gtrsim 0.2$, $N_{\text{H}} \gtrsim 10^{21} \text{ cm}^{-2}$ and $N_{\text{H}_2} \gtrsim 10^{19.5} \text{ cm}^{-2}$. The molecular fractions rise from $f_{\text{H}_2} \approx 1\%$ up to 40-75% in translucent sight lines with $\log N_{\text{H}} \approx 21.40$ to 21.65. Using new photometric distances toward 129 stars at $D_{\text{phot}} \leq 5$ kpc, we find a sightline-averaged hydrogen density $\langle n_{\text{H}} \rangle = 0.50 \text{ cm}^{-3}$ and molecular fraction $\langle f_{\text{H}_2} \rangle = 0.20$. These mean values shift toward higher values (**Table 5**) in sub-samples with $D_{\text{phot}} \leq 2$ kpc, owing to bias in distant targets that avoid heavily reddened gas. For stars at $D \leq 2$ kpc, $\langle n_{\text{H}} \rangle = 0.81 \text{ cm}^{-3}$ and molecular fraction $\langle f_{\text{H}_2} \rangle = 0.27$.

3.2. Hydrogen Gas vs. Extinction: $N_{\text{H}}/E(B - V)$ Ratio

The optical extinction along Galactic sight lines is often taken to be proportional to the dust column density, and therefore to the gas column density. This “gas-to-dust ratio” assumes a homogeneous mixture of interstellar hydrogen and grains, which may be a good assumption for most regions of the diffuse ISM. Deviations can be produced by changes in the grain size distribution and other physical properties that arise within dark clouds such as ρ Oph (Bohlin et al. 1978; Green et al. 1992) or in regions where shock waves have sputtered or destroyed some of the grains (Seab & Shull 1983). The total hydrogen column density, $N_{\text{H}} = N_{\text{HI}} + 2N_{\text{H}_2}$, is often compared to dust content through its ratio to color excess, $N_{\text{H}}/E(B - V)$, derived from UV surveys of H I ($\text{Ly}\alpha$) and H_2 toward early-type stars (Bohlin et al. 1978; Savage et al. 1977).

Our *FUSE* survey of the Milky Way disk should be more robust, with more stellar sight lines, updated O-star photometry and SpTs from the GOS survey, and newly derived values of $E(B - V)$ and target distances (Shull & Danforth 2019). **Figure 6** shows the distribution of $N_{\text{H}}/E(B - V)$ vs. $E(B - V)$. For 129 stars at $D \leq 5$ kpc, we find a mean ratio, $\langle N_{\text{H}}/E(B - V) \rangle = (6.07 \pm 1.01) \times 10^{21} \text{ cm}^{-2} \text{ mag}^{-1}$ with (rms) variations shown as blue wash. A sub-sample of 56 stars at $D \leq 2$ kpc (Table 5) has $\langle N_{\text{H}}/E(B - V) \rangle = 6.00 \times 10^{21} \text{ cm}^{-2} \text{ mag}^{-1}$. Both values are slightly above the values $5.8 \times 10^{21} \text{ cm}^{-2} \text{ mag}^{-1}$ in the *Copernicus* survey of 75 stars (Bohlin et al. 1978) and $5.94 \times 10^{21} \text{ cm}^{-2} \text{ mag}^{-1}$ in the *FUSE* survey of 38 translucent sight lines with $A_V \approx 0.5 - 4.7$ (Rachford et al. 2009).

Recent studies find a larger ratio when N_{HI} is measured from 21-cm emission and $E(B - V)$ is inferred from all-sky maps (Schlegel et al. 1998; Schlafly & Finkbeiner 2011) of far-infrared (FIR) dust emission from *IRAS* and *COBE/DIRBE*. Liszt (2014a,b) found $N_{\text{HI}}/E(B - V) = 8.3 \times 10^{21} \text{ cm}^{-2} \text{ mag}^{-1}$ in high-latitude sight lines ($|b| > 20^\circ$) with low extinction, $0.015 < E(B - V) < 0.075$. Lenz et al. (2017) found a similar large value, $8.8 \times 10^{21} \text{ cm}^{-2} \text{ mag}^{-1}$. These studies used only H I, but as the authors comment, corrections for H_2 are normally small for $E(B - V) < 0.08$.

We investigated whether sight lines with low $E(B - V)$ have different dust-to-gas ratios in the UV surveys. For 25 stars with $0.01 \leq E(B - V) \leq 0.08$ in the *Copernicus/IUE* survey (Bohlin et al. 1978) the

mean ratio is $4.0 \times 10^{21} \text{ cm}^{-2} \text{ mag}^{-1}$. For the 21 stars in our *FUSE* survey with $E(B - V) \leq 0.25$, we find a mean ratio $N_{\text{H}}/E(B - V) = 5.83 \times 10^{21} \text{ cm}^{-2} \text{ mag}^{-1}$. We omitted one outlier (HD 3827) with $\log N_{\text{H}} = 20.55$, with an uncertain $E(B - V) \approx 0.02$, and a high ratio $N_{\text{H}}/E(B - V) \approx 17 \times 10^{21} \text{ cm}^{-2} \text{ mag}^{-1}$. Located at photometric distance $D_{\text{phot}} \approx 1.88 \text{ kpc}$, HD 3827 lies 700 – 800 pc below the Galactic plane at $b = -23.21^\circ$. Its color excess, $E(B - V) = 0.02$, was based on magnitudes $B = 7.76$ and $V = 8.01$ (Deutschman et al. 1976) and intrinsic color $(B - V)_0 = -0.27$. Jenkins (2019) listed $E(B - V) = 0.05$ for this star, based on $B = 7.76$ and $V = 7.95$, which would reduce the ratio to $7 \times 10^{21} \text{ cm}^{-2} \text{ mag}^{-1}$.

The difference between the two techniques (UV absorption and radio/FIR emission) appears to be an effect only seen at high Galactic latitudes (Liszt 2014b; Hensley & Draine 2021). Elevated ratios from UV data do not appear toward disk stars with low $E(B - V)$. We suggest that the high ratios in 21-cm/FIR measurements result from different distributions of gas and dust above the disk. Dust grains are produced by stars in the disk and grow in the ISM through accretion of refractory elements. Some grains are transported above the disk plane by radiation pressure and supernova-driven outflows. Other grains may settle gravitationally into lower scale-height distributions, separating from the high-latitude H I. Dust at high latitudes may also come into contact with hot coronal gas at 10^{6-7} K and experience erosion by thermal sputtering and destruction by fast interstellar shock waves (Jones et al. 1996; Slavin et al. 2004). In hot, low-density halo gas, grain lifetimes from sputtering are $t_{\text{sp}} \approx (1 \text{ Gyr})(10^{-3} \text{ cm}^{-3}/n_e)$. Thus, the 21-cm and far-IR surveys at $|b| > 20^\circ$ likely probe systematically lower dust-to-gas ratios.

3.3. Atomic to Molecular Transition

As we will describe, the molecular transition from H I to H_2 is consistent with models involving H_2 self-shielding and efficient H_2 formation by atomic processes on grain surfaces (Hollenbach et al. 1971; Jura 1975a,b; Shull & Beckwith 1982). In equilibrium, the abundance ratio, $n_{\text{H}_2}/n_{\text{H}}$, can be expressed as a balance between H_2 formation and photo-dissociation. For number densities n_{HI} , n_{H_2} , and total hydrogen n_{H} , molecule formation occurs at a rate per unit volume, $Rn_{\text{H}}n_{\text{HI}}$. The total hydrogen density serves as a proxy for dust grains, whose surfaces are catalysts for H_2 formation. The coefficient R depends on the dust-to-gas ratio, metallicity, and atom-grain collisional rates, and it likely varies with gas temperature, grain temperature, and surface physics (Hollenbach & McKee 1979).

Previous studies (Browning et al. 2003; Krumholz et al. 2008, 2009; Sternberg et al. 2014; Bialy & Sternberg 2016) analyzed the molecular transition with radiative transfer. Here, we present a simple analytic description of the transition (at $f_{\text{H}_2} \approx 0.1$) tied directly to parameters that control the H_2 equilibrium between formation and destruction and the attenuation of FUV flux by H_2 self-shielding and dust opacity. In equilibrium,

$$n_{\text{HI}} n_{\text{H}} R = (f_{\text{diss}} G \beta_0) n_{\text{H}_2} S_{\text{H}_2} e^{-\tau_d}, \quad (3)$$

where β_0 is the average unshielded absorption rate of H_2 in the Lyman and Werner bands. For the local ISM, Jura (1974) estimated $\beta_0 = 5 \times 10^{-10} \text{ s}^{-1}$ with $f_{\text{diss}} \approx 0.11$. With updated line-dissociation data and models of self-shielding, Draine & Bertoldi (1996) found a mean fraction $\langle f_{\text{diss}} \rangle \approx 0.15$ for all H_2 absorptions inside the cloud. The parameter G allows for local elevation of the FUV radiation relative to its average value (Habing 1968), τ_d is the dust optical depth at 930–1130 Å, and the factor S_{H_2} accounts for H_2 self-shielding as the absorption lines become optically thick. For clarity, we define the *local* molecular fraction $f = 2n_{\text{H}_2}/n_{\text{H}}$, with $n_{\text{HI}} = (1 - f)n_{\text{H}}$. This fraction varies with depth into the cloud, whereas the *observed*

fraction, $f_{\text{H}_2} \equiv 2N_{\text{H}_2}/N_{\text{H}}$, depends on the integrated column densities. This leads to an expression,

$$\frac{f}{(1-f)} = \left(\frac{2n_{\text{H}}R}{f_{\text{diss}}\beta_0 G} \right) S_{\text{H}_2}^{-1} e^{\tau_d}. \quad (4)$$

Draine & Bertoldi (1996) provided a reliable approximation, $S_{\text{H}_2} = [N_{\text{H}_2}/10^{14} \text{ cm}^{-2}]^{-0.75}$, for $N_{\text{H}_2} \geq 10^{14} \text{ cm}^{-2}$. Combining $S_{\text{H}_2} = AN_{\text{H}_2}^{-0.75}$ ($A = 3.16 \times 10^{10} \text{ cm}^3/2$) with the approximation, $f \approx 2n_{\text{H}_2}/n_{\text{H}}$ for $f \leq 0.1$, we can write the local molecular density as

$$n_{\text{H}_2} = \left(\frac{Rn_{\text{H}}^2}{f_{\text{diss}}\beta_0 GA} \right) N_{\text{H}_2}^{0.75} e^{\tau_d}. \quad (5)$$

In a planar slab of constant density n_{H} , with column density N_{H_2} at a distance x into the absorber, we can write $n_{\text{H}_2} = dN_{\text{H}_2}/dx$. The dust optical depth is $\tau_d(x) \approx n_{\text{H}}x/N_d$, where $N_d \approx 4.5 \times 10^{20} \text{ cm}^{-2}$ at $\lambda \approx 1000 - 1100 \text{ \AA}$ (Draine 2011). This leads to a differential equation,

$$\frac{dN_{\text{H}_2}}{dx} = \left(\frac{Rn_{\text{H}}^2}{f_{\text{diss}}\beta_0 GA} \right) N_{\text{H}_2}^{0.75} e^{n_{\text{H}}x/N_d}, \quad (6)$$

with the analytic solution

$$N_{\text{H}_2} = \left(\frac{RN_d n_{\text{H}}}{4f_{\text{diss}}\beta_0 GA} \right)^4 \left[e^{\tau_d(x)} - 1 \right]^4. \quad (7)$$

The power-law approximation for $S_{\text{H}_2} \propto N_{\text{H}_2}^{-0.75}$ breaks down at low column densities, since $S_{\text{H}_2} = 1$ at $N_{\text{H}_2} < 10^{14} \text{ cm}^{-2}$. However, this only occurs in a small surface layer ($f_{\text{H}_2} < 10^{-5}$). Thus, the above expressions are valid up to to $f_{\text{H}_2} = 0.1$ for the H_2 absorbers observed with *FUSE*. The observed atomic-to-molecular transition at $N_{\text{H}_2} \approx 10^{19.5} \text{ cm}^{-2}$ occurs at dust optical depth $\tau_d = N_{\text{H}}/N_d$ given by

$$[e^{\tau_d} - 1] = (1.755) \left(\frac{N_{\text{H}_2}}{10^{19.5} \text{ cm}^{-2}} \right)^{1/4} G n_{30}^{-1} \left(\frac{3 \times 10^{-17} \text{ cm}^3 \text{ s}^{-1}}{R} \right) \left(\frac{4.5 \times 10^{20} \text{ cm}^{-2}}{N_d} \right) \quad (8)$$

Here, we adopted $f_{\text{diss}} = 0.15$ and $A/N_d = 7.03 \times 10^{-11} \text{ cm}^{1/2}$ for metallicities and grain opacities in the local ISM. We scaled the cloud density to $n_{\text{H}} = (30 \text{ cm}^{-3})n_{30}$, appropriate for thermal pressures, $P/k \approx 3000 \text{ cm}^{-3} \text{ K}$, inferred from observations of C I fine-structure populations (Jenkins & Tripp 2011). Setting the parenthetical terms equal to unity, we find a dust optical depth $\tau_d = 1.013$. The right-hand side of equation (8) scales as $(G/RN_d n_{\text{H}})$, which is insensitive to metallicity if the product (RN_d) remains constant. This would be expected if grain abundances decrease at lower metal abundances. In that case, N_d would increase and R would decrease. Thus, the transition should be governed by the FUV/density ratio (G/n_{H}) . In low-metallicity environments such as the LMC/SMC, the transition will occur at similar $\tau_d \approx 1$, but at higher total hydrogen column density, $N_{\text{H}} = \tau_d N_d$.

Previous studies of H_2 abundances estimated that $R \approx 3 \times 10^{-17} \text{ cm}^3 \text{ s}^{-1}$ (Jura 1975a). The observed transition implies a rate coefficient,

$$R = \left[\frac{4f_{\text{diss}}\beta_0 GA}{N_d n_{\text{H}}} \right] N_{\text{H}_2}^{1/4} [e^{\tau_d} - 1]^{-1} \approx (3.0 \times 10^{-17} \text{ cm}^3 \text{ s}^{-1}) G n_{30}^{-1} \left[\frac{N_{\text{H}_2}}{10^{19.5}} \right]^{1/4}, \quad (9)$$

for $\tau_d \approx 1$, as found above. This result suggests that absorbers with densities $n_{\text{H}} > 30 \text{ cm}^{-3}$ are associated with elevated radiation fields ($G > 1$) from their proximity to hot stars.

We see that dust can be an important factor, along with H_2 self-shielding, in the onset of the molecular transition. Our results show that the transition occurs when $\tau_d \approx 1$. Because the dust-to-gas ratio depends

on abundances of C, Si, O, and other refractory heavy elements, changes in metallicity will have offsetting effects on the H₂ fractions through the formation coefficient (R) and radiative attenuation (τ_d). This analysis may explain the observed hydrogen column densities of the molecular transition at $f_{\text{H}_2} = 0.1$, which occurs at $\log N_{\text{H}} \approx 21.0$ in the Milky Way, $\log N_{\text{H}} \approx 21.3$ in the LMC, and $\log N_{\text{H}} \approx 22.0$ in the SMC. Sight lines at high Galactic latitude (Gillmon et al. 2006) showed a transition at lower columns ($\log N_{\text{H}} \approx 20.4$), likely because of lower radiation-to-density ratios, and possibly one-sided absorber illumination from the disk stars. The current *FUSE* survey of the Milky Way disk exhibits no obvious shift with distance, but large changes in metallicity are not expected over the range of target star distances.

More precise determinations of R require knowledge of n_{H} , FUV radiation field, and dust properties, which may depend on metallicity and environment. Interstellar clouds are inhomogeneous, with internal variations in temperature, hydrogen density, and metallicity. Irradiated cloud models have been constructed (Browning et al. 2003; Le Petit et al. 2006; Nehmé et al. 2008; Klimenko & Balashev 2020) that follow the attenuation of UV radiation into the cloud and the resulting changes in gas temperature (T_g), dust temperature (T_d) and molecular fraction. These models depend sensitively on n_{H} , β_0 , G , and $R(T_g, T_d, Z)$. The best measures of the FUV radiation field and cloud density are the high- J excitation ratios, $N(4)/N(2)$ and $N(5)/N(3)$. These issues are discussed further in Section 3.5.

3.4. Rotational Excitation Temperatures ($J = 0, 1, 2$)

The excitation temperature T_{01} of the lowest two rotational states, $J = 0$ (para-H₂) and $J = 1$ (ortho-H₂) is frequently used as a measure of the kinetic temperature in diffuse clouds. This requires that the gas density and column density be sufficiently high for thermal proton collisions (Gerlich 1990) to couple the ortho and para forms of H₂ and set the ratio $N(1)/N(0)$. Recent experiments suggest that ortho-para conversion might occur on silicate grain surfaces (Tsuge et al. 2021). The expectation is that ortho/para production on grains would be in the 3:1 spin-statistical ratio. The observed low values of $T_{01} \approx 70 - 90$ K suggest that this formation channel is subdominant. Theoretical models of H₂ formation and destruction in diffuse clouds find that the lowest three rotational states ($J = 0, 1, 2$) are usually thermalized, with populations depending primarily on gas temperature. We assume that the observed populations obey Boltzmann ratios, with T_{01} and T_{02} determined from the expressions,

$$T_{01} = \frac{\Delta E_{01}/k}{\ln[(g_1/g_0)N(0)/N(1)]}, \quad (10)$$

$$T_{02} = \frac{\Delta E_{02}/k}{\ln[(g_2/g_0)N(0)/N(2)]}. \quad (11)$$

Here, $g_1/g_0 = 9$ and $g_2/g_0 = 5$ are ratios of statistical weights of the rotational levels, and $\Delta E_{01}/k = 170.48$ K and $\Delta E_{02}/k = 509.86$ K come from the rotational energies computed by Komasa et al. (2011).

The initial *Copernicus* study of H₂ in 13 clouds with $N(0) \geq 10^{17}$ cm⁻² found a mean temperature $\langle T_{01} \rangle = 81 \pm 13$ K (Spitzer & Cochran 1973). A more extensive *Copernicus* survey (Savage et al. 1977) of 61 stars with $\log N_{\text{H}_2} \geq 18$ found $\langle T_{01} \rangle = 77 \pm 17$ K (rms). In their study of CO and H₂ in diffuse molecular clouds, Sheffer et al. (2008) tabulated total H₂ column densities N_{H_2} along 58 sight lines studied with *FUSE*. For 24 stars in common with our 139, there was reasonable agreement in $\log N_{\text{H}_2}$, typically within ± 0.10 . We also compared our H₂ column densities to those in the metallicity study (O, Ge, Kr) of Jenkins (2019). For 57 stars in common, we found near agreement (within ± 0.03) for $\log N(0)$ and $\log N(1)$ in 22 and 18 sight lines, respectively. For the other stars, the column densities agreed within ± 0.10 . We also compared

the tabulated rotational temperatures in these two studies. Sheffer et al. (2008) quoted a mean rotational temperature, $\langle T_{01} \rangle = 76 \pm 14$ K for 56 sight lines, similar to the *Copernicus* result of 77 ± 17 K (Savage et al. 1977). In our current *FUSE* survey of 139 stars, we find $\langle T_{01} \rangle = 88 \pm 20$ K. Comparing to the 57 common sight lines with Jenkins (2019), we found only a few differences. These are attributable to different values of $N(0)$ and $N(1)$ arising from fitting the damping wings. Sheffer et al. (2008) did not tabulate individual column densities, $N(0)$ and $N(1)$, and we were unable to investigate the source of the differences.

Figure 7 shows the distributions of T_{01} with $E(B - V)$ and N_{H} . Removing the four labeled outliers reduces the mean slightly to $\langle T_{01} \rangle = 87$ K. The distributions of T_{02} are shown in **Figure 8**. For the reduced sample (four outliers removed) of 128 stars with measured $J = 2$ column densities, we find $\langle T_{02} \rangle = 77 \pm 18$ K. In their analysis of H_2 in the LMC and SMC, Tumlinson et al. (2002) found $\langle T_{01} \rangle = 82 \pm 21$ K for 22 sight lines with $N_{\text{H}_2} \geq 10^{16.5} \text{ cm}^{-2}$. Kruczek et al. (2019) explored the contributions of higher rotational lines to the damping wings of $J = 1$ lines. Their re-analysis of nine *Copernicus* sight lines and 13 from *FUSE* altered $N(0)$ and $N(1)$, resulting in a reduced $T_{01} = 68 \pm 13$ K (12% lower than their previous values). Our *FUSE* survey extends to larger column densities and greater stellar distances than *Copernicus* and contains more than twice the number of stars. Given the dispersions in T_{01} and T_{02} distributions, their agreement suggests that the diffuse ISM has similar heating and cooling rates over a wide range of cloud densities, metallicities, and FUV radiation fields.

Even for the best determinations of $\log N(0)$ and $\log N(1)$, rotational temperatures T_{01} have errors of $\sigma_{T_{01}} \approx 4$ K. Uncertainties on T_{02} can be higher, when $\log N(2)$ is poorly determined. From errors on $\log N_0$, $\log N_1$, and $\log N_2$, and neglecting covariance, the propagated errors on T_{01} and T_{02} derived from equations (10) and (11) are:

$$\frac{\sigma_{T_{01}}}{T_{01}} = 2.303 \left[\frac{T_{01}}{170.48 \text{ K}} \right] [\sigma_{\log N_0}^2 + \sigma_{\log N_1}^2]^{1/2} \quad (12)$$

$$\frac{\sigma_{T_{02}}}{T_{02}} = 2.303 \left[\frac{T_{02}}{509.86 \text{ K}} \right] [\sigma_{\log N_0}^2 + \sigma_{\log N_2}^2]^{1/2} . \quad (13)$$

For equal errors on $J = 0$ and $J = 1$ column densities, $\sigma_{\log N_1} = \sigma_{\log N_0}$, this expression simplifies to $\sigma_{T_{01}} \approx [T_{01}^2/52.34]\sigma_{\log N_0}$. For the best fits to the damping wings ($\sigma_{\log N_0} = 0.03$) the temperature uncertainty is $\sigma_{T_{01}} = 4.3$ K at $T_{01} \approx 87$ K. In poorer quality data, with $\sigma_{\log N_0} \approx \sigma_{\log N_1} = 0.07$, the uncertainty is higher, $\sigma_{T_{01}} \approx 10$ K. Errors on $J = 2$ column densities are usually much larger than those for $J = 0$. Thus, $\sigma_{T_{02}} \approx [T_{02}^2/221.39]\sigma_{\log N_2}$. At $T_{02} \approx 77$ K, the uncertainty $\sigma_{T_{02}} \approx 5\text{--}11$ K for $\sigma_{\log N_2} = 0.20 - 0.40$.

3.5. Rotational Excitation Temperatures ($J \geq 3$)

The higher rotational levels ($J \geq 3$) of H_2 are generally believed to be populated by the fluorescent cascade following FUV radiative pumping in the Lyman and Werner bands (Black & Dalgarno 1976; Spitzer & Zweibel 1974; Jura 1974). The FUV radiation field includes the ambient Galactic radiation field (Jura 1974; Habing 1968; Draine 2011) augmented by local flux from O stars. Measurements by *Copernicus* (Spitzer et al. 1974; Morton 1975) found that levels $J \geq 3$ were populated in excess of predictions from T_{01} . The column densities in $J = 3, 4, 5$ were fitted to excitation temperatures $T_{\text{exc}} \approx 200 - 500$ K, and sometimes as high as 1100 K near luminous early O-type stars such as Zeta Puppis (Morton & Dinerstein 1976). Subsequent studies of H_2 excitation using *FUSE* data (Browning et al. 2003; Sheffer et al. 2008; Nehmé et al. 2008; Jensen et al. 2010) also found $T_{\text{exc}} \approx 200 - 500$ K for $J \geq 3$. The mean rotational excitation temperature, fitted to $J \geq 3$ and averaged over our sample, is $T_{\text{exc}} = 326 \pm 125$ K with a typical

range from 150–650 K. These temperatures are similar to those seen toward selected *Copernicus* targets, and they likely reflect fluorescent pumping of high- J states. Some observations suggest that $J \geq 2$ levels may be influenced by collisional excitation (Gry et al. 2002; Nehmé et al. 2008; Ingalls et al. 2011) in a component of warm gas ($T > 500$ K) heated by turbulent dissipation (Moseley et al. 2020). Observationally, CH^+ is correlated with rotationally-excited H_2 (Jensen et al. 2010), leading to suggested production schemes for CH^+ involving hot H_2 (Falgarone & Puget 1995; Myers et al. 2015). Sheffer et al. (2008) tabulated several excitation temperatures to higher rotational states (T_{03} and T_{04}) for 56 *FUSE* sight lines. We chose not to tabulate these parameters, since our modeling experience (Browning et al. 2003) found them less useful than T_{24} and T_{35} . Many of their values of T_{04} seemed implausibly high (200-300 K) and inconsistent with our observed ratios of $N(4)/N(0)$. Because they did not tabulate individual values of $N(J)$, we could not investigate further.

In our survey, we choose to focus on individual pairs of upper (u) and lower (l) rotational states (J_l, J_u), in particular (0,2), (2,4), and (3,5). These parameters capture the fact that H_2 exists over a range of cloud temperatures, with radiative pumping changing throughout the cloud because of H_2 self-shielding and attenuation by FUV extinction. In addition, the rate of ortho-para conversion may change, depending on cloud density. This will affect radiative pumping from $J = 0$, $J = 1$, and sometimes $J = 2$, creating departures of rotational populations of $J \geq 3$ from a single excitation temperature. For these reasons, we tabulate pairwise excitation temperatures, T_{02} , T_{24} , and T_{35} , each remaining within para (even- J) and ortho (odd- J) forms of H_2 . The temperatures T_{04} and T_{15} are not as useful diagnostics. Detailed models of the excitation processes and radiative transfer may help to distinguish the relative contributions of FUV pumping and collisional excitation and to estimate the FUV radiation field and gas density.

Based on column densities $N(J)$ in the *FUSE* survey, **Table 4** lists four excitation temperatures, T_{01} , T_{02} , T_{24} , and T_{35} , between upper and lower rotational states defined by

$$T_{lu} = \frac{(E_u - E_l)/k}{\ln[(g_u/g_l)(N_l/N_u)]}, \quad (14)$$

corresponding to Boltzmann population ratios,

$$N(1)/N(0) = (9/1) \exp[-170.48 \text{ K}/T_{01}] \quad (15)$$

$$N(2)/N(0) = (5/1) \exp[-509.86 \text{ K}/T_{02}] \quad (16)$$

$$N(4)/N(2) = (9/5) \exp[-1171.78 \text{ K}/T_{24}] \quad (17)$$

$$N(5)/N(3) = (11/7) \exp[-1488.66 \text{ K}/T_{35}]. \quad (18)$$

These excitation temperatures were derived from the relativistic quantum calculations of Komasa et al. (2011), using the J -level dissociation energies in their Table 1. From the observed populations of higher- J states, we find mean excitation temperatures, $\langle T_{24} \rangle = 237 \pm 91$ K and $\langle T_{35} \rangle = 304 \pm 108$ K. Even with a wide range of these temperatures, they generally exhibit a correlation between the two parameters.

Figure 9 shows the rotational distributions in four of the six sight lines with detections up to $J = 7$. These include Star #48 (HD 93250) with $\log N(7) = 15.54 \pm 0.15$; Star #88 (HD 163892) with $\log N(7) = 14.14 \pm 0.06$; Star #116 (HD 199579) with $\log N(7) = 14.29 \pm 0.11$; and Star #137 (HD 303308) with $\log N(7) = 15.43 \pm 0.15$. The absorbers along these sight lines have different excitation temperatures. Two exhibit higher excitation temperatures for $J = 4$ and $J = 5$, likely produced by elevated FUV radiation fields from absorber proximity to hot stars.

Figure 10 displays distributions of the four excitation temperatures with stellar target distance. We see no obvious trend with increasing distance, although stars beyond 4–5 kpc are unlikely to be an unbiased

sample. The similar values of T_{01} and T_{02} suggest that the $J = 0, 1, 2$ levels are thermalized to the gas kinetic temperature. Both T_{24} and T_{35} show several outliers, well above their distribution means of 237 K and 304 K, respectively. For this 10-15% population, higher rotational excitation is expected from exposure to local FUV radiation above the background.

Figure 11 shows the relation of T_{24} and T_{35} , color-coded by the SpT of the target star. With the exception of a few labeled outliers, the para-H₂ levels ($J = 2$ and 4) and ortho-H₂ levels ($J = 3$ and 5) have correlated excitation temperatures above 300 K. Most sight lines have $T_{35} > T_{24}$, with data points above the dashed line of unit slope. This difference could arise from strong pumping of ortho-H₂ populations out of $J = 1$. Alternatively, thermalization of the $J = 2$ population to the gas kinetic temperature may alter the pumping out of $J = 2$. The expectation that high- J populations would be greater toward hotter O-type stars is not consistently reflected in this plot. The labeled sight lines with $T_{35} > 500$ K include two early O-type stars (#4, #48), two later O-type stars (#32, #122), and two B0/B0.5 stars (#2, #59). A number of hot (O2–O4) stars exhibit high excitation temperatures ($T_{35} > 450$ K), while others have $T_{35} < 400$ K. This mixed distribution suggests that radiative pumping of $J \geq 3$ levels is sometimes enhanced by proximity of the molecular absorbers to nearby hot stars. Deriving the pertinent model parameters of FUV absorption rate and absorber density will require modeling of the ratios $N(4)/N(2)$ and $N(5)/N(3)$, as performed by Browning et al. (2003) and Klimenko & Balashev (2020).

4. Discussion and Summary

This *FUSE* survey of interstellar H₂ in the Milky Way disk complements the pioneering survey by *Copernicus*, with several important extensions. Because *FUSE* was a more sensitive spectrograph, the survey includes more OB-star targets at greater distances and larger H₂ column densities. Many *FUSE* sight lines exhibit molecular fractions above the value, $f_{\text{H}_2} \geq 0.01$ at $\log N_{\text{H}} \geq 20.7$, noted in the *Copernicus* survey (Savage et al. 1977). We also measured H₂ populations in higher rotational states ($J \geq 2$) as well as $J = 0$ and $J = 1$. The *FUSE* sample includes the 139 OB-star targets with updated distances and $E(B - V)$ from Shull & Danforth (2019) derived from updated spectral types, digital photometry, and optical-NIR dust extinction in the Galactic O-star Spectroscopic Survey (Maíz Apellániz et al. 2004; Maíz-Apellániz & Barbá 2018). Our measurements of H₂ populations in the lowest three rotational states ($J = 0, 1, 2$) found similar excitation temperatures, $T_{01} \approx T_{02} \approx 70 - 90$ K, suggesting thermal coupling to the gas kinetic temperature. Populations of higher rotational states ($J \geq 3$) could be used to distinguish between radiative pumping and collisional excitation. The pairwise excitation temperatures, T_{24} and T_{35} , are correlated at the high end of the distribution, with $T_{35} > T_{24}$. After deriving total hydrogen column densities, N_{H} , from those of H₂ and H I, we compared them to updated values of selective extinction, $E(B - V)$, to find a mean gas-to-dust ratio in the Galactic disk, $\langle N_{\text{H}}/E(B - V) \rangle = (6.07 \pm 1.01) \times 10^{21} \text{ cm}^{-2} \text{ mag}^{-1}$.

The *FUSE* survey finds that a typical atomic-to-molecular transition in the ISM of the Galactic disk occurs at molecular fraction $f_{\text{H}_2} \approx 0.1$ and molecular column density $N_{\text{H}_2} \approx 10^{19.5} \text{ cm}^{-2}$. This transition can be understood with a simple analytic model describing its dependence on H₂ formation on dust-grain surfaces and photo-dissociation by FUV radiation, including self-shielding and dust attenuation. This formulation shows that the transition depends on the ratio of FUV flux to gas density, analogous to the photoionization parameter used in the analysis of nebular lines. The transition occurs at dust optical depth $\tau_d \approx 1$ and total hydrogen column density $N_{\text{H}} = \tau_d N_d$, where the dust-opacity parameter $N_d \approx 4.5 \times 10^{20} \text{ cm}^{-2}$ at solar metallicity ($Z \approx Z_{\odot}$). The H I-to-H₂ conversion is mediated by both dust opacity and H₂ self-shielding. The optical depth $\tau_d \approx 1$ is likely insensitive to metallicity and grain/gas ratio, because of offsetting effects

of grain surface area on the H₂ formation rate coefficient (R) and dust opacity (N_d).

With a mean fractional abundance $\langle f_{\text{H}_2} \rangle \approx 0.2$ in diffuse interstellar clouds, radiative cooling by 28.22 μm emission from the $J = 2$ level of H₂ (510 K excitation) augments the dominant cooling from the 157.74 μm [C II] fine-structure line (91.21 K excitation). At low densities, the cooling rate from H⁺-H₂ collisions is $\mathcal{L}_{\text{H}_2} = (3.1 \times 10^{-28} \text{ erg cm}^3 \text{ s}^{-1}) n_{\text{HI}} n_{\text{H}_2}$ at $T = 100$ K (Forrey et al. 1997), while that from [C II] is $\mathcal{L}_{\text{CII}} \approx (3.0 \times 10^{-28} \text{ erg cm}^3 \text{ s}^{-1}) n_{\text{H}}^2$. We adopted an electron-impact collision strength $\Omega_{12} = 1.56$, a solar carbon abundance $n_{\text{C}}/n_{\text{H}} = 2.69 \times 10^{-4}$, and electron density $n_e \approx 3.3 \times 10^{-4} n_{\text{H}}$ donated by trace metal ions. Thus, $\mathcal{L}_{\text{H}_2}/\mathcal{L}_{\text{CII}} \approx 0.5 f_{\text{H}_2} (1 - f_{\text{H}_2})$ at 100 K. In higher density clouds, the H₂ 28.22 μm emission will be reduced by collisional de-excitation. The H₂ cooling rises at $T > 100$ K, but drops off exponentially in lower temperature clouds at higher N_{H} , owing to the 510 K excitation temperature of the $J = 2$ level.

The following summarizes the results of the *FUSE* survey of interstellar H₂ abundances and inferred physical parameters in the Milky Way disk:

1. The *FUSE* survey measured column densities of H₂ in the Galactic disk toward 139 OB stars with recently updated SpT, photometry, and distances (Shull & Danforth 2019). The survey extends the *Copernicus* H₂ survey (Savage et al. 1977) up to total hydrogen column densities $N_{\text{H}} \approx 5 \times 10^{21} \text{ cm}^{-2}$ and complements *FUSE* surveys of H₂ in the Magellanic Clouds (Tumlinson et al. 2002), translucent clouds (Rachford et al. 2002, 2009), and gas at high Galactic latitude (Gillmon et al. 2006; Wakker 2006).
2. For each sight line, we report column densities N_{H_2} , N_{HI} , $N(J)$, $N_{\text{H}} = N_{\text{HI}} + 2N_{\text{H}_2}$, and $f_{\text{H}_2} = 2N_{\text{H}_2}/N_{\text{H}}$, with mean values listed in Table 5. The mean gas-to-dust ratio, $\langle N_{\text{H}}/E(B - V) \rangle = (6.07 \pm 1.01) \times 10^{21} \text{ cm}^{-2} \text{ mag}^{-1}$, is slightly above the value of $5.8 \times 10^{21} \text{ cm}^{-2} \text{ mag}^{-1}$ in the *Copernicus* survey (Bohlin et al. 1978). The larger ratios seen in 21-cm/far-IR surveys at high Galactic latitudes (Liszt 2014a,b) suggest different distributions of gas and dust above the disk, produced by grain sedimentation to the disk plane or dust destruction when transported above the disk.
3. Using an analytic model of H₂ formation-destruction equilibrium with dust opacity and H₂ self-shielding, we derive an expression for the atomic-to-molecular transition, which occurs at optical depth $\tau_d \approx 1$, molecular fraction $f_{\text{H}_2} \approx 0.1$, $N_{\text{H}_2} \approx 10^{19.5} \text{ cm}^{-2}$, and $N_{\text{H}} \approx 10^{21} \text{ cm}^{-2}$. An H₂ formation rate coefficient $R \approx 3 \times 10^{-17} \text{ cm}^3 \text{ s}^{-1}$ is consistent with the observed transition, with occasional elevated FUV radiation fields in 10-15% of the sight lines. These parameters can be constrained with models of H₂ rotational populations, supplemented by C I fine-structure abundances (Jenkins & Tripp 2011; Klimenko & Balashev 2020).
4. The lowest three rotational states ($J = 0, 1, 2$) appear to be thermally coupled by collisions to the gas kinetic temperature. The survey mean excitation temperatures are $\langle T_{01} \rangle = 88 \pm 20$ K and $\langle T_{02} \rangle = 77 \pm 18$ K. For sight lines with $E(B - V) > 0.5$ and $\log N_{\text{H}} > 20.7$, these temperatures decrease to 50 – 70 K.
5. Populations of higher- J states are produced primarily by radiative pumping from FUV radiation. From column-density ratios of rotational levels $N(4)/N(2)$ and $N(5)/N(3)$, we find mean excitation temperatures, $\langle T_{24} \rangle = 237 \pm 91$ K and $\langle T_{35} \rangle = 304 \pm 108$ K (rms). In most cases, these two temperatures are correlated, with $T_{35} > T_{24}$, but we find no consistent connection with SpT (from O3 to B1). Elevated radiative pumping is likely produced by close proximity to hot stars, possibly with some collisional excitation from heating by turbulent dissipation.

Acknowledgements. This work was supported by the *FUSE* mission, with financial support from NASA Contract NAS5-32985 to Johns Hopkins University and a sub-contract to the University of Colorado at Boulder. We thank Jason Tumlinson for developing software for *FUSE* studies of H₂ and former CU undergraduates Teresa Ross and Kristen Gillmon for their assistance with data analysis during early stages of this project. We have benefitted from discussions on interstellar gas, molecules, and dust with Sergei Balashev, John Black, Bruce Draine, Kevin France, Ed Jenkins, Slava Klimenko, Harvey Liszt, Chris McKee, Blair Savage, and Don York.

REFERENCES

- Balashev, S. A., Klimenko, V. V., Noterdaeme, P., et al. 2019, *MNRAS*, 490, 2668
- Bialy, S., & Sternberg, A. 2016, *ApJ*, 822, 83
- Black, J. H., & Dalgarno, A. 1976, *ApJ*, 203, 132
- Bohlin, R. C., Savage, B. D., & Drake, J. F. 1978, *ApJ*, 224, 132
- Bowen, D. V., Jenkins, E. B., Tripp, T. M., et al. 2008, *ApJS*, 176, 59
- Browning, M. K., Tumlinson, J., & Shull J. M. 2003, *ApJ*, 582, 810
- Burgh, E. B., France, K., & McCandliss, S. R. 2007, *ApJ*, 658, 446
- Dalgarno, A., Black, J. H., & Weisheit, J. C. 1973, *Astrophys. Letters*, 14, 77
- Deutschman, W. A., Davis, R. T., & Schild, R. E. 1976, *ApJS*, 30, 97
- Diplas, A., & Savage, B. D. 1994, *ApJS*, 93, 211
- Draine, B. T. 2011, *Physical Processes in the Interstellar and Intergalactic Medium* (Princeton: Princeton Univ. Press)
- Draine, B. T., & Bertoldi, F. 1996, *ApJ*, 468, 269
- Falgarone, E., & Puget, J.-L. 1995, *A&A*, 293, 840
- Fitzpatrick, E. L., & Massa, D. 1990, *ApJS*, 72, 163
- Forrey, R. C., Balakrishnan, N., Dalgarno, A., & Lepp, S. 1997, *ApJ*, 489, 1000
- Gerlich, D. J. 1990, *J. Chem. Phys.*, 92, 2377
- Gillmon, K., & Shull, J. M. 2006, *ApJ*, 636, 908
- Gillmon, K., Shull, J. M., Tumlinson, J., & Danforth, C. 2006, *ApJ*, 636, 891
- Green, J. C., Snow, T. P., Cook, T. A., Cash, W. C., & Poplawski, O. 1992, *ApJ*, 395, 289
- Gry, C., Boulanger, F., Nehmé, C., et al. 2002, *A&A*, 391, 675
- Habing, H. J. 1968, *B.A.N.*, 19, 421
- Hanson, M. M., Snow, T. P., & Black, J. H. 1996, *ApJ*, 392, 571
- Hébrard, G., Tripp, T. M., Chayer, P., et al. 2005, *ApJ*, 635, 1136
- Hensley, B. S., & Draine, B. T. 2021, *ApJ*, 906, 73
- Hollenbach, D. J., & McKee, C. F. 1979, *ApJS*, 44, 555
- Hollenbach, D. J., Werner, M. W., & Salpeter, E. E. 1971, *ApJ*, 163, 165
- Hoopes, C. G., Sembach, K. R., Hébrard, G., Moos, H. W., & Knauth, D. C. 2003, *ApJ*, 586, 1094
- Ingalls, J. G., Bania, T.M., Boulanger, F., et al. 2011, *ApJ*, 743, 174
- Jensen, A. G., Snow, T. P., Sonneborn, G., & Rachford, B. L. 2010, *ApJ*, 711, 1236

- Jenkins, E. B. 2019, *ApJ*, 872, 55
- Jenkins, E. B., & Peimbert, A. 1997, *ApJ*, 477, 265
- Jenkins, E. B., & Tripp, T. M. 2011, *ApJ*, 734, 65
- Jones, A. P., Tielens, A. G. G. M., & Hollenbach, D. J. 1996, *ApJ*, 469, 740
- Jorgenson, R. A., Murphy, M. T., Thompson, R., & Carswell, R. F. 2014, *MNRAS*, 443, 2783
- Jura, M. 1974, *ApJ*, 191, 375
- Jura, M. 1975a, *ApJ*, 197, 575
- Jura, M. 1975b, *ApJ*, 197, 581
- Klimenko, V. V., & Balashev, S. A. 2020, *MNRAS*, 498, 1531
- Komasa, J., Piszczatowski, K., Lach, G., et al., 2011, *J. Chem. Theory Comput.*, 7, 3105
- Kruczek, N., France, K., Hoadley, K., Fleming, B., & Nell, N. 2019, *ApJ*, 878, 77
- Krumholz, M. R., McKee, C. F., & Tumlinson, J. 2008, *ApJ*, 689, 865
- Krumholz, M. R., McKee, C. F., & Tumlinson, J. 2009, *ApJ*, 693, 216
- Lacour, S., Ziskin, V., Hébrard, G., et al., 2005, *ApJ*, 627, 251
- Le Petit, F., Nehmé, C., Le Bourlot, J., & Roueff, E. 2006, *ApJS*, 164, 506
- Lenz, D., Hensley, B. S., & Doré, O. 2017, *ApJ*, 846, 38
- Liszt, H. 2014a, *ApJ*, 780, 10
- Liszt, H. 2014b, *ApJ*, 783, 17
- Maíz Apellániz, J., & Barbá, R. H. 2018, *A&A*, 613, A9
- Maíz Apellániz, J., Walborn, N. R., Galué, H. A., & Wei, L. H. 2004, *ApJS*, 151, 103
- Massa, D., Fullerton, A. J., Sonneborn, G., & Hutchings, J. B. 2003, *ApJ*, 586, 996
- McCandliss, S. R. 2003, *PASP*, 115, 651
- Moos, H. W., Cash, W. C., Cowie, L. L., et al. 2000, *ApJ*, 538, L1
- Moos, H. W., Sembach, K. R., Vidal-Madjar, A., et al. 2002, *ApJS*, 140, 3
- Morton, D. C. 1975, *ApJS*, 197, 85
- Morton, D. C., & Dinerstein, H. L. 1976, *ApJ*, 204, 1
- Moseley, E. R., Draine, B. T., Tomida, K., & Stone, J. M. 2021, *MNRAS*, 500, 3290
- Myers, A. F., McKee, C. F., & Li, P. S. 2015, *MNRAS*, 453, 2747
- Nehmé, C., Le Bourlot, J., Boulanger, F., et al., 2008, *A&A*, 483, 485
- Noterdaeme, P., Ledoux C., Petitjean, P., & Srianand, R. 2008, *A&A*, 481, 327
- Rachford, B. L., Snow, T. P., Tumlinson, J., et al. 2002, *ApJ*, 577, 221
- Rachford, B. L., Snow, T. P., Destree, J. D., et al. 2009, *ApJS*, 180, 125
- Sahnow, D. J., Moos, H. W., Ake, T. B., et al. 2000, *ApJ*, 538, L7
- Savage, B. D., Bohlin, R. C., Drake, J. F., & Budich, W. 1977, *ApJ*, 216, 291
- Schlafly, E. F., & Finkbeiner, D. P. 2011, *ApJ*, 77, 103
- Schlegel, D. J., Finkbeiner, D. P., & Davis, M. 1998, *ApJ*, 500, 525
- Seab, C. G., & Shull, J. M. 1983, *ApJ*, 275, 652
- Sheffer, Y., Rogers, M., Federman, S. R., et al. 2008, *ApJ*, 687, 1075

- Shull, J. M., & Beckwith, S. 1982, *ARA&A*, 20, 163
- Shull, J. M., & Danforth, C. W. 2019, *ApJ*, 882, 180
- Shull, J. M., Tumlinson, J., Jenkins, E. B., et al. 2000, *ApJ*, 538, L73
- Shull, J. M., & Van Steenberg, M. E. 1985, *ApJ*, 294, 599
- Slavin, J. D., Dwek, E., & Jones, A. P. 2004, *ApJ*, 803, 7
- Snow, T. P., Black, J. H., van Dishoeck, E. F., et al. 1992, *ApJ*, 465, 245
- Snow, T. P., Rachford, B. L., Tumlinson, J., et al. 2000, *ApJ*, 538, L65
- Sota, A., Maíz Apellániz, J., Morrell, N. I., et al., 2014, *ApJS*, 211, 10
- Sota, A., Maíz Apellániz, J., Walborn, N. R., et al., 2011, *ApJS*, 193, 24
- Spitzer, L., & Cochran, W. D. 1973, *ApJ*, 186, L23
- Spitzer, L., Cochran, W. D., & Hirshfeld, A. 1974, *ApJS*, 28, 373
- Spitzer, L., & Zweibel, E. G. 1974, *ApJ*, 191, L127
- Sternberg, A., Le Petit, F., Roueff, E., & Le Bourlot, J. 2014, *ApJ*, 790, 10
- Tsuge, M., Namiyoshi, T., Furuya, K., et al. 2021, *ApJ*, in press (arXiv:2101.02357)
- Tumlinson, J., Shull, J. M., Rachford, B. L., et al. 2002, *ApJ*, 566, 857
- Wakker, B. P. 2006, *ApJS*, 163, 282

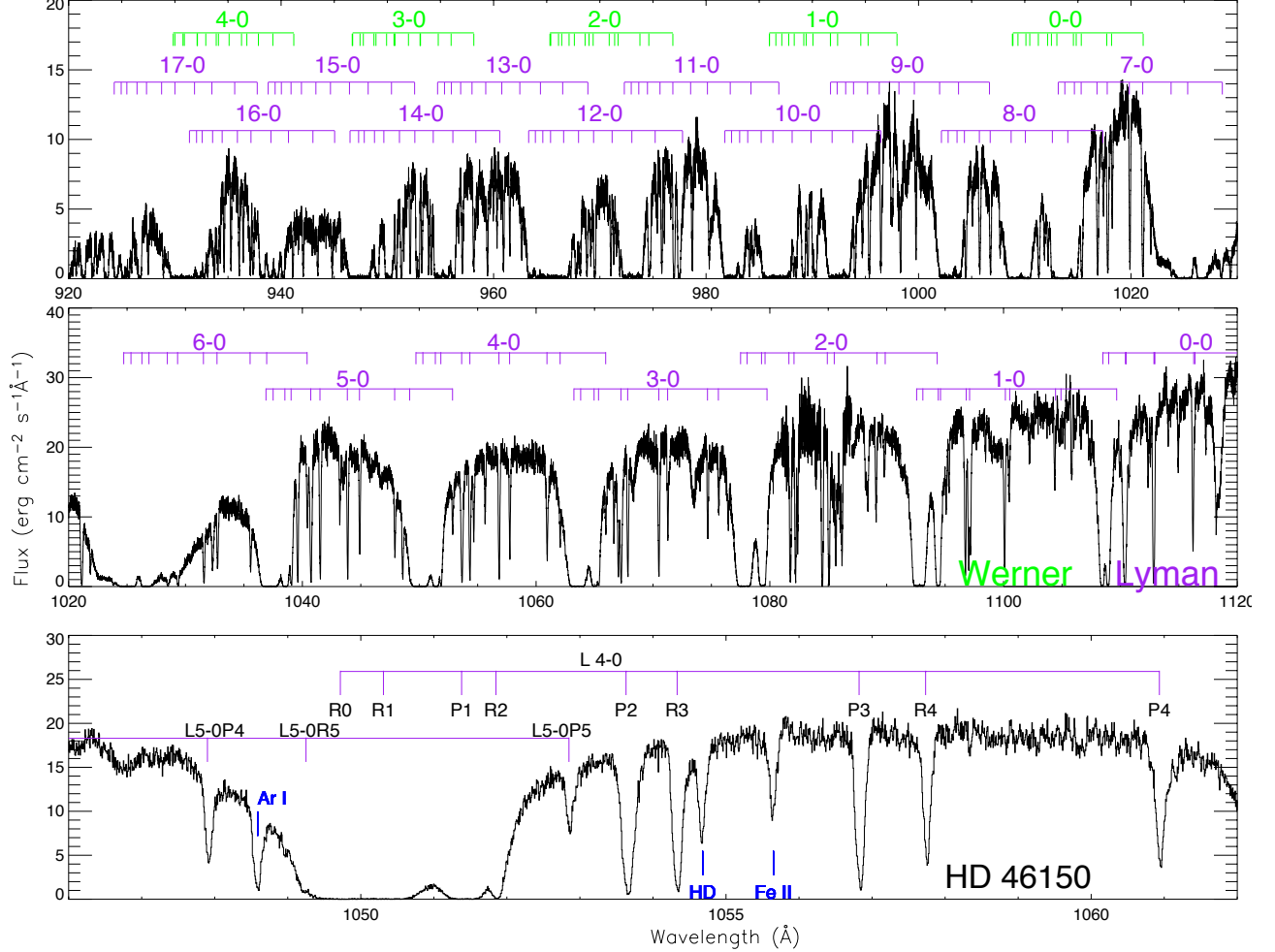


Fig. 1.— *FUSE* spectrum of the sight line to HD 46150, an O5 Vf star at 1.5 kpc distance and $E(B - V) = 0.45$, located inside the Rosette Nebula. Locations of the H_2 Lyman and Werner bands are shown as purple and green templates in the top two panels. Each template shows a different vibrational band ($v_u - v_\ell$) with a comb of absorption lines from rotational levels J in the ground vibrational state ($v_\ell = 0$) to the upper vibrational state (v_u) in the excited electronic states, $B^1\Sigma_u^+$ (Lyman bands) and $C^1\Pi_u$ (Werner bands). For each band, the template shows locations of R-branch and P-branch absorption lines from $J = 0, 1, 2, \dots$. The bottom panel shows a close-up of the (4-0) Lyman band, with nearby lines of Ar I (1048.220 Å), Fe II (1055.262 Å), HD (4-0) R(0) at 1054.294 Å, and P(4), R(5), P(5) lines from $J = 4$ and $J = 5$ levels of the (5-0) Lyman band. The R(0), R(1), P(1) lines have damping wings and are blended. In some bands, the P(1) and R(2) lines are separable. The P-branch and R-branch lines from higher- J states are sufficiently shifted to be measured. We find $\log N_{H_2} = 20.64 \pm 0.04$, with $\log N(0) = 20.23 \pm 0.05$, $\log N(1) = 20.42 \pm 0.05$, and rotational temperatures $T_{01} = 97 \pm 9$ K and $T_{02} = 55 \pm 4$ K.

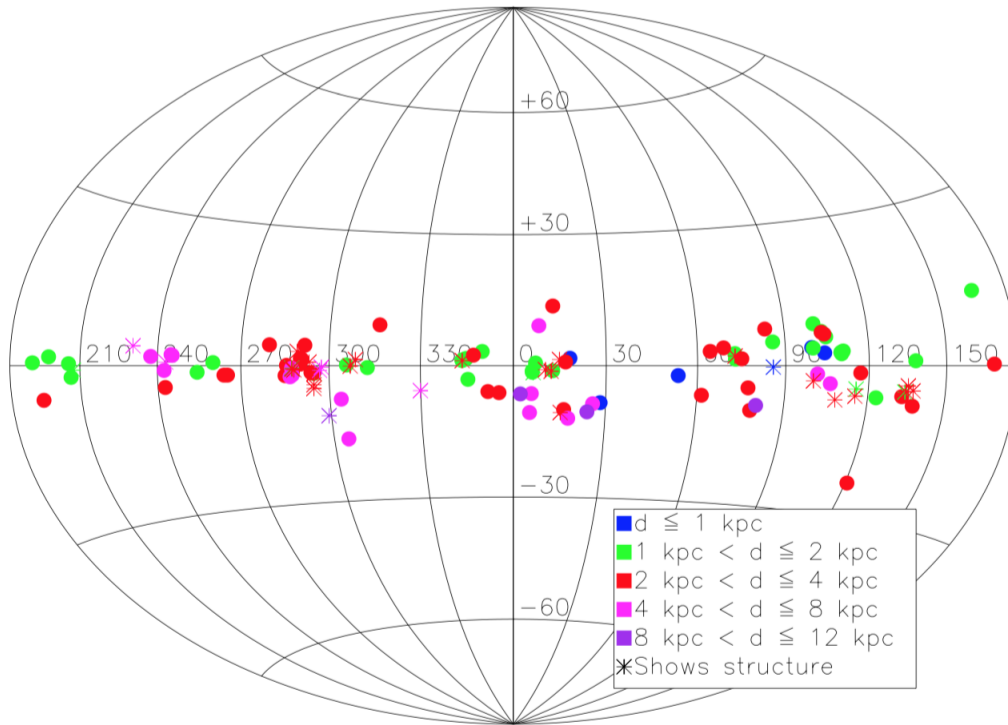


Fig. 2.— Aitoff projection plot of 139 target locations in Galactic coordinates (ℓ and b) with distances coded by color. Several sight lines with multiple velocity components that are separably measurable ($\Delta v \geq 20 \text{ km s}^{-1}$) are shown as asterisks.

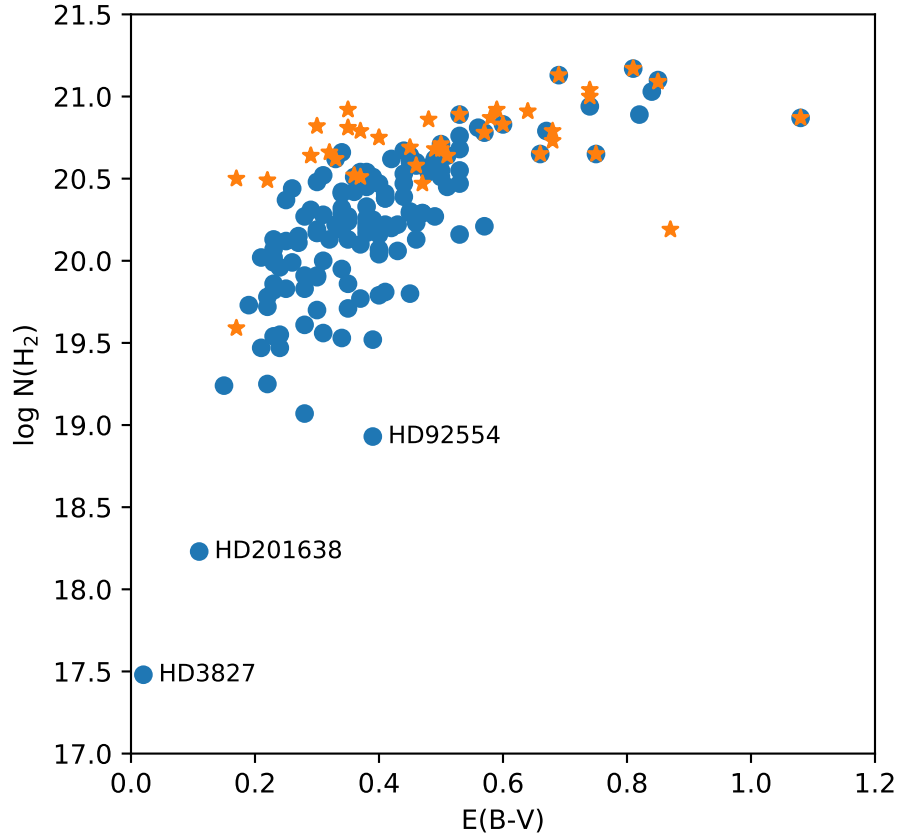


Fig. 3.— Distribution of H_2 column density with color excess, labeling three sight lines with $\log N_{\text{H}_2} < 19.0$. Symbols are color-labeled for the current *FUSE* survey (blue circles) and translucent sight lines (orange stars) also studied by *FUSE* (Rachford et al. 2002, 2009). We re-analyzed 11 of these translucent sight lines with our H_2 software for stars with new GOS photometry and SpTs (ID numbers 32, 82, 97, 98, 105, 107, 114, 116, 120, 122, 127).

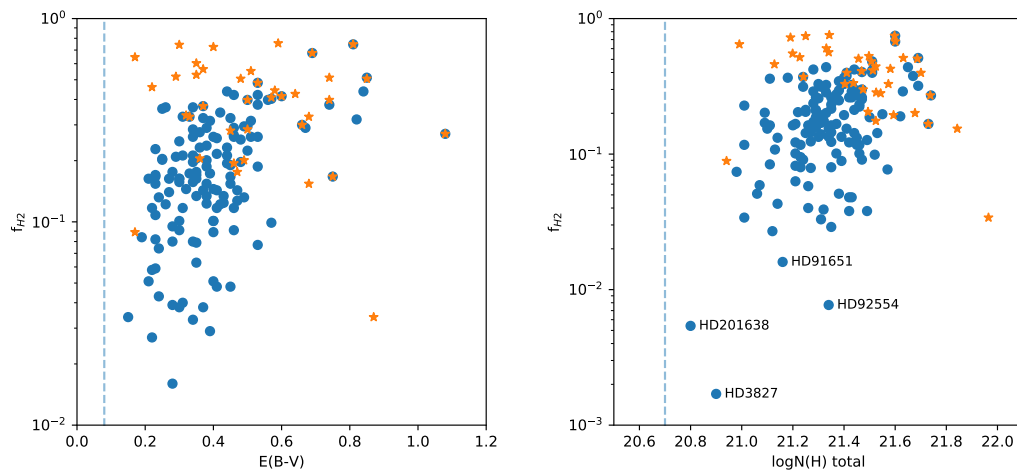


Fig. 4.— Molecular fraction f_{H_2} compared to color excess (left panel) and total hydrogen column density, $N_{\text{H}} = N_{\text{HI}} + 2N_{\text{H}_2}$ (right panel). Vertical dashed lines show the transition to $f_{\text{H}_2} > 0.01$ at $E(B - V) \gtrsim 0.08$ and $\log N_{\text{H}} \gtrsim 20.7$ seen in *Copernicus* data (Savage et al. 1977). Most of the *FUSE* targets are more distant and have f_{H_2} between 3% and 75%. Symbols are color-coded as in Figure 3. The outlier (orange star) with $f_{\text{H}_2} = 0.034$ at $E(B - V) = 0.87$ and $\log N_{\text{H}} = 21.96$ is the translucent sight line toward HD 164740 (Rachford et al. 2009).

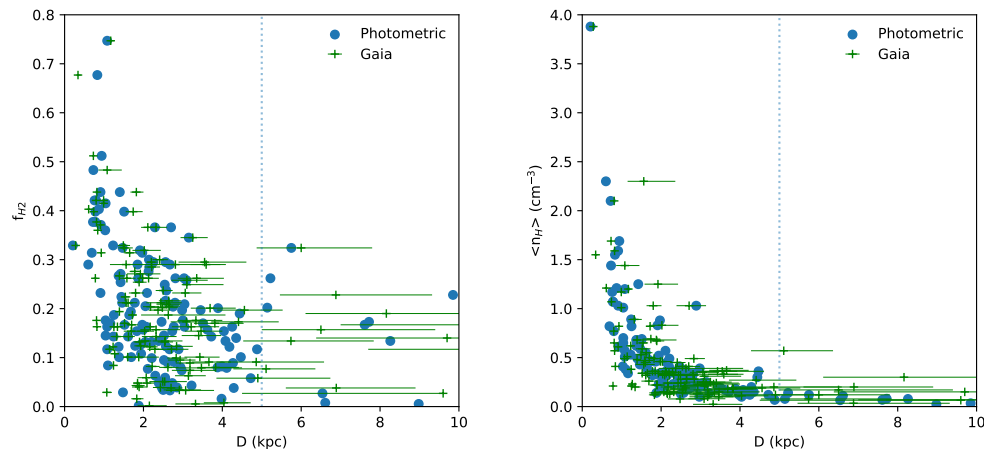


Fig. 5.— Molecular fraction f_{H_2} (left panel) and total hydrogen density n_{H} (right panel), averaged over photometric distance to target stars. Updated values (Shull & Danforth 2019) are shown for both photometric and *Gaia*-DR2 parallax distances. For 129 stars with photometric distances $D \leq 5$ kpc (vertical dashed lines) the mean sight-line values are $\langle n_{\text{HI}} \rangle = 0.50 \text{ cm}^{-3}$, $\langle f_{\text{H}_2} \rangle = 0.20$, and $\langle N_{\text{H}}/E(B - V) \rangle = 6.07 \times 10^{21} \text{ cm}^{-2} \text{ mag}^{-1}$. Table 5 lists these quantities for the full survey and for sub-samples ($D \leq 2$ kpc and $D \leq 5$ kpc).

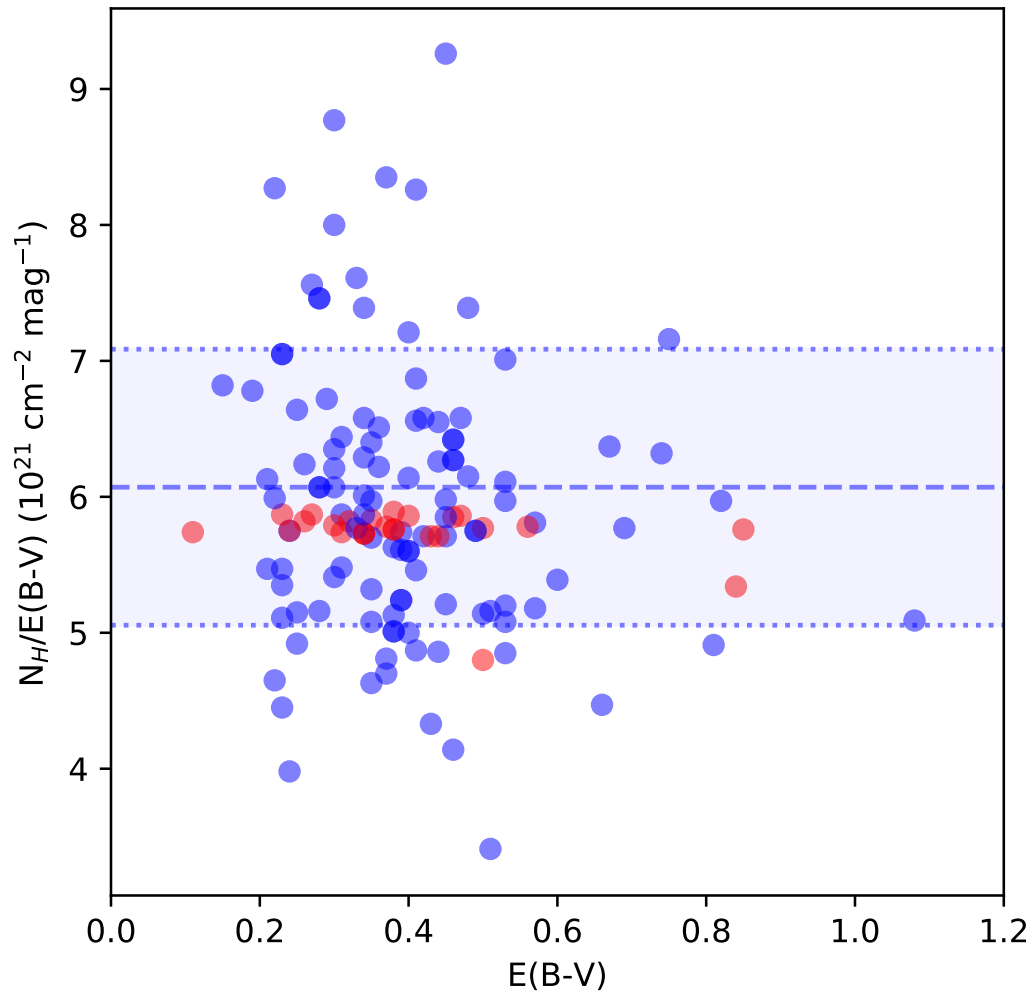


Fig. 6.— Distribution of the “gas-to-dust” ratio, $N_H/E(B - V)$, for 138 sight lines, in units of $10^{21} \text{ cm}^{-2} \text{ mag}^{-1}$. One star (ID #7, HD 3827) was omitted owing to its uncertain $E(B - V)$. Blue points are the 112 sight lines with N_{HI} determined from Ly α profile fits. Red points are the 26 stars lacking Ly α fits for H I (Tables 2 and 4), where N_{HI} was scaled from $E(B - V)$. The mean ratio for the 112 stars is $\langle N_H/E(B - V) \rangle = (6.07 \pm 1.01) \times 10^{21} \text{ cm}^{-2} \text{ mag}^{-1}$. The mean and (rms) deviations are shown as horizontal lines and blue wash.

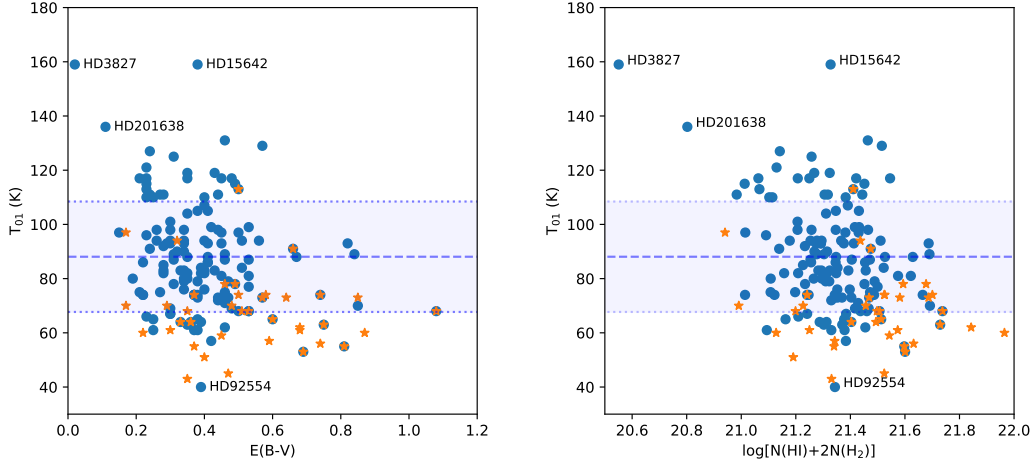


Fig. 7.— Rotational temperature T_{01} vs. color excess (left panel) and total hydrogen column density (right panel). The mean value $\langle T_{01} \rangle = 88 \pm 20$ K (horizontal dashed line with 1σ dispersions) should track the gas kinetic temperature in high-density clouds. Lower temperatures appear in translucent clouds at $E(B - V) \gtrsim 0.5$ and $\log N_{\text{H}} \gtrsim 21.5$. Symbols are color-coded as in Figure 3 with four outlier targets labeled.

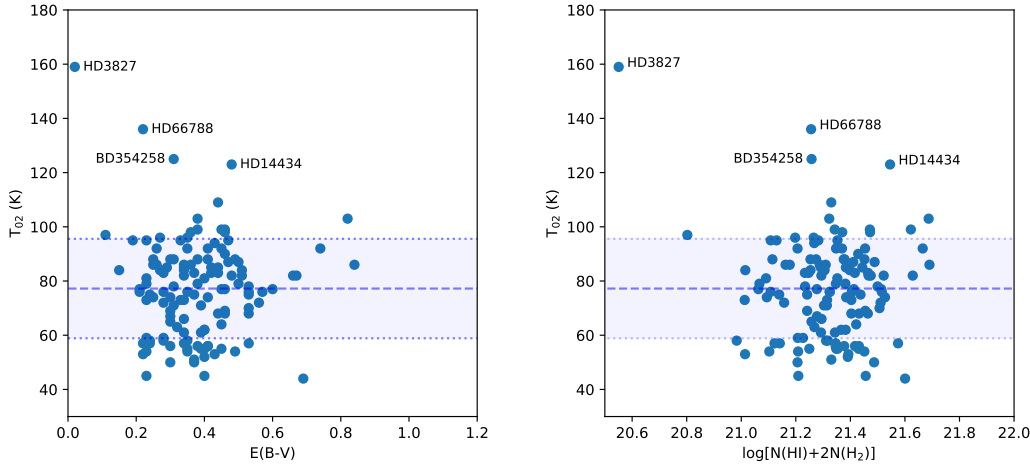


Fig. 8.— Rotational temperature T_{02} vs. color excess (left panel) and total hydrogen column density (right panel). Four outlier targets are labeled. The other 128 stars have a mean value $\langle T_{02} \rangle = 77 \pm 18$ K (horizontal dashed lines with mean and 1σ dispersions). Within individual sight-line errors (Section 3.4) and spreads of the distributions, $\langle T_{02} \rangle$ is similar to $\langle T_{01} \rangle = 88 \pm 20$ K. The lowest three rotational levels ($J = 0, 1, 2$) are likely coupled to the gas kinetic temperature.

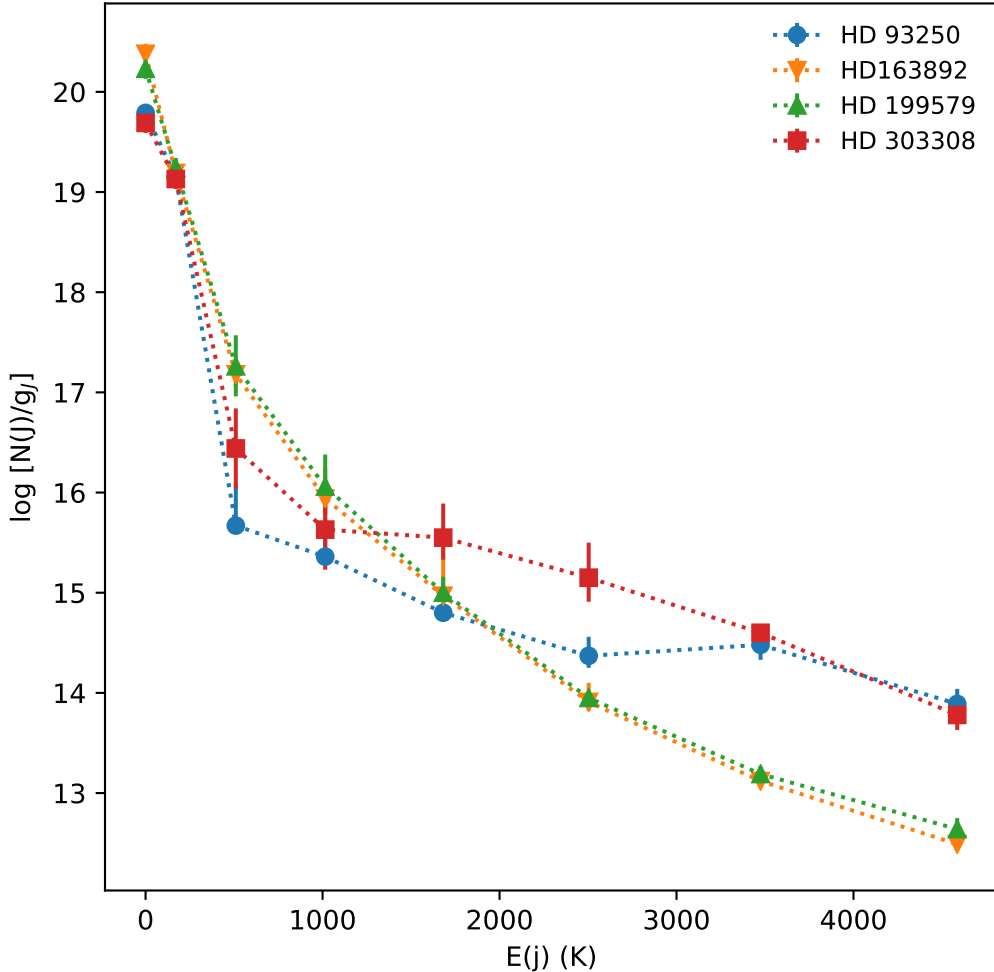


Fig. 9.— Populations of H₂ rotational states, $\log[N(J)/g_J]$, vs. their excitation energies, $E(J)/k$, expressed as temperatures. The level statistical weights are $g_J = (2S + 1)(2J + 1)$, where $S = 0$ (even- J) and $S = 1$ (odd- J). We show distributions ($J = 0 - 7$) for four sight lines with different excitation temperatures of low- J and high- J states. The lowest levels ($J = 0, 1, 2$) appear thermally coupled. For HD 199579 (O6.5 V) we find $T_{01} = 74$ K and $T_{02} = 75$ K, but $T_{24} = 225$ K and $T_{35} = 307$ K. For HD 163892 (O9 IV) we find $T_{01} = 62$ K and $T_{02} = 69$ K, but $T_{24} = 230$ K and $T_{35} = 319$ K. Two sight lines toward hotter stars show even higher excitation ($T_{24} = 582$ K, $T_{35} = 686$ K) for HD 93250 (O4 III) and ($T_{24} = 569$ K, $T_{35} = 1358$ K) for HD 303308 (O4.5 V).

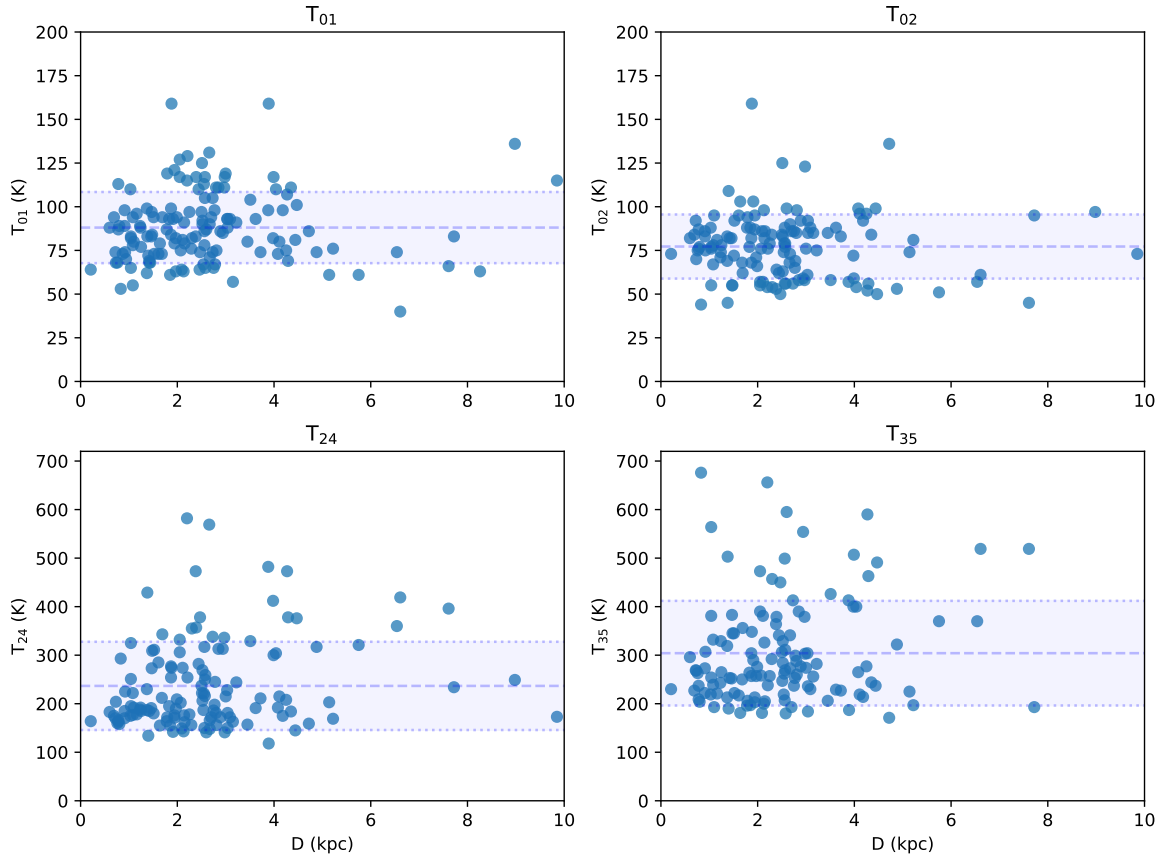


Fig. 10.— Excitation temperatures, T_{01} and T_{02} , of the lowest rotational levels and T_{24} and T_{35} for higher excited levels, versus photometric distance to the target stars. Several sight lines with missing or uncertain values of T_{02} , T_{24} , T_{35} , have been omitted. Horizontal lines show means and 1σ dispersions. A significant fraction (10-15%) in the lower two panels have high values of T_{24} and T_{35} , lying above the (rms) dispersions.

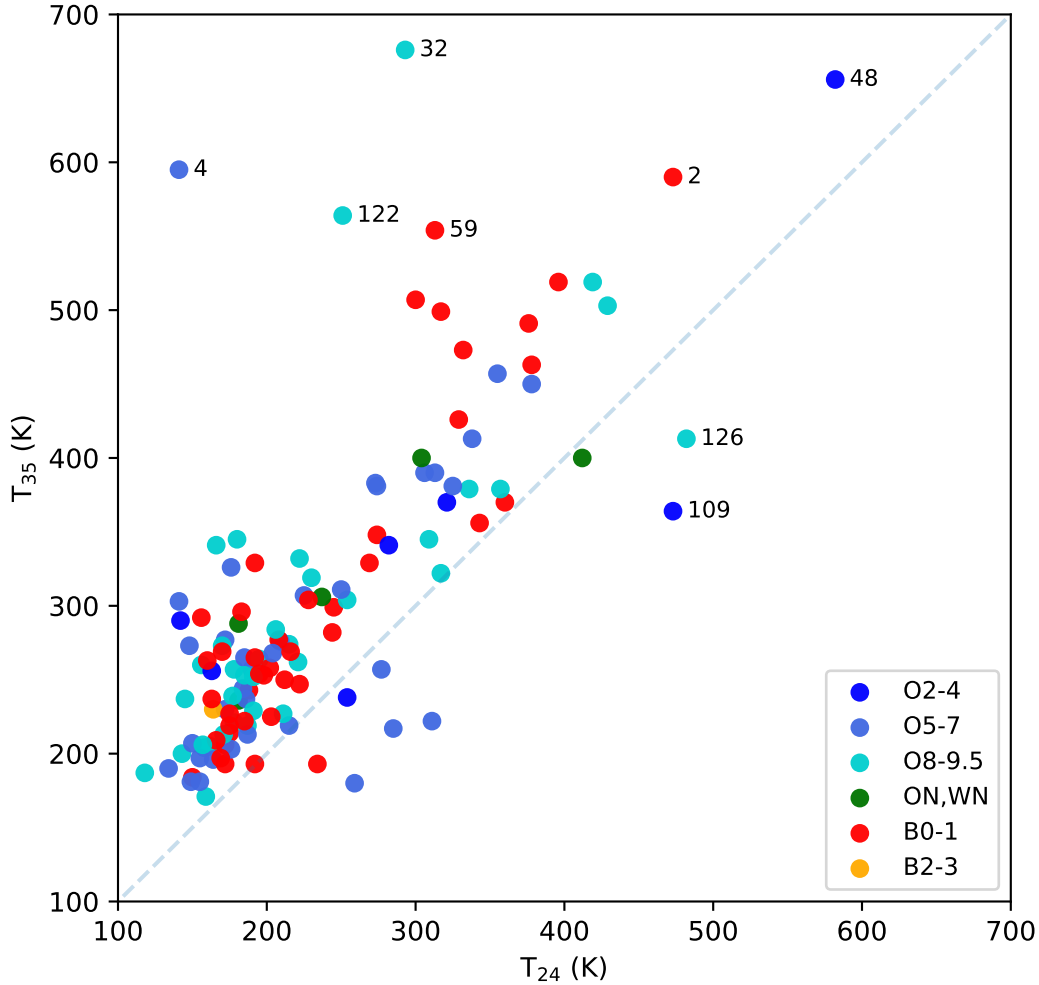


Fig. 11.— Relation between pairwise rotational excitation temperatures, T_{35} and T_{24} , connecting ortho (odd- J) and para (even- J) states. These two temperatures are correlated above 300 K, usually with $T_{35} > T_{24}$. Most data points lie above the dashed line of slope unity. Stars of similar SpT are color-coded as follows: dark blue (O2–O4); cornflower blue (O5–O7); cyan (O8–O9.5); dark green (ON and WN); red (B0–B1); and orange (one B3 star). Using internal ID numbers, we label stars with high excitation temperatures, plus several that lie off the trend-line (see Section 3.5). Star #137 (HD 303308, O4.5 Vfc) is not shown, with its off-scale excitation temperatures, $T_{35} = 1358$ K and $T_{24} = 569$ K.

Table 1. Stellar Parameters^a and Distances^b

ID	Target	ℓ (deg)	b (deg)	B (mag)	V (mag)	$E(B - V)$ (mag)	SpT	D_{phot}^b (kpc)	D_{Gaia}^b (kpc)	Program (FUSE ID)	t_{exp} (ksec)
1	BD 35°4258	77.19	-4.74	9.42	9.41	0.31	B0.5 Vn	2.51	1.89[1.71,2.10]	P1017902	5.673
2	BD 53°2820	101.24	-1.69	10.05	9.95	0.40	B0 IVn	4.27	3.18[2.82,3.65]	P1223203	5.147
3	CPD-59°2600	287.60	-0.74	8.82	8.81	0.53	O6 Vf	2.11	5.11[4.28,6.36]	P1221403	5.307
4	CPD-59°2603	287.59	-0.69	8.91	8.81	0.46	O7.5 V	2.60	3.66[3.22,4.22]	S3040502	31.599
5	CPD-69°1743	303.71	-7.35	9.40	9.38	0.30	B0.5 IIIIn	4.47	3.43[3.04,3.93]	P1013701	3.548
6	CPD-72°1184	299.15	-10.94	10.61	10.68	0.23	B0 III	9.85	6.88[5.46,9.32]	S5140103	9.172
7	HD 3827	120.79	-23.23	7.76	8.01	0.02	B0.7 V	1.88	2.15[1.85,2.59]	P1010302	2.885
8	HD 5005A	123.12	-6.24	8.19	8.10	0.41	O6.5 Vf	2.89	2.71[2.39,3.14]	P1020102	6.372
9	HD 12323	132.91	-5.87	8.88	8.90	0.29	ON9 V	3.04	2.59[2.33,2.93]	P1020201	3.865
10	HD 13268	133.96	-4.99	8.31	8.18	0.44	ON8.5 III	2.80	1.61[1.50,1.74]	P1020304	4.430
11	HD 13745	134.58	-4.96	7.99	7.83	0.46	ON9.7 IIIn	2.81	2.13[1.91,2.39]	P1020404	4.483
12	HD 14434	135.08	-3.82	8.65	8.49	0.48	O5.5 Vnfp	2.98	2.37[2.13,2.67]	P1020504	4.426
13	HD 15137	137.46	-7.58	7.91	7.86	0.35	O9.5 II-IIIn	3.00	3.33[2.86,4.00]	P1020602	2.282
14	HD 15558A	134.72	+0.92	8.41	7.91	0.82	O4.5 IIIf	1.91	2.02[1.72,2.44]	P1170101	2.472
15	HD 15642	137.09	-4.73	8.61	8.53	0.38	O9.5 II-IIIIn	3.89	3.69[3.20,4.34]	P1020702	4.837
16	HD 34656	170.04	+0.27	6.81	6.79	0.34	O7.5 IIf	1.99	2.32[1.92,2.93]	P1011301	4.179
17	HD 39680	194.07	-5.88	8.01	7.99	0.34	O6 Vnep	2.67	3.07[2.57,3.79]	P1020901	3.866
18	HD 41161	164.97	+12.89	6.68	6.76	0.23	O8 Vn	1.16	1.52[1.40,1.66]	P1021002	6.520
19	HD 42088	190.04	+0.48	7.62	7.55	0.39	O6 Vfz	1.97	1.65[1.50,1.83]	P1021101	4.137
20	HD 45314	196.96	+1.52	6.79	6.64	0.46	O9 npe	0.80	0.80[0.78,0.84]	P1021301	5.515
21	HD 46150	206.31	-2.07	6.89	6.76	0.45	O5 Vf	1.47	1.52[1.36,1.73]	P1021401	4.858
22	HD 47360	207.33	-0.79	8.32	8.19	0.41	B0.5 V	1.24	1.32[1.17,1.51]	P1021504	4.993
23	HD 47417	205.35	+0.35	6.98	6.97	0.31	B0 IV	1.23	1.49[1.35,1.66]	P1021602	4.079
24	HD 60369	242.68	-4.30	8.14	8.15	0.30	O9 IV	2.54	3.10[2.97,4.03]	P1050201	7.099
25	HD 61347	230.60	+3.80	8.60	8.43	0.45	O9 Ib	4.44	8.16[6.11,12.3]	P1022002	7.290
26	HD 62866	237.48	+1.80	9.08	9.01	0.35	B0.5 IIIIn	3.51	3.81[3.28,4.54]	P1221004	4.614
27	HD 63005	242.50	-0.93	9.08	9.13	0.27	O7 Vf	4.35	9.70[6.38,20.1]	P1022101	5.311
28	HD 64568	243.14	+0.71	9.43	9.38	0.37	O3 V* z	5.75	6.00[4.87,7.80]	P1221104	4.154
29	HD 66695	245.01	+2.21	9.77	9.78	0.27	B0.5 IV	4.25	3.21[2.72,3.92]	P1221201	8.080
30	HD 66788	245.43	+2.05	9.36	9.45	0.22	O8 V	4.72	4.90[3.85,6.74]	P1011801	4.209
31	HD 69106	254.52	-1.33	7.03	7.13	0.19	B0.2 V	1.10	1.24[1.17,1.33]	P1022302	0.404
32	HD 73882	260.18	+0.64	7.60	7.22	0.69	O8.5 IV	0.83	0.34[0.30,0.41]	P1161302	13.627
33	HD 74194	264.04	-1.95	7.78	7.57	0.50	O8.5 Ib-II	2.25	2.20[2.07,2.36]	P1022404	12.397
34	HD 74920	265.29	-1.95	7.56	7.53	0.35	O7.5 IV	2.05	2.65[2.42,2.92]	P1022601	4.672
35	HD 89137	279.69	+4.45	7.91	7.98	0.23	ON9.7 IIIn	4.04	3.46[3.05,4.00]	P1022801	4.628
36	HD 90087	285.16	-2.13	7.74	7.76	0.28	O9.2 III	2.52	2.93[2.62,3.32]	P1022901	3.934
37	HD 91597	286.86	-2.37	9.88	9.84	0.30	B1 IIIIne	4.29	6.89[5.61,8.90]	P1023004	6.228
38	HD 91651	286.55	-1.72	8.82	8.84	0.28	ON9.5 IIIIn	3.98	1.83[1.69,2.00]	P1023102	8.137
39	HD 91824	285.70	+0.07	8.07	8.14	0.25	O7 Vfz	2.75	2.18[1.99,2.41]	A1180802	4.649
40	HD 92554	287.60	-2.02	9.56	9.47	0.39	O9.5 IIIn	6.61	4.04[3.53,4.72]	P1023202	6.051
41	HD 93028	287.64	-1.19	8.24	8.30	0.24	O9 IV	2.97	3.18[2.72,3.83]	A1180902	4.446
42	HD 93129A	287.41	-0.57	7.51	7.26	0.57	O2 If* +O3 IIIIf*	2.21	2.83[2.60,3.11]	P1170202	7.361
43	HD 93146A	287.67	-1.05	8.48	8.45	0.35	O7 Vfz	2.30	3.14[2.80,3.58]	P1023301	4.140
44	HD 93204	287.57	-0.71	8.57	8.48	0.41	O5.5 Vf	2.73	2.09[1.94,2.27]	P1023501	4.664
45	HD 93205	287.57	-0.71	7.84	7.76	0.40	O3.5 V	2.44	2.49[2.27,2.76]	P1023601	4.693
46	HD 93206	287.67	-0.94	6.40	6.31	0.39	O9.7 IIn	1.48	1.07[0.96,1.20]	P1023401	4.140
47	HD 93222	287.74	-1.02	8.15	8.10	0.37	O7 IIIIf	2.47	2.70[2.47,2.99]	P1023701	3.920
48	HD 93250	287.51	-0.54	7.58	7.41	0.49	O4 IIIIfc	2.20	2.54[2.36,2.75]	P1023801	4.140
49	HD 93843	288.24	-0.90	7.26	7.30	0.28	O5 IIIIf	2.85	2.43[2.24,2.66]	P1024001	4.140
50	HD 96670	290.20	+0.40	7.57	7.43	0.46	O8 Ibf	2.67	3.59[3.19,4.09]	P1024201	4.273
51	HD 96715	290.27	+0.33	8.37	8.27	0.42	O4 Vf	3.15	3.25[2.94,3.63]	P1024301	4.597
52	HD 96917	289.28	+3.06	7.15	7.07	0.39	O8.5 Ibf	2.46	4.41[3.72,5.43]	P1024401	7.982
53	HD 97471	290.36	+1.62	9.55	9.30	0.30	B0 V	2.78	4.86[3.85,6.58]	A1180404	4.194
54	HD 97913	290.84	+1.41	8.84	8.80	0.32	B0.5 IVn	2.52	3.40[2.97,3.97]	P1221702	9.961

Table 1—Continued

ID	Target	ℓ (deg)	b (deg)	B (mag)	V (mag)	$E(B - V)$ (mag)	SpT	D_{phot}^b (kpc)	D_{Gaia}^b (kpc)	Program (FUSE ID)	t_{exp} (ksec)
55	HD 99857	294.78	-4.94	7.56	7.45	0.35	B0.5 Ib	3.04	2.17[2.04,2.33]	P1024501	4.266
56	HD 99890	291.75	+4.43	8.22	8.26	0.24	B0 III n	3.22	1.85[1.70,2.03]	P1024601	4.584
57	HD 100199	293.94	-1.49	8.14	8.14	0.30	B0 III ne	2.77	1.25[1.15,1.37]	P1221801	4.623
58	HD 100213	294.81	-4.14	8.25	8.22	0.34	O8 V n	2.15	2.21[2.03,2.42]	P1024701	4.561
59	HD 100276	293.31	+0.77	7.20	7.16	0.28	B0.5 Ib	2.94	2.62[2.40,2.89]	P1024801	4.125
60	HD 101131	294.78	-1.62	7.14	7.15	0.31	O5.5 Vf	1.78	2.44[2.07,2.97]	P1024901	4.302
61	HD 101190	294.78	-1.49	7.31	7.27	0.36	O6 IV f	2.09	3.06[2.73,3.47]	P1025001	3.392
62	HD 101205	294.85	-1.65	6.48	6.42	0.38	O7 II:	1.64	2.63[1.94,4.08]	P1025101	0.059
63	HD 101298	294.94	-1.69	8.11	8.05	0.38	O6 IV f	2.58	2.50[2.31,2.74]	P1025201	4.565
64	HD 101413	295.03	-1.71	8.40	8.35	0.36	O8 V	2.13	1.78[1.65,1.94]	P1025301	4.161
65	HD 101436	295.04	-1.71	7.62	7.56	0.38	O6.5 V	1.85	2.81[2.18,3.95]	P1025401	4.152
66	HD 103779	296.85	-1.02	7.19	7.20	0.23	B0.5 I ab	3.99	2.22[2.06,2.41]	P1025601	4.336
67	HD 104705	297.45	-0.34	7.74	7.76	0.26	B0 Ib	4.18	2.16[1.99,2.36]	P1025701	4.482
68	HD 115071	305.76	+0.15	8.15	7.94	0.51	O9.5 III	1.87	1.98[1.84,2.14]	P1025901	4.347
69	HD 116781	307.05	-0.07	7.73	7.60	0.43	B0 III ne	1.79	1.93[1.77,2.12]	P1026101	2.961
70	HD 116852	304.88	-16.13	8.38	8.47	0.22	O8.5 II-III f	4.88	13[7.7,18]	P1013801	7.212
71	HD 118571	308.70	+1.35	8.74	8.76	0.26	B0.5 IV n	2.70	2.32[2.09,2.60]	P1222001	4.434
72	HD 124314A	312.67	-0.42	6.85	6.64	0.53	O6 IV nf	1.25	1.72[1.62,1.83]	P1026201	4.364
73	HD 124979	316.40	+9.08	8.62	8.53	0.41	O7.5 IV n	3.09	3.10[2.71,3.63]	P1026301	5.105
74	HD 148422	329.92	-5.60	8.69	8.60	0.35	B1 Ia	8.26	5.74[4.53,7.84]	P1015003	3.242
75	HD 152218	343.53	+1.28	7.78	7.61	0.48	O9 IV n	1.42	1.89[1.73,2.08]	P1015402	9.486
76	HD 152233	343.48	+1.22	6.72	6.59	0.45	O6 III f	1.52	1.70[1.57,1.86]	P1026702	4.104
77	HD 152248	343.46	+1.18	6.25	6.10	0.47	O7 I ab f	1.61	1.62[1.48,1.78]	P1026801	4.445
78	HD 152314	343.52	+1.14	8.05	7.86	0.50	O9 IV	1.44	1.54[1.42,1.67]	P1026901	4.040
79	HD 152623	344.62	+1.61	6.75	6.67	0.40	O7 V nf	1.04	data problem	P1027001	6.056
80	HD 152723	344.81	+1.61	7.31	7.16	0.47	O6.5 III	1.94	data problem	P1027102	5.019
81	HD 153426	347.14	+2.38	7.71	7.47	0.45	O8.5 III	1.83	2.03[1.84,2.27]	P1027202	5.413
82	HD 154368	349.97	+3.22	6.65	6.13	0.81	O9.2 I ab	1.08	1.17[1.11,1.25]	P1161901	12.320
83	HD 156292	345.35	-3.08	7.75	7.49	0.56	O9.7 III	1.51	1.74[1.55,1.98]	P1027403	6.648
84	HD 157857	12.97	+13.5	7.95	7.78	0.49	O6.5 III f	2.56	3.55[2.89,4.61]	P1027501	4.022
85	HD 158661	8.29	+9.05	8.32	8.18	0.38	B0.5 Ib	4.08	2.55[2.23,2.99]	P1222201	6.597
86	HD 161807	351.78	-5.85	6.92	6.99	0.23	O9.7 III: n	1.94	1.27[1.18,1.37]	P1222302	1.906
87	HD 163758	355.36	-6.10	7.35	7.32	0.35	O6.5 Ia fp	4.11	3.47[2.82,4.50]	P1015901	5.383
88	HD 163892	7.15	+0.62	7.60	7.44	0.46	O9 IV n	1.37	1.39[1.28,1.52]	P1027602	6.583
89	HD 164816	6.06	-1.20	7.09	7.08	0.31	O9.5 V	1.08	1.14[1.06,1.24]	P1016001	5.043
90	HD 165052	6.12	-1.48	6.96	6.86	0.42	O5.5 Vz	1.37	1.23[1.16,1.30]	P1027801	4.874
91	HD 165246	6.40	-1.56	7.80	7.71	0.40	O8 V n	1.38	1.88[1.55,2.39]	P1050301	7.782
92	HD 166546	10.36	-0.92	7.26	7.22	0.34	O9.5 IV	1.46	1.56[1.35,1.84]	P1222501	3.444
93	HD 166716	14.85	+1.39	7.87	7.95	0.38	B0 II-III	2.73	1.69[1.50,1.92]	P1050401	5.788
94	HD 167402	2.26	-6.39	8.94	8.95	0.23	B0 Ib	7.61	< 14 kpc	P1016201	3.856
95	HD 167659	12.20	-1.27	7.60	7.39	0.53	O7 II-III f	1.87	1.58[1.40,1.80]	P1028001	5.816
96	HD 167771	12.70	-1.13	6.66	6.54	0.44	O7 III nf	1.40	1.82[1.67,2.00]	P1028101	3.836
97	HD 167971	18.25	+1.68	8.27	7.50	1.08	O8 Ia fn	1.42	1.92[1.58,2.43]	P1162101	9.450
98	HD 168076	16.84	+0.84	8.61	8.18	0.75	O4 III f	1.97	data problem	P1162201	6.601
99	HD 168941	5.82	-6.31	9.41	9.34	0.37	O9.5 IV p	3.72	2.32[1.96,2.84]	P1016502	3.983
100	HD 172140	5.28	-10.61	9.90	9.96	0.22	B0.5 III	6.54	< 9.6 kpc	P1016603	5.244
101	HD 175754	16.39	-9.92	6.93	7.01	0.23	O8 II nf p	2.55	2.07[1.85,2.35]	P1016802	1.932
102	HD 175876	15.28	-10.58	6.81	6.92	0.21	O6.5 III nf	2.57	2.54[2.15,3.10]	P1016902	1.932
103	HD 177989	17.81	-11.88	9.28	9.33	0.25	B0 III	5.14	2.48[2.17,2.87]	P1017101	10.289
104	HD 178487	25.78	-8.56	8.82	8.66	0.40	B0 Ib	5.22	3.35[2.87,4.04]	P1017201	8.902
105	HD 179406	28.23	-8.31	5.47	5.34	0.33	B3 IV	0.21	0.28[0.27,0.29]	E0610301	21.228
106	HD 179407	24.02	-10.40	9.50	9.41	0.33	B0.5 Ib	7.72	3.09[2.69,3.63]	P1017301	13.858
107	HD 185418	53.60	-2.17	7.67	7.45	0.50	B0.5 V	0.78	0.74[0.72,0.76]	P1162301	4.399
108	HD 187459	68.81	+3.85	6.64	6.49	0.44	B0.5 Ib	1.68	1.39[1.31,1.48]	P1028201	4.504

Table 1—Continued

ID	Target	ℓ (deg)	b (deg)	B (mag)	V (mag)	$E(B - V)$ (mag)	SpT	$D_{\text{phot}}^{\text{b}}$ (kpc)	$D_{\text{Gaia}}^{\text{b}}$ (kpc)	Program (FUSE ID)	t_{exp} (ksec)
109	HD 190429A	72.59	+2.61	7.20	7.09	0.43	O4 If	2.38	2.04[1.91,2.20]	P1028401	5.390
110	HD 190918	72.65	+2.07	6.88	6.75	0.45	O9.5Iab+WN4	2.39	1.85[1.74,1.97]	P1028501	5.510
111	HD 191495	72.74	+1.41	8.51	8.41	0.40	B0 IV-V	1.69	1.60[1.48,1.74]	P1222901	6.329
112	HD 191877	61.57	-6.45	6.27	6.28	0.21	B1 Ib	2.07	1.34[1.23,1.48]	P1028701	6.132
113	HD 192035	83.33	+7.76	8.26	8.22	0.34	B0 III-IVn	2.29	2.11[1.94,2.31]	P1028603	6.624
114	HD 192639	74.90	+1.48	7.46	7.11	0.66	O7.5 Iab	2.14	2.41[2.23,2.62]	P1162401	4.834
115	HD 195965	85.71	+5.00	6.93	6.98	0.25	B0 V	1.03	0.84[0.81,0.87]	P1028803	14.047
116	HD 199579	85.70	-0.30	6.01	5.96	0.37	O6.5 Vfz	0.92	0.91[0.87,0.97]	P1162501	4.307
117	HD 201345	78.44	-9.54	7.61	7.75	0.15	ON9.2 IV	2.50	2.91[2.51,3.46]	P1223001	5.104
118	HD 201638	80.29	-8.45	8.92	9.05	0.11	B0.5 Ib	8.98	3.32[2.81,4.06]	P1018001	4.920
119	HD 203374A	100.51	+8.62	6.91	6.67	0.53	B0 IVpe	0.78	uncertain	B0300102	10.170
120	HD 206267	99.29	+3.74	5.82	5.62	0.53	O6 Vf	0.73	1.08[0.86,1.45]	P1162701	4.872
121	HD 206773	99.80	+3.62	7.12	6.91	0.51	B0 Vpe	0.69	0.93[0.91,0.96]	B0710901	4.399
122	HD 207198	103.14	+6.99	6.27	5.96	0.60	O8.5 II	1.04	0.99[0.94,1.05]	P1162801	13.177
123	HD 207308	103.11	+6.82	7.74	7.49	0.53	B0.5 V	0.76	0.99[0.96,1.03]	B0300301	22.382
124	HD 208440	104.03	+6.44	7.93	7.91	0.28	B1 V	1.04	0.81[0.79,0.83]	B0300401	9.777
125	HD 209339	104.58	+5.87	6.73	6.73	0.30	O9.7 IV	1.08	0.82[0.80,0.85]	B0300501	2.022
126	HD 210809	99.85	-3.13	7.59	7.54	0.34	O9 Iab	3.88	3.83[3.37,4.42]	P1223103	10.065
127	HD 210839	103.83	+2.61	5.30	5.05	0.57	O6.5 Infp	0.87	0.61[0.56,0.66]	P1163101	6.045
128	HD 216044	105.93	-3.64	8.59	8.51	0.38	B0 III-IV	2.57	2.84[2.53,3.25]	P1223801	5.612
129	HD 216532	109.65	+2.68	8.54	8.00	0.85	O8.5 Vn	0.94	0.73[0.72,0.75]	A0510202	22.736
130	HD 216898	109.93	+2.39	8.53	8.00	0.84	O9 V	0.91	0.82[0.80,0.84]	A0510303	19.543
131	HD 217035	110.25	+2.86	8.20	7.74	0.74	B0.5 V	0.72	0.81[0.79,0.83]	A0510404	10.187
132	HD 217312	110.56	+2.95	7.81	7.42	0.67	B0.5 V	0.60	1.56[1.15,2.36]	P1930501	10.814
133	HD 218915	108.06	-6.89	7.22	7.20	0.30	O9.2 Iab	3.62	6.5 [5.0, 9.4]	P1018801	5.325
134	HD 224151	115.44	-4.64	6.01	6.19	0.44	B0.5 II-III	0.91	1.80[1.63,2.01]	P1224103	6.145
135	HD 224257	115.25	-6.06	7.92	7.98	0.24	B0.2 IV	2.05	1.90[1.75,2.08]	P1050601	7.032
136	HD 224868	116.87	-1.44	7.39	7.29	0.34	B0 Ib	3.03	0.78[0.73,0.83]	P1220201	5.105
137	HD 303308	287.59	-0.61	8.33	8.19	0.46	O4.5 Vfc	2.66	2.29[2.10,2.51]	P1221602	7.679
138	HD 308813	294.79	-1.61	9.32	9.28	0.34	O9.7 IVn	3.45	4.56[3.87,5.53]	P1221903	5.667
139	HD 332407	64.28	+3.11	8.63	8.50	0.41	B0.5 III	2.56	2.64[2.39,2.95]	P1222802	4.277

^aUpdated stellar parameters, photometry, spectral types, and distances are from a survey of 139 OB-type stars (Shull & Danforth 2019) with their internal target ID (column 1). These parameters are based on optical and near-IR digital photometry and extinction corrections from the Galactic O-Star Spectroscopic Survey (Maíz Apellániz et al. 2004) and new spectral types (Sota et al. 2011, 2014). Columns 3 and 4 list the Galactic longitude and latitude. Later columns list the stellar photometry [B , V , $E(B - V)$], spectral types (SpT), photometric distances (D_{phot}), and parallax distances (D_{Gaia}) listed in Tables 1 and 2 of Shull & Danforth (2019). The last two columns give the Program ID and exposure time of the primary *FUSE* spectroscopic observations.

^bPhotometric distances (D_{phot}) are based on GOS photometry, extinctions, and SpTs and a new set of absolute magnitudes (see Shull & Danforth 2019). When GOS data were not available, we based photometric distances (shown in **boldface**) on photometry and SpT in the literature. Parallax distances (D_{Gaia}) and error ranges are based on parallaxes and errors from the *Gaia*-DR2 archive, after adding a constant parallax offset of 0.03 mas.

Table 2. H I Column Density Measurements^a

ID	Target (Star)	E_{B-V} ^b (mag)	$\log N_{\text{HI}}^c$ (Adopted)	$\log N_{\text{HI}}$ (SVS85)	$\log N_{\text{HI}}$ (DS94)	$\log N_{\text{HI}}$ (J19)	$\log N_{\text{HI}}^c$ (Other)
1	BD 35°4258	0.31	21.24			21.24 ^{+0.03} _{-0.07}	
2	BD 53°2820	0.40	21.35			21.35 ^{+0.05} _{-0.07}	
3	CPD -59°2600	0.53	21.54	21.48 ± 0.10	21.54 ± 0.07		21.48 ± 0.15 (FM90)
4	CPD -59°2603	0.46	21.43	21.48 ± 0.15	21.46 ± 0.07	21.43 ^{+0.04} _{-0.05}	
5	CPD -69°1743	0.30	21.16		21.12 ± 0.11	21.16 ^{+0.04} _{-0.09}	
6	CPD -72°1184	0.23	20.90		20.90 ± 0.08		
7	HD 3827	0.02	20.55		20.56 ± 0.09	20.55 ^{+0.07} _{-0.05}	
8	HD 5005A	0.41	21.40	21.48 ± 0.15	21.40 ± 0.10		
9	HD 12323	0.29	21.19			21.19 ^{+0.04} _{-0.05}	
10	HD 13268	0.44	21.34		21.34 ± 0.18	21.34 ^{+0.07} _{-0.07}	
11	HD 13745	0.46	21.34		21.26 ± 0.10	21.34 ^{+0.05} _{-0.05}	
12	HD 14434	0.48	21.45		21.45 ± 0.08		
13	HD 15137	0.35	21.24		21.11 ± 0.16	21.24 ^{+0.08} _{-0.06}	
14	HD 15558A	0.82	21.52		21.52 ± 0.18		
15	HD 15642	0.38	21.23	21.18 ± 0.07	21.23 ± 0.08		
16	HD 34656	0.34	21.22				21.22 (scaled)
17	HD 39680	0.34	21.30		21.30 ± 0.08		
18	HD 41161	0.23	21.01	20.98 ± 0.07	21.01 ± 0.08	21.09 ^{+0.05} _{-0.05}	
19	HD 42088	0.39	21.15		21.15 ± 0.08		
20	HD 45314	0.46	21.04		21.04 ± 0.09		
21	HD 46150	0.45	21.26	21.20 ± 0.10	21.26 ± 0.12		
22	HD 47360	0.41	21.46		21.46 ± 0.08		
23	HD 47417	0.31	21.13	21.20 ± 0.05	21.13 ± 0.09		
24	HD 60369	0.30	21.26		21.26 ± 0.10		
25	HD 61347	0.45	21.53		21.53 ± 0.13		
26	HD 62866	0.35	21.23				21.23 (scaled)
27	HD 63005	0.27	21.24			21.24 ^{+0.03} _{-0.06}	
28	HD 64568	0.37	21.16				21.16 (scaled)
29	HD 66695	0.27	21.12				21.12 (scaled)
30	HD 66788	0.22	21.23			21.23 ^{+0.04} _{-0.02}	
31	HD 69106	0.19	21.07		21.08 ± 0.06	21.07 ^{+0.04} _{-0.04}	
32	HD 73882	0.69	21.11				21.11 ± 0.15 (FM90)
33	HD 74194	0.50	21.23				21.23 (scaled)
34	HD 74920	0.35	21.15		21.15 ± 0.09		
35	HD 89137	0.23	21.03			21.03 ^{+0.07} _{-0.02}	
36	HD 90087	0.28	21.19		21.15 ± 0.06	21.19 ^{+0.05} _{-0.09}	
37	HD 91597	0.30	21.40	21.34 ± 0.10	21.40 ± 0.06		
38	HD 91651	0.28	21.15		21.15 ± 0.06		
39	HD 91824	0.25	21.12			21.12 ^{+0.04} _{-0.04}	21.15 ± 0.15 (FM90)
40	HD 92554	0.39	21.34		21.28 ± 0.10	21.34 ^{+0.09} _{-0.11}	
41	HD 93028	0.24	20.95				20.95 ± 0.15 (FM90)
42	HD 93129A	0.57	21.47			21.47 ^{+0.07} _{-0.04}	
43	HD 93146A	0.35	21.18		21.18 ± 0.09		
44	HD 93204	0.41	21.41	21.40 ± 0.10	21.41 ± 0.10		
45	HD 93205	0.40	21.36	21.34 ± 0.05	21.33 ± 0.10	21.36 ^{+0.05} _{-0.05}	
46	HD 93206	0.39	21.34		21.34 ± 0.11		
47	HD 93222	0.37	21.47			21.47 ^{+0.03} _{-0.04}	21.54 ± 0.15 (FM90)
48	HD 93250	0.49	21.39	21.26 ± 0.10	21.39 ± 0.15		
49	HD 93843	0.28	21.30	21.30 ± 0.05	21.33 ± 0.08	21.30 ^{+0.05} _{-0.04}	
50	HD 96670	0.46	21.28				21.28 (scaled)
51	HD 96715	0.42	21.20	21.15 ± 0.10	21.20 ± 0.16		
52	HD 96917	0.39	21.23		21.23 ± 0.11		
53	HD 97471	0.30	21.20				21.20 (scaled)
54	HD 97913	0.32	21.20				21.20 (scaled)

Table 2—Continued

ID	Target (Star)	E_{B-V}^b (mag)	$\log N_{\text{HI}}^c$ (Adopted)	$\log N_{\text{HI}}$ (SVS85)	$\log N_{\text{HI}}$ (DS94)	$\log N_{\text{HI}}$ (J19)	$\log N_{\text{HI}}^c$ (Other)
55	HD 99857	0.35	21.27		21.31 ± 0.12	$21.27^{+0.07}_{-0.03}$	
56	HD 99890	0.24	21.12		20.93 ± 0.13	$21.12^{+0.05}_{-0.07}$	
57	HD 100199	0.30	21.18			$21.18^{+0.06}_{-0.13}$	
58	HD 100213	0.34	21.18		21.18 ± 0.07		
59	HD 100276	0.28	21.19		21.19 ± 0.09		
60	HD 101131	0.31	21.15				21.15 (scaled)
61	HD 101190	0.36	21.24	21.04 ± 0.10	21.15 ± 0.11	$21.24^{+0.03}_{-0.06}$	
62	HD 101205	0.38	21.20		21.20 ± 0.07		
63	HD 101298	0.38	21.26		21.26 ± 0.11		
64	HD 101413	0.36	21.23		21.23 ± 0.13		
65	HD 101436	0.38	21.23		21.23 ± 0.08		
66	HD 103779	0.23	21.17		21.16 ± 0.10	$21.17^{+0.05}_{-0.05}$	
67	HD 104705	0.26	21.15		21.11 ± 0.07	$21.15^{+0.06}_{-0.05}$	
68	HD 115071	0.51	21.39		21.38 ± 0.10	$21.39^{+0.04}_{-0.09}$	
69	HD 116781	0.43	21.21			$21.21^{+0.05}_{-0.05}$	
70	HD 116852	0.22	20.96	20.95 ± 0.10	20.96 ± 0.08	$20.96^{+0.04}_{-0.04}$	
71	HD 118571	0.26	20.98				20.98 (scaled)
72	HD 124314A	0.53	21.41		21.34 ± 0.10	$21.41^{+0.06}_{-0.04}$	
73	HD 124979	0.41	21.27		21.30 ± 0.11	$21.27^{+0.09}_{-0.09}$	
74	HD 148422	0.35	21.24		21.15 ± 0.12	$21.24^{+0.09}_{-0.06}$	
75	HD 152218	0.48	21.34	21.34 ± 0.10	21.34 ± 0.12		
76	HD 152233	0.45	21.29	21.35 ± 0.10	21.29 ± 0.10		
77	HD 152248	0.47	21.37				21.37 (scaled)
78	HD 152314	0.50	21.35				21.35 (scaled)
79	HD 152623	0.40	21.28	21.11 ± 0.05	21.28 ± 0.10		
80	HD 152723	0.47	21.43		21.43 ± 0.13		
81	HD 153426	0.45	21.34		21.34 ± 0.13		
82	HD 154368	0.81	21.00				21.00 ± 0.05 (Sno96)
83	HD 156292	0.56	21.29				21.29 (scaled)
84	HD 157857	0.49	21.30		21.30 ± 0.09		
85	HD 158661	0.38	21.28				21.28 (scaled)
86	HD 161807	0.23	21.08				21.08 (scaled)
87	HD 163758	0.35	21.23	21.20 ± 0.10	21.23 ± 0.18		
88	HD 163892	0.46	21.32		21.32 ± 0.10		
89	HD 164816	0.31	21.18		21.18 ± 0.13		
90	HD 165052	0.42	21.36		21.36 ± 0.10		
91	HD 165246	0.40	21.41			$21.41^{+0.03}_{-0.04}$	
92	HD 166546	0.34	21.19				21.19 (scaled)
93	HD 166716	0.38	21.27				21.27 (scaled)
94	HD 167402	0.23	21.13		20.99 ± 0.13	$21.13^{+0.05}_{-0.04}$	
95	HD 167659	0.53	21.30		21.30 ± 0.12		
96	HD 167771	0.44	21.08		21.08 ± 0.12		21.10 ± 0.15 (FM90)
97	HD 167971	1.08	21.60				21.60 ± 0.30 (Rat02)
98	HD 168076	0.75	21.65		21.65 ± 0.23		
99	HD 168941	0.37	21.18		21.11 ± 0.09	$21.18^{+0.05}_{-0.07}$	
100	HD 172140	0.22	21.11		21.11 ± 0.08		
101	HD 175754	0.23	21.04	21.08 ± 0.05	21.04 ± 0.10		
102	HD 175876	0.21	21.04		21.04 ± 0.11		
103	HD 177989	0.25	20.99		20.95 ± 0.09	$20.99^{+0.05}_{-0.06}$	
104	HD 178487	0.40	21.22		21.15 ± 0.10	$21.22^{+0.04}_{-0.10}$	
105	HD 179406	0.33	21.23				21.23 ± 0.30 (Han92)
106	HD 179407	0.33	21.20		21.11 ± 0.11	$21.20^{+0.06}_{-0.10}$	
107	HD 185418	0.50	21.19			$21.19^{+0.05}_{-0.04}$	21.11 ± 0.15 (FM90)
108	HD 187459	0.44	21.31				21.31 (scaled)

Table 2—Continued

ID	Target (Star)	E_{B-V} ^b (mag)	$\log N_{\text{HI}}$ ^c (Adopted)	$\log N_{\text{HI}}$ (SVS85)	$\log N_{\text{HI}}$ (DS94)	$\log N_{\text{HI}}$ (J19)	$\log N_{\text{HI}}$ ^c (Other)
109	HD 190429A	0.43	21.33				21.33 (scaled)
110	HD 190918	0.45	21.40		21.40 ± 0.10		
111	HD 191495	0.40	21.32				21.32 (scaled)
112	HD 191877	0.21	21.03		20.90 ± 0.10	21.03 ^{+0.05} _{-0.05}	
113	HD 192035	0.34	21.20		21.09 ± 0.19	21.20 ^{+0.04} _{-0.10}	
114	HD 192639	0.66	21.32		21.32 ± 0.12		
115	HD 195965	0.25	20.92	20.95 ± 0.07	20.90 ± 0.09	20.92 ^{+0.05} _{-0.05}	
116	HD 199579	0.37	21.04	21.04 ± 0.10	21.04 ± 0.11		21.08 ± 0.15 (FM90)
117	HD 201345	0.15	21.00		20.88 ± 0.10	21.00 ^{+0.05} _{-0.06}	
118	HD 201638	0.11	20.80				20.80 (scaled)
119	HD 203374A	0.53	21.20			21.20 ^{+0.05} _{-0.04}	
120	HD 206267	0.53	21.22			21.22 ^{+0.06} _{-0.04}	21.30 ± 0.15 (Rat02)
121	HD 206773	0.51	21.09			21.09 ^{+0.07} _{-0.03}	
122	HD 207198	0.60	21.28	21.34 ± 0.15	21.34 ± 0.17	21.28 ^{+0.07} _{-0.09}	
123	HD 207308	0.53	21.20			21.20 ^{+0.06} _{-0.05}	
124	HD 208440	0.28	21.24		21.23 ± 0.07	21.24 ^{+0.06} _{-0.04}	
125	HD 209339	0.30	21.20			21.20 ^{+0.04} _{-0.04}	
126	HD 210809	0.34	21.31		21.26 ± 0.07	21.31 ^{+0.06} _{-0.05}	
127	HD 210839	0.57	21.24	21.20 ± 0.10	21.15 ± 0.12	21.24 ^{+0.05} _{-0.05}	
128	HD 216044	0.38	21.28				21.28 (scaled)
129	HD 216532	0.85	21.38				21.38 (scaled)
130	HD 216898	0.84	21.44				21.44 (scaled)
131	HD 217035	0.74	21.46		21.46 ± 0.12		
132	HD 217312	0.67	21.48		21.48 ± 0.09		
133	HD 218915	0.30	21.20	21.20 ± 0.10	21.11 ± 0.13	21.20 ^{+0.07} _{-0.06}	
134	HD 224151	0.44	21.35		21.32 ± 0.10	21.35 ^{+0.05} _{-0.08}	
135	HD 224257	0.24	21.08				21.08 (scaled)
136	HD 224868	0.34	21.16				21.16 (scaled)
137	HD 303308	0.46	21.41	21.40 ± 0.10	21.45 ± 0.09	21.41 ^{+0.03} _{-0.08}	
138	HD 308813	0.34	21.20		21.15 ± 0.10	21.20 ^{+0.06} _{-0.04}	
139	HD 332407	0.41	21.24		21.24 ± 0.14		

^aThe adopted column densities N_{HI} (in cm^{-2}) in column 4 (SD20) are compared to three previous Ly α -fitting surveys in columns 5–7: SVS85 (Shull & Van Steenberg 1985); DS94 (Diplas & Savage 1994); and J19 (Jenkins 2019). Column 8 lists individual measurements from: FM90 (Fitzpatrick & Massa 1990); Rat02 (Rachford et al. 2002); Han92 (Hanson et al. 1992); Sno96 (Snow et al. 1996); and scaled estimates of N_{HI} from $E(B - V)$. Footnote (c) to Table 3 provides further details.

^bUpdated values of color excess (Shull & Danforth 2019) were derived using digital photometry, visual extinction, and new SpTs from the Galactic O-star Spectroscopic Survey (Maíz Apellániz et al. 2004; Sota et al. 2011, 2014).

^cThe adopted source for N_{HI} was selected in priority order of: J19 (57 stars), DS94 (51 stars), FM90 (2 stars), and three other sources (3 stars). For 26 stars that lack fits to Ly α profiles, we estimated N_{HI} by scaling with color excess $E(B - V)$; see Section 2.1.

Table 3. Column Densities^a and Doppler Parameters^a

ID	Target	log N(0)	log N(1)	log N(2)	log N(3)	log N(4)	log N(5)	log N(6)	b (km s ⁻¹)
1	BD 35°4258	19.03 ^{+0.10} _{-0.10}	19.39 ^{+0.10} _{-0.10}	17.72 ^{+0.21} _{-0.30}	17.78 ^{+0.23} _{-0.32}	15.68 ^{+0.20} _{-0.14}	15.36 ^{+0.17} _{-0.12}	14.14 ^{+0.18} _{-0.18}	8.4 ^{+0.9} _{-1.0}
2	BD 53°2820	19.59 ^{+0.10} _{-0.10}	19.85 ^{+0.10} _{-0.10}	16.07 ^{+0.40} _{-0.40}	15.85 ^{+0.4} _{-0.4}	15.25 ^{+0.04} _{-0.02}	14.95 ^{+0.03} _{-0.02}	< 14.15	20 ^{+1.0} _{-1.0}
3	CPD -59°2600	19.84 ^{+0.10} _{-0.10}	19.88 ^{+0.10} _{-0.10}	16.66 ^{+0.46} _{-0.32}	16.39 ^{+0.36} _{-0.20}	15.06 ^{+0.10} _{-0.07}	14.89 ^{+0.08} _{-0.06}	14.04 ^{+0.10} _{-0.10}	8.4 ^{+0.9} _{-1.0}
4	CPD -59°2603	19.77 ^{+0.05} _{-0.05}	19.87 ^{+0.10} _{-0.10}	18.23 ^{+0.50} _{-0.50}	15.65 ^{+0.11} _{-0.73}	14.88 ^{+0.05} _{-0.05}	14.76 ^{+0.06} _{-0.06}	13.94 ^{+0.18} _{-0.18}	11.3 ^{+0.9} _{-1.0}
5	CPD -69°1743	19.49 ^{+0.10} _{-0.10}	19.71 ^{+0.10} _{-0.10}	15.78 ^{+0.12} _{-0.08}	15.51 ^{+0.10} _{-0.08}	14.68 ^{+0.09} _{-0.09}	14.39 ^{+0.04} _{-0.04}	< 13.85	13.3 ^{+0.9} _{-1.0}
6	CPD -72°1184	19.59 ^{+0.10} _{-0.10}	19.90 ^{+0.10} _{-0.10}	17.24 ^{+0.70} _{-0.50}	16.04 ^{+1.43} _{-0.20}	14.56 ^{+1.38} _{-0.03}	< 14.30	< 14.10	...
7	HD 3827	16.84 ^{+0.05} _{-0.05}	17.33 ^{+0.05} _{-0.05}	16.15 ^{+0.20} _{-0.13}	15.82 ^{+0.14} _{-0.10}	14.55 ^{+0.06} _{-0.06}	14.16 ^{+0.09} _{-0.09}	< 13.85	12.8 ^{+0.9} _{-1.0}
8	HD 5005A	19.87 ^{+0.05} _{-0.05}	19.96 ^{+0.05} _{-0.05}	18.16 ^{+0.50} _{-0.50}	17.14 ^{+0.27} _{-0.68}	15.46 ^{+0.04} _{-0.09}	15.00 ^{+0.07} _{-0.07}	14.08 ^{+0.10} _{-0.10}	15.0 ^{+3.6} _{-1.0}
9	HD 12323	19.92 ^{+0.10} _{-0.10}	20.08 ^{+0.10} _{-0.10}	18.01 ^{+0.25} _{-0.18}	17.35 ^{+0.37} _{-0.45}	15.45 ^{+0.15} _{-0.23}	14.81 ^{+0.06} _{-0.06}	< 14.00	7.4 ^{+1.0} _{-1.0}
10	HD 13268 ^b	20.00 ^{+0.10} _{-0.10}	20.29 ^{+0.10} _{-0.10}	18.08 ^{+0.50} _{-0.50}	17.23 ^{+0.50} _{-0.50}	15.53 ^{+0.03} _{-0.03}	15.18 ^{+0.03} _{-0.03}	< 14.00	...
	(blue)	14.75 ^{+0.04} _{-0.04}	14.52 ^{+0.04} _{-0.04}	...	15.6 ^{+4.4} _{-1.0}
	(red)	15.45 ^{+0.04} _{-0.04}	15.07 ^{+0.04} _{-0.04}	...	13.2 ^{+0.9} _{-1.0}
11	HD 13745 ^b	20.30 ^{+0.10} _{-0.10}	20.27 ^{+0.10} _{-0.10}	18.74 ^{+0.50} _{-0.50}	17.38 ^{+0.35} _{-0.33}	15.74 ^{+1.77} _{-0.06}	15.09 ^{+0.69} _{-0.03}	< 14.00	...
	(blue)	17.27 ^{+0.44} _{-0.46}	15.07 ^{+0.87} _{-0.16}	14.29 ^{+1.05} _{-0.04}	...	3.9 ^{+1.0} _{-2.9}
	(red)	16.74 ^{+0.38} _{-0.28}	15.63 ^{+0.08} _{-0.06}	15.02 ^{+0.04} _{-0.04}	...	9.6 ^{+0.9} _{-1.0}
12	HD 14434 ^b	20.04 ^{+0.10} _{-0.10}	20.36 ^{+0.10} _{-0.10}	18.94 ^{+0.50} _{-0.50}	17.06 ^{+0.27} _{-0.20}	15.59 ^{+0.05} _{-0.03}	15.12 ^{+0.03} _{-0.03}	< 14.00	...
	(blue)	16.93 ^{+0.35} _{-0.27}	15.17 ^{+0.04} _{-0.04}	14.88 ^{+0.04} _{-0.04}
	(red)	16.50 ^{+0.37} _{-0.24}	15.38 ^{+0.08} _{-0.05}	14.74 ^{+0.04} _{-0.04}
13	HD 15137	19.77 ^{+0.05} _{-0.05}	20.10 ^{+0.05} _{-0.05}	17.55 ^{+0.33} _{-0.35}	16.74 ^{+0.30} _{-0.20}	15.44 ^{+0.08} _{-0.11}	14.58 ^{+0.05} _{-0.04}	...	9.5 ^{+0.9} _{-1.0}
14	HD 15558A	20.50 ^{+0.15} _{-0.15}	20.66 ^{+0.10} _{-0.10}	19.04 ^{+0.50} _{-0.50}	17.39 ^{+0.29} _{-0.26}	15.70 ^{+0.09} _{-0.07}	15.36 ^{+0.06} _{-0.05}	< 14.60	12.6 ^{+0.9} _{-1.0}
15	HD 15642 ^b	19.61 ^{+0.10} _{-0.10}	20.10 ^{+0.10} _{-0.10}	19.64 ^{+0.50} _{-0.50}	18.14 ^{+0.50} _{-0.50}	15.58 ^{+0.21} _{-0.04}	14.88 ^{+0.04} _{-0.04}	< 14.00	...
	(blue)	14.46 ^{+0.04} _{-0.04}	13.88 ^{+0.04} _{-0.04}
	(red)	15.58 ^{+0.21} _{-0.12}	14.88 ^{+0.04} _{-0.04}
16	HD 34656	19.80 ^{+0.05} _{-0.05}	19.97 ^{+0.05} _{-0.05}	17.16 ^{+0.50} _{-0.50}	16.86 ^{+0.37} _{-0.28}	15.28 ^{+0.06} _{-0.06}	14.71 ^{+0.04} _{-0.04}	< 13.95	10.8 ^{+0.9} _{-1.0}
17	HD 39680	19.16 ^{+0.05} _{-0.05}	19.29 ^{+0.05} _{-0.05}	16.82 ^{+0.54} _{-0.47}	16.37 ^{+0.48} _{-0.24}	14.83 ^{+0.10} _{-0.05}	14.20 ^{+0.04} _{-0.04}	< 14.15	6.3 ^{+1.0} _{-1.0}
18	HD 41161	19.62 ^{+0.15} _{-0.15}	19.80 ^{+0.15} _{-0.15}	17.58 ^{+0.50} _{-0.50}	17.01 ^{+0.40} _{-0.36}	14.97 ^{+0.09} _{-0.06}	14.28 ^{+0.04} _{-0.05}	< 14.15	7.7 ^{+0.9} _{-1.0}
19	HD 42088	20.18 ^{+0.05} _{-0.05}	20.23 ^{+0.05} _{-0.05}	17.77 ^{+0.25} _{-0.36}	17.22 ^{+0.41} _{-0.41}	15.34 ^{+0.12} _{-0.09}	14.90 ^{+0.05} _{-0.06}	< 13.70	7.5 ^{+0.9} _{-1.0}
20	HD 45314	20.23 ^{+0.05} _{-0.05}	20.35 ^{+0.05} _{-0.05}	18.05 ^{+0.11} _{-0.18}	17.28 ^{+0.33} _{-0.46}	15.09 ^{+0.10} _{-0.08}	14.30 ^{+0.04} _{-0.04}	< 14.08	6.2 ^{+1.0} _{-1.0}
21	HD 46150	20.23 ^{+0.05} _{-0.05}	20.42 ^{+0.05} _{-0.05}	16.91 ^{+0.39} _{-0.28}	16.36 ^{+0.30} _{-0.21}	15.30 ^{+0.07} _{-0.06}	14.87 ^{+0.05} _{-0.04}	13.76 ^{+0.15} _{-0.15}	10.8 ^{+0.9} _{-1.0}
22	HD 47360	20.02 ^{+0.10} _{-0.10}	20.13 ^{+0.10} _{-0.10}	17.71 ^{+0.21} _{-0.32}	16.55 ^{+0.54} _{-0.43}	15.31 ^{+0.16} _{-0.11}	14.78 ^{+0.08} _{-0.06}	< 14.00	6.8 ^{+1.0} _{-1.0}
23	HD 47417	20.15 ^{+0.05} _{-0.05}	20.27 ^{+0.05} _{-0.05}	17.74 ^{+0.22} _{-0.28}	17.20 ^{+0.35} _{-0.32}	15.29 ^{+0.06} _{-0.04}	14.73 ^{+0.05} _{-0.05}	< 14.08	9.0 ^{+0.9} _{-1.0}
24	HD 60369	20.25 ^{+0.05} _{-0.05}	20.10 ^{+0.05} _{-0.05}	17.96 ^{+0.15} _{-0.15}	17.66 ^{+0.23} _{-0.29}	15.50 ^{+0.07} _{-0.10}	14.90 ^{+0.05} _{-0.05}	< 13.85	5.3 ^{+1.0} _{-1.1}
25	HD 61347 ^b	20.27 ^{+0.10} _{-0.10}	20.31 ^{+0.10} _{-0.10}	18.74 ^{+0.50} _{-0.50}	17.41 ^{+0.62} _{-0.40}	15.48 ^{+0.50} _{-0.06}	14.88 ^{+0.75} _{-0.03}	< 14.20	...
	(blue)	15.53 ^{+1.80} _{-0.24}	14.96 ^{+0.40} _{-0.09}	14.25 ^{+1.0} _{-0.04}
	(red)	17.41 ^{+0.62} _{-0.40}	15.48 ^{+0.50} _{-0.06}	14.88 ^{+0.75} _{-0.04}
26	HD 62866	19.80 ^{+0.10} _{-0.10}	20.04 ^{+0.10} _{-0.10}	16.65 ^{+0.40} _{-0.40}	16.27 ^{+0.13} _{-0.17}	15.36 ^{+0.05} _{-0.07}	14.95 ^{+0.04} _{-0.04}	< 14.30	17.7 ^{+2.2} _{-1.0}
27	HD 63005	19.68 ^{+0.10} _{-0.10}	19.97 ^{+0.10} _{-0.10}	17.73 ^{+0.15} _{-0.25}	17.04 ^{+0.36} _{-0.48}	15.22 ^{+0.17} _{-0.11}	14.59 ^{+0.06} _{-0.05}	< 14.01	5.4 ^{+0.9} _{-0.8}
28	HD 64568	20.35 ^{+0.10} _{-0.10}	20.10 ^{+0.10} _{-0.10}	16.67 ^{+0.40} _{-0.40}	16.51 ^{+0.15} _{-0.21}	15.34 ^{+0.05} _{-0.06}	14.96 ^{+0.04} _{-0.04}	< 14.10	15.9 ^{+2.7} _{-1.0}
29	HD 66695	19.82 ^{+0.10} _{-0.10}	19.79 ^{+0.10} _{-0.10}	18.21 ^{+0.11} _{-0.11}	17.96 ^{+0.16} _{-0.20}	16.02 ^{+0.47} _{-0.26}	15.82 ^{+0.48} _{-0.29}	< 14.00	6.8 ^{+1.0} _{-1.0}
30	HD 66788	19.33 ^{+0.05} _{-0.05}	19.42 ^{+0.05} _{-0.05}	18.40 ^{+0.06} _{-0.09}	18.24 ^{+0.09} _{-0.14}	15.46 ^{+0.20} _{-0.13}	14.65 ^{+0.04} _{-0.04}	< 14.18	6.4 ^{+1.0} _{-0.9}
31	HD 69106	19.41 ^{+0.10} _{-0.10}	19.44 ^{+0.10} _{-0.10}	17.77 ^{+0.50} _{-0.50}	17.61 ^{+0.28} _{-0.33}	15.38 ^{+0.13} _{-0.10}	14.46 ^{+0.04} _{-0.04}	< 14.11	9.6 ^{+0.9} _{-1.0}
32	HD 73882	21.00 ^{+0.15} _{-0.15}	20.55 ^{+0.15} _{-0.15}	16.61 ^{+0.40} _{-0.40}	16.04 ^{+0.08} _{-0.08}	15.13 ^{+0.02} _{-0.02}	15.28 ^{+0.20} _{-0.20}	< 14.40	18.6 ^{+1.3} _{-1.0}
33	HD 74194	20.14 ^{+0.10} _{-0.10}	20.33 ^{+0.10} _{-0.10}	18.05 ^{+0.12} _{-0.15}	17.25 ^{+0.40} _{-0.47}	15.45 ^{+0.33} _{-0.12}	14.93 ^{+0.07} _{-0.05}	< 14.00	5.7 ^{+1.0} _{-1.0}
34	HD 74920	19.77 ^{+0.05} _{-0.05}	20.09 ^{+0.05} _{-0.05}	16.42 ^{+0.37} _{-0.24}	16.06 ^{+0.26} _{-0.16}	15.01 ^{+0.07} _{-0.05}	14.60 ^{+0.09} _{-0.09}	13.85 ^{+0.20} _{-0.20}	8.9 ^{+0.9} _{-1.0}
35	HD 89137	19.53 ^{+0.05} _{-0.05}	19.81 ^{+0.05} _{-0.05}	16.12 ^{+0.15} _{-0.15}	15.70 ^{+0.10} _{-0.10}	14.70 ^{+0.12} _{-0.04}	14.28 ^{+0.12} _{-0.12}	< 13.85	9.6 ^{+0.9} _{-1.0}
36	HD 90087	19.53 ^{+0.05} _{-0.05}	19.68 ^{+0.05} _{-0.05}	17.57 ^{+0.23} _{-0.37}	16.87 ^{+0.41} _{-0.29}	15.36 ^{+0.12} _{-0.09}	14.79 ^{+0.05} _{-0.04}	13.63 ^{+0.04} _{-0.04}	7.3 ^{+1.0} _{-0.9}
37	HD 91597	19.45 ^{+0.10} _{-0.10}	19.33 ^{+0.10} _{-0.10}	16.20 ^{+0.27} _{-0.17}	16.03 ^{+0.33} _{-0.15}	15.11 ^{+0.05} _{-0.05}	14.83 ^{+0.04} _{-0.04}	< 14.00	10.9 ^{+0.9} _{-1.0}
38	HD 91651	18.74 ^{+0.05} _{-0.05}	18.79 ^{+0.05} _{-0.05}	16.35 ^{+0.28} _{-0.19}	16.53 ^{+0.33} _{-0.24}	15.37 ^{+0.08} _{-0.06}	15.11 ^{+0.06} _{-0.05}	14.06 ^{+0.08} _{-0.08}	10.9 ^{+0.9} _{-1.0}
39	HD 91824	19.61 ^{+0.05} _{-0.05}	19.43 ^{+0.05} _{-0.05}	17.72 ^{+0.50} _{-0.50}	17.17 ^{+0.38} _{-0.42}	15.24 ^{+0.09} _{-0.07}	14.64 ^{+0.04} _{-0.04}	< 14.00	7.4 ^{+1.0} _{-1.0}
40	HD 92554	18.88 ^{+0.10} _{-0.10}	17.98 ^{+0.10} _{-0.10}	15.94 ^{+0.10} _{-0.10}	15.91 ^{+0.10} _{-0.10}	14.98 ^{+0.04} _{-0.04}	14.86 ^{+0.04} _{-0.04}	14.27 ^{+0.08} _{-0.08}	13.4 ^{+0.9} _{-1.0}
41	HD 93028	19.08 ^{+0.10} _{-0.10}	19.37 ^{+0.10} _{-0.10}	15.98 ^{+0.20} _{-0.11}	15.73 ^{+0.19} _{-0.11}	14.72 ^{+0.04} _{-0.04}	14.22 ^{+0.09} _{-0.09}	< 14.00	9.1 ^{+0.9} _{-1.0}
42	HD 93129A	19.68 ^{+0.10} _{-0.10}	20.06 ^{+0.10} _{-0.10}	17.47 ^{+0.36} _{-0.39}	17.88 ^{+0.30} _{-0.30}	15.72 ^{+0.29} _{-0.16}	15.36 ^{+0.14} _{-0.09}	14.05 ^{+0.08} _{-0.08}	8.7 ^{+0.9} _{-1.0}
43	HD 93146A	19.38 ^{+0.10} _{-0.10}	19.43 ^{+0.10} _{-0.10}	15.97 ^{+0.24} _{-0.16}	15.78 ^{+0.21} _{-0.13}	14.79 ^{+0.05} _{-0.04}	14.56 ^{+0.04} _{-0.04}	14.14 ^{+0.15} _{-0.15}	9.1 ^{+0.9} _{-1.0}
44	HD 93204	19.37 ^{+0.05} _{-0.05}	19.62 ^{+0.05} _{-0.05}	16.11 ^{+0.29} _{-0.16}	15.88 ^{+0.24} _{-0.12}	14.86 ^{+0.06} _{-0.04}	14.51 ^{+0.04} _{-0.04}	< 13.85	9.2 ^{+0.9} _{-1.0}
45	HD 93205 ^b	19.33 ^{+0.05} _{-0.05}	19.61 ^{+0.05} _{-0.05}	16.47 ^{+0.44} _{-0.28}	16.29 ^{+0.37} _{-0.18}	14.92 ^{+0.05} _{-0.04}	14.59 ^{+0.06} _{-0.04}	< 13.85	...

Table 3—Continued

ID	Target	log N(0)	log N(1)	log N(2)	log N(3)	log N(4)	log N(5)	log N(6)	b (km s ⁻¹)
	(blue)	14.36 ^{+0.55} _{-0.12}	14.93 ^{+1.10} _{-0.36}	13.95 ^{+0.23} _{-0.06}	13.96 ^{+0.17} _{-0.05}
	(red)	16.47 ^{+0.44} _{-0.28}	16.27 ^{+0.36} _{-0.13}	14.87 ^{+0.05} _{-0.04}	14.48 ^{+0.04} _{-0.04}
46	HD 93206	19.18 ^{+0.05} _{-0.05}	19.25 ^{+0.05} _{-0.05}	15.87 ^{+0.24} _{-0.13}	15.78 ^{+0.25} _{-0.07}	14.48 ^{+0.04} _{-0.04}	14.10 ^{+0.04} _{-0.04}	< 13.85	8.2 ^{+0.9} _{-1.0}
47	HD 93222	19.49 ^{+0.05} _{-0.05}	19.44 ^{+0.05} _{-0.05}	15.80 ^{+0.08} _{-0.06}	15.70 ^{+0.09} _{-0.07}	14.71 ^{+0.04} _{-0.04}	14.46 ^{+0.04} _{-0.04}	< 14.15	12.9 ^{+0.9} _{-1.0}
48	HD 93250	19.79 ^{+0.05} _{-0.05}	20.10 ^{+0.05} _{-0.05}	16.37 ^{+0.41} _{-0.07}	16.68 ^{+0.24} _{-0.07}	15.75 ^{+0.19} _{-0.07}	15.89 ^{+0.19} _{-0.12}	15.59 ^{+0.15} _{-0.15}	15.4 ^{+0.9} _{-1.0}
49	HD 93843	19.14 ^{+0.05} _{-0.05}	19.43 ^{+0.05} _{-0.05}	16.04 ^{+0.08} _{-0.08}	15.86 ^{+0.05} _{-0.06}	14.67 ^{+0.04} _{-0.04}	14.40 ^{+0.04} _{-0.04}	< 13.78	14.6 ^{+0.9} _{-1.0}
50	HD 96670	20.33 ^{+0.10} _{-0.10}	20.24 ^{+0.10} _{-0.10}	18.56 ^{+0.50} _{-0.50}	16.70 ^{+0.29} _{-0.33}	15.74 ^{+0.18} _{-0.12}	15.00 ^{+0.08} _{-0.06}	< 14.00	9.1 ^{+0.9} _{-1.0}
51	HD 96715	20.45 ^{+0.10} _{-0.10}	20.11 ^{+0.10} _{-0.10}	18.53 ^{+0.50} _{-0.50}	17.15 ^{+0.29} _{-0.27}	15.66 ^{+0.07} _{-0.05}	14.82 ^{+0.04} _{-0.04}	< 14.10	10.1 ^{+0.9} _{-0.9}
52	HD 96917 ^c	20.04 ^{+0.10} _{-0.10}	19.83 ^{+0.10} _{-0.10}	16.18 ^{+0.12} _{-0.12}	15.43 ^{+0.15} _{-0.15}	14.43 ^{+0.05} _{-0.05}	12.0 ^{+3.0} _{-1.0}
53	HD 97471	19.67 ^{+0.10} _{-0.10}	19.52 ^{+0.10} _{-0.10}	17.15 ^{+0.36} _{-0.31}	16.74 ^{+0.37} _{-0.27}	15.33 ^{+0.11} _{-0.09}	14.77 ^{+0.04} _{-0.04}	< 13.95	10.6 ^{+0.9} _{-1.0}
54	HD 97913	19.76 ^{+0.10} _{-0.10}	19.89 ^{+0.10} _{-0.10}	16.96 ^{+0.30} _{-0.30}	16.46 ^{+0.23} _{-0.23}	15.32 ^{+0.06} _{-0.06}	14.69 ^{+0.04} _{-0.04}	13.90 ^{+0.10} _{-0.10}	10.5 ^{+1.0} _{-1.0}
55	HD 99857	19.90 ^{+0.10} _{-0.10}	20.01 ^{+0.10} _{-0.10}	18.19 ^{+0.08} _{-0.11}	17.78 ^{+0.15} _{-0.26}	15.05 ^{+0.09} _{-0.07}	14.46 ^{+0.04} _{-0.04}	< 14.04	5.7 ^{+1.0} _{-0.8}
56	HD 99890	19.09 ^{+0.10} _{-0.10}	19.23 ^{+0.10} _{-0.10}	16.84 ^{+0.40} _{-0.27}	16.66 ^{+0.38} _{-0.25}	15.01 ^{+0.08} _{-0.06}	14.56 ^{+0.04} _{-0.04}	< 13.85	9.4 ^{+0.9} _{-0.9}
57	HD 100199	19.76 ^{+0.10} _{-0.10}	19.96 ^{+0.10} _{-0.10}	17.66 ^{+0.24} _{-0.34}	17.11 ^{+0.25} _{-0.35}	15.35 ^{+0.11} _{-0.09}	14.75 ^{+0.05} _{-0.04}	< 14.08	8.4 ^{+0.9} _{-1.0}
58	HD 100213	20.11 ^{+0.10} _{-0.10}	20.13 ^{+0.10} _{-0.10}	18.22 ^{+0.11} _{-0.17}	17.61 ^{+0.25} _{-0.41}	15.33 ^{+0.11} _{-0.10}	14.65 ^{+0.05} _{-0.05}	< 13.98	7.2 ^{+1.0} _{-1.0}
59	HD 100276	19.49 ^{+0.10} _{-0.10}	19.57 ^{+0.10} _{-0.10}	16.44 ^{+0.15} _{-0.16}	16.02 ^{+0.11} _{-0.12}	15.07 ^{+0.04} _{-0.04}	15.05 ^{+0.04} _{-0.04}	< 14.10	17.0 ^{+2.0} _{-1.0}
60	HD 101131	19.92 ^{+0.05} _{-0.05}	20.02 ^{+0.05} _{-0.05}	18.10 ^{+0.08} _{-0.21}	17.70 ^{+0.15} _{-0.38}	15.27 ^{+0.06} _{-0.10}	14.59 ^{+0.06} _{-0.06}	< 14.18	7.1 ^{+1.0} _{-0.6}
61	HD 101190	20.21 ^{+0.05} _{-0.05}	20.00 ^{+0.05} _{-0.05}	18.33 ^{+0.03} _{-0.07}	17.81 ^{+0.08} _{-0.18}	15.16 ^{+0.05} _{-0.03}	14.44 ^{+0.04} _{-0.04}	< 13.95	4.9 ^{+0.9} _{-0.4}
62	HD 101205	19.94 ^{+0.15} _{-0.15}	19.96 ^{+0.15} _{-0.15}	18.48 ^{+0.10} _{-0.10}	17.98 ^{+0.07} _{-0.23}	15.45 ^{+0.33} _{-0.17}	14.60 ^{+0.06} _{-0.05}	< 14.18	6.2 ^{+1.0} _{-1.0}
63	HD 101298	20.23 ^{+0.10} _{-0.10}	20.04 ^{+0.10} _{-0.10}	16.99 ^{+0.40} _{-0.40}	17.94 ^{+0.11} _{-0.16}	15.28 ^{+0.09} _{-0.06}	14.54 ^{+0.05} _{-0.04}	< 13.95	5.4 ^{+0.9} _{-0.7}
64	HD 101413	20.30 ^{+0.10} _{-0.10}	20.08 ^{+0.10} _{-0.10}	18.74 ^{+0.50} _{-0.50}	17.35 ^{+0.39} _{-0.32}	14.95 ^{+0.15} _{-0.15}	14.32 ^{+0.08} _{-0.08}	< 14.22	4.0 ^{+1.0} _{-0.7}
65	HD 101436 ^b	20.34 ^{+0.05} _{-0.05}	20.09 ^{+0.05} _{-0.05}	18.53 ^{+0.50} _{-0.50}	17.50 ^{+0.70} _{-0.55}	15.51 ^{+0.14} _{-0.10}	14.41 ^{+0.03} _{-0.03}	< 13.90	...
	(blue)	15.49 ^{+1.87} _{-0.18}	14.29 ^{+0.56} _{-0.04}	5.3 ^{+1.0} _{-3.7}
	(red)	17.50 ^{+0.09} _{-0.16}	15.48 ^{+0.14} _{-0.11}	14.41 ^{+0.04} _{-0.04}	...	3.3 ^{+0.5} _{-0.4}
66	HD 103779	19.33 ^{+0.10} _{-0.10}	19.65 ^{+0.10} _{-0.10}	16.25 ^{+0.15} _{-0.09}	15.83 ^{+0.10} _{-0.07}	14.81 ^{+0.04} _{-0.04}	14.75 ^{+0.10} _{-0.10}	< 13.88	13 ^{+0.9} _{-1.0}
67	HD 104705 ^b	19.57 ^{+0.05} _{-0.05}	19.77 ^{+0.05} _{-0.05}	17.87 ^{+0.08} _{-0.06}	17.28 ^{+0.18} _{-0.12}	15.21 ^{+0.30} _{-0.15}	14.46 ^{+0.05} _{-0.03}	< 13.95	...
	(blue)	15.85 ^{+0.25} _{-0.14}	15.30 ^{+0.15} _{-0.08}	14.01 ^{+0.04} _{-0.04}	7.1 ^{+1.0} _{-1.0}
	(red)	17.87 ^{+0.08} _{-0.06}	17.28 ^{+0.18} _{-0.13}	15.18 ^{+0.31} _{-0.09}	14.46 ^{+0.05} _{-0.04}	...	3.4 ^{+0.3} _{-0.6}
68	HD 115071	20.30 ^{+0.10} _{-0.10}	20.37 ^{+0.10} _{-0.10}	18.30 ^{+0.22} _{-0.22}	16.86 ^{+0.38} _{-0.29}	15.55 ^{+0.10} _{-0.08}	14.93 ^{+0.05} _{-0.04}	< 13.90	10.2 ^{+0.9} _{-1.0}
69	HD 116781	19.56 ^{+0.10} _{-0.10}	19.89 ^{+0.10} _{-0.10}	17.90 ^{+0.19} _{-0.25}	17.55 ^{+0.29} _{-0.37}	15.19 ^{+0.11} _{-0.08}	14.61 ^{+0.05} _{-0.04}	< 14.00	8.5 ^{+0.9} _{-1.0}
70	HD 116852	19.50 ^{+0.05} _{-0.05}	19.46 ^{+0.05} _{-0.05}	15.99 ^{+0.37} _{-0.20}	15.81 ^{+0.32} _{-0.18}	14.64 ^{+0.04} _{-0.04}	14.00 ^{+0.18} _{-0.18}	< 13.85	7.1 ^{+1.0} _{-1.0}
71	HD 118571	19.86 ^{+0.05} _{-0.05}	20.03 ^{+0.05} _{-0.05}	17.97 ^{+0.16} _{-0.30}	17.65 ^{+0.23} _{-0.39}	15.27 ^{+0.12} _{-0.11}	14.50 ^{+0.04} _{-0.04}	< 14.04	7.5 ^{+1.0} _{-0.9}
72	HD 124314A	20.17 ^{+0.05} _{-0.05}	20.16 ^{+0.05} _{-0.05}	18.03 ^{+0.15} _{-0.22}	16.99 ^{+0.39} _{-0.34}	15.53 ^{+0.13} _{-0.10}	14.75 ^{+0.04} _{-0.04}	< 13.64	9.1 ^{+0.9} _{-0.9}
73	HD 124979	20.02 ^{+0.10} _{-0.10}	20.18 ^{+0.10} _{-0.10}	18.21 ^{+0.15} _{-0.20}	17.46 ^{+0.32} _{-0.33}	15.51 ^{+0.09} _{-0.08}	14.84 ^{+0.04} _{-0.04}	< 13.90	10.0 ^{+0.9} _{-1.0}
74	HD 148422 ^c	19.93 ^{+0.15} _{-0.15}	19.70 ^{+0.15} _{-0.15}	15.04 ^{+0.12} _{-0.12}	14.30 ^{+0.20} _{-0.20}	< 14.30	...
75	HD 152218	20.32 ^{+0.10} _{-0.10}	20.20 ^{+0.10} _{-0.10}	18.33 ^{+0.11} _{-0.14}	17.50 ^{+0.31} _{-0.42}	15.83 ^{+0.44} _{-0.26}	15.14 ^{+0.13} _{-0.09}	13.93 ^{+0.15} _{-0.15}	7.0 ^{+1.0} _{-1.0}
76	HD 152233	20.01 ^{+0.10} _{-0.10}	19.95 ^{+0.10} _{-0.10}	18.31 ^{+0.06} _{-0.08}	18.11 ^{+0.07} _{-0.10}	16.93 ^{+0.40} _{-0.57}	15.39 ^{+0.47} _{-0.21}	14.02 ^{+0.08} _{-0.08}	4.3 ^{+0.9} _{-0.9}
77	HD 152248	20.01 ^{+0.10} _{-0.10}	19.95 ^{+0.10} _{-0.10}	18.37 ^{+0.09} _{-0.08}	18.14 ^{+0.13} _{-0.14}	16.84 ^{+0.71} _{-0.59}	15.36 ^{+1.40} _{-0.24}	< 13.90	4.9 ^{+0.9} _{-2.1}
78	HD 152314 ^c	20.27 ^{+0.10} _{-0.10}	20.14 ^{+0.10} _{-0.10}	15.70 ^{+0.18} _{-0.18}	15.00 ^{+0.08} _{-0.08}	< 13.90	7.0 ^{+1.0} _{-1.0}
79	HD 152623	19.88 ^{+0.10} _{-0.10}	19.93 ^{+0.10} _{-0.10}	16.58 ^{+0.33} _{-0.26}	16.34 ^{+0.29} _{-0.23}	15.27 ^{+0.08} _{-0.06}	14.84 ^{+0.05} _{-0.04}	13.65 ^{+0.10} _{-0.10}	10.4 ^{+0.9} _{-1.0}
80	HD 152723	19.97 ^{+0.10} _{-0.10}	19.99 ^{+0.10} _{-0.10}	18.12 ^{+0.11} _{-0.16}	17.83 ^{+0.16} _{-0.26}	15.49 ^{+0.30} _{-0.15}	14.84 ^{+0.08} _{-0.06}	13.70 ^{+0.10} _{-0.10}	5.9 ^{+0.9} _{-0.9}
81	HD 153426	19.91 ^{+0.10} _{-0.10}	20.07 ^{+0.10} _{-0.10}	17.74 ^{+0.18} _{-0.22}	17.11 ^{+0.32} _{-0.40}	15.39 ^{+0.69} _{-0.19}	14.86 ^{+0.22} _{-0.09}	< 13.81	6.5 ^{+0.9} _{-1.4}
82	HD 154368 ^c	21.02 ^{+0.15} _{-0.15}	20.62 ^{+0.10} _{-0.10}	15.41 ^{+0.18} _{-0.18}	14.86 ^{+0.8} _{-0.08}
83	HD 156292	20.41 ^{+0.10} _{-0.10}	20.58 ^{+0.10} _{-0.10}	18.04 ^{+0.21} _{-0.24}	16.56 ^{+0.39} _{-0.28}	15.47 ^{+0.10} _{-0.07}	14.88 ^{+0.05} _{-0.05}	< 13.78	9.4 ^{+0.9} _{-1.0}
84	HD 157857	20.31 ^{+0.10} _{-0.10}	20.32 ^{+0.10} _{-0.10}	18.50 ^{+0.09} _{-0.16}	17.73 ^{+0.23} _{-0.36}	15.36 ^{+0.12} _{-0.09}	14.80 ^{+0.05} _{-0.06}	< 14.11	7.1 ^{+1.0} _{-1.0}
85	HD 158661	19.89 ^{+0.10} _{-0.10}	19.83 ^{+0.10} _{-0.10}	18.35 ^{+0.13} _{-0.15}	17.75 ^{+0.24} _{-0.29}	15.96 ^{+0.39} _{-0.24}	15.51 ^{+0.19} _{-0.12}	< 14.10	8.2 ^{+0.9} _{-1.0}
86	HD 161807	19.35 ^{+0.05} _{-0.05}	19.69 ^{+0.05} _{-0.05}	17.73 ^{+0.17} _{-0.34}	17.27 ^{+0.49} _{-0.49}	15.00 ^{+0.08} _{-0.08}	14.43 ^{+0.04} _{-0.04}	< 13.90	6.4 ^{+0.8} _{-0.8}
87	HD 163758	19.53 ^{+0.10} _{-0.10}	19.56 ^{+0.10} _{-0.10}	17.93 ^{+0.19} _{-0.26}	18.06 ^{+0.18} _{-0.25}	15.82 ^{+0.31} _{-0.19}	15.31 ^{+0.07} _{-0.06}	14.05 ^{+0.07} _{-0.07}	9.0 ^{+0.9} _{-1.0}
88	HD 163892	20.38 ^{+0.10} _{-0.10}	20.14 ^{+0.10} _{-0.10}	17.88 ^{+0.12} _{-0.12}	17.26 ^{+0.30} _{-0.30}	15.92 ^{+0.48} _{-0.22}	15.43 ^{+0.19} _{-0.09}	14.23 ^{+0.04} _{-0.04}	5.2 ^{+0.6} _{-0.8}
89	HD 164816	19.69 ^{+0.10} _{-0.10}	19.70 ^{+0.10} _{-0.10}	17.55 ^{+0.07} _{-0.09}	17.11 ^{+0.16} _{-0.22}	14.93 ^{+0.24} _{-0.14}	14.60 ^{+0.09} _{-0.06}	< 14.30	2.8 ^{+0.8} _{-0.4}
90	HD 165052	19.78 ^{+0.05} _{-0.05}	19.99 ^{+0.05} _{-0.05}	17.82 ^{+0.19} _{-0.29}	17.43 ^{+0.32} _{-0.39}	15.36 ^{+0.16} _{-0.12}	14.59 ^{+0.04} _{-0.04}	< 14.00	7.7 ^{+0.9} _{-0.9}
91	HD 165246	19.83 ^{+0.10} _{-0.10}	19.89 ^{+0.10} _{-0.10}	15.59 ^{+0.13} _{-0.13}	15.44 ^{+0.06} _{-0.06}	14.66 ^{+0.05} _{-0.05}	14.35 ^{+0.13} _{-0.13}	< 14.08	8.7 ^{+0.9} _{-1.0}
92	HD 166546 ^b	19.99 ^{+0.10} _{-0.10}	20.05 ^{+0.10} _{-0.10}	18.01 ^{+0.19} _{-0.23}	17.54 ^{+0.32} _{-0.37}	15.60 ^{+0.26} _{-0.07}	15.17 ^{+0.07} _{-0.03}	14.20 ^{+0.10} _{-0.20}	...
	(blue)	18.01	17.54	15.41	14.83	13.90 ^{+0.10} _{-0.10}	...
	(red)	15.32	15.34	15.16	14.90	13.90 ^{+0.10} _{-0.20}	...

Table 3—Continued

ID	Target	log N(0)	log N(1)	log N(2)	log N(3)	log N(4)	log N(5)	log N(6)	b (km s ⁻¹)
93	HD 166716 ^c	19.95 ^{+0.10} _{-0.10}	19.90 ^{+0.10} _{-0.10}	15.65 ^{+0.13} _{-0.13}	15.18 ^{+0.08} _{-0.08}	< 14.10	...
94	HD 167402	19.90 ^{+0.10} _{-0.10}	19.74 ^{+0.10} _{-0.10}	15.63 ^{+0.04} _{-0.06}	15.42 ^{+0.04} _{-0.06}	14.60 ^{+0.04} _{-0.04}	14.37 ^{+0.08} _{-0.08}	< 14.00	15.7 ^{+2.5} _{-1.0}
95	HD 167659 ^b	20.13 ^{+0.10} _{-0.10}	20.34 ^{+0.10} _{-0.10}	17.59 ^{+0.44} _{-0.37}	17.62 ^{+0.27} _{-0.34}	16.01 ^{+0.22} _{-0.11}	15.30 ^{+0.15} _{-0.07}	13.98 ^{+0.10} _{-0.10}	...
	(blue)	15.73 ^{+0.07} _{-0.04}	15.48 ^{+0.17} _{-0.09}	14.64 ^{+0.27} _{-0.04}	14.28 ^{+0.16} _{-0.04}	...	8.4 ^{+0.9} _{-1.0}
	(red)	17.58 ^{+0.44} _{-0.38}	17.62 ^{+0.27} _{-0.34}	15.99 ^{+0.12} _{-0.12}	15.26 ^{+0.08} _{-0.08}	...	7.6 ^{+0.9} _{-1.0}
96	HD 167771	20.39 ^{+0.05} _{-0.05}	20.32 ^{+0.05} _{-0.05}	19.05 ^{+0.50} _{-0.50}	18.04 ^{+0.07} _{-0.14}	15.50 ^{+0.07} _{-0.06}	14.83 ^{+0.05} _{-0.04}	< 13.96	6.1 ^{+0.6} _{-2.0}
97	HD 167971 ^c	20.63 ^{+0.15} _{-0.15}	20.49 ^{+0.10} _{-0.10}	18.10 ^{+0.50} _{-0.50}	16.20 ^{+0.30} _{-0.30}	16.00 ^{+0.30} _{-0.20}	< 15.31	...	15.0 ^{+2.0} _{-2.0}
98	HD 168076 ^c	20.45 ^{+0.15} _{-0.15}	20.22 ^{+0.15} _{-0.15}	16.50 ^{+0.20} _{-0.20}	15.64 ^{+0.08} _{-0.08}	< 14.40	...
99	HD 168941	19.82 ^{+0.10} _{-0.10}	19.77 ^{+0.10} _{-0.10}	17.85 ^{+0.13} _{-0.15}	17.29 ^{+0.33} _{-0.46}	15.69 ^{+0.42} _{-0.42}	14.64 ^{+0.11} _{-0.11}	< 14.08	4.0 ^{+1.0} _{-1.4}
100	HD 172140	18.97 ^{+0.10} _{-0.10}	18.92 ^{+0.10} _{-0.10}	15.78 ^{+1.47} _{-0.29}	15.68 ^{+1.48} _{-0.28}	14.62 ^{+0.56} _{-0.07}	14.13 ^{+0.10} _{-0.04}	< 13.90	5.1 ^{+1.0} _{-2.5}
101	HD 175754	19.06 ^{+0.10} _{-0.10}	19.36 ^{+0.10} _{-0.10}	16.96 ^{+0.43} _{-0.35}	16.57 ^{+0.44} _{-0.37}	14.91 ^{+0.07} _{-0.04}	14.30 ^{+0.04} _{-0.04}	< 13.95	8.4 ^{+0.9} _{-1.0}
102	HD 175876 ^b	18.98 ^{+0.05} _{-0.05}	19.30 ^{+0.05} _{-0.05}	16.79 ^{+0.45} _{-0.30}	16.46 ^{+0.26} _{-0.13}	15.01 ^{+0.05} _{-0.03}	14.58 ^{+0.03} _{-0.03}	< 14.06	...
	(blue)	16.03	16.15	14.73	14.38	< 13.75	...
	(red)	16.71	16.16	14.69	14.16	< 13.75	...
103	HD 177989	19.93 ^{+0.10} _{-0.10}	19.67 ^{+0.10} _{-0.10}	17.64 ^{+0.13} _{-0.20}	17.26 ^{+0.25} _{-0.37}	15.39 ^{+0.31} _{-0.17}	14.58 ^{+0.06} _{-0.05}	< 13.85	4.4 ^{+0.8} _{-0.6}
104	HD 178487	20.18 ^{+0.10} _{-0.10}	20.16 ^{+0.10} _{-0.10}	18.16 ^{+0.16} _{-0.16}	17.75 ^{+0.28} _{-0.28}	15.41 ^{+0.20} _{-0.12}	14.66 ^{+0.10} _{-0.10}	< 14.06	7.2 ^{+1.0} _{-1.0}
105	HD 179406	20.41 ^{+0.10} _{-0.10}	20.21 ^{+0.10} _{-0.10}	18.09 ^{+0.14} _{-0.14}	17.12 ^{+0.55} _{-0.46}	15.25 ^{+0.41} _{-0.10}	14.50 ^{+0.09} _{-0.05}	< 14.10	5.5 ^{+1.0} _{-1.5}
106	HD 179407	19.88 ^{+0.10} _{-0.10}	19.94 ^{+0.10} _{-0.10}	18.25 ^{+0.10} _{-0.10}	17.98 ^{+0.17} _{-0.17}	16.33 ^{+0.93} _{-0.08}	14.83 ^{+0.30} _{-0.21}	< 14.00	5.5 ^{+1.0} _{-1.6}
107	HD 185418	20.23 ^{+0.10} _{-0.10}	20.53 ^{+0.10} _{-0.10}	18.37 ^{+0.07} _{-0.08}	17.43 ^{+0.29} _{-0.41}	15.56 ^{+1.15} _{-0.28}	14.53 ^{+0.21} _{-0.07}	< 13.90	4.1 ^{+0.9} _{-1.5}
108	HD 187459	20.12 ^{+0.10} _{-0.10}	20.06 ^{+0.10} _{-0.10}	17.56 ^{+0.33} _{-0.34}	17.23 ^{+0.38} _{-0.34}	15.41 ^{+0.12} _{-0.09}	14.84 ^{+0.05} _{-0.04}	< 13.78	9.7 ^{+0.9} _{-1.0}
109	HD 190429A	19.89 ^{+0.10} _{-0.10}	19.95 ^{+0.10} _{-0.10}	16.39 ^{+0.40} _{-0.40}	16.66 ^{+0.20} _{-0.20}	15.57 ^{+0.08} _{-0.07}	15.08 ^{+0.05} _{-0.04}	13.99 ^{+0.15} _{-0.15}	13.3 ^{+0.9} _{-1.0}
110	HD 190918	19.31 ^{+0.10} _{-0.10}	19.63 ^{+0.10} _{-0.10}	16.56 ^{+0.20} _{-0.27}	16.57 ^{+0.21} _{-0.31}	15.39 ^{+0.06} _{-0.06}	15.06 ^{+0.04} _{-0.04}	13.76 ^{+0.15} _{-0.15}	15.5 ^{+2.4} _{-1.0}
111	HD 191495	19.68 ^{+0.10} _{-0.10}	19.85 ^{+0.10} _{-0.10}	16.79 ^{+0.32} _{-0.32}	16.67 ^{+0.33} _{-0.33}	15.56 ^{+0.11} _{-0.09}	15.05 ^{+0.05} _{-0.04}	14.05 ^{+0.11} _{-0.11}	11.8 ^{+0.9} _{-1.0}
112	HD 191877	19.73 ^{+0.10} _{-0.10}	19.70 ^{+0.10} _{-0.10}	17.52 ^{+0.14} _{-0.36}	17.06 ^{+0.27} _{-0.43}	15.26 ^{+0.09} _{-0.09}	14.75 ^{+0.04} _{-0.04}	13.53 ^{+0.10} _{-0.10}	6.1 ^{+0.9} _{-0.6}
113	HD 192035	20.37 ^{+0.10} _{-0.10}	20.35 ^{+0.10} _{-0.10}	18.43 ^{+0.50} _{-0.50}	16.69 ^{+0.49} _{-0.41}	15.43 ^{+0.13} _{-0.09}	14.67 ^{+0.05} _{-0.04}	< 14.08	6.8 ^{+1.0} _{-1.0}
114	HD 192639	20.27 ^{+0.10} _{-0.10}	20.41 ^{+0.10} _{-0.10}	18.28 ^{+0.20} _{-0.20}	17.06 ^{+0.46} _{-0.48}	15.64 ^{+0.25} _{-0.15}	15.27 ^{+0.19} _{-0.12}	14.08 ^{+0.11} _{-0.11}	7.3 ^{+1.0} _{-1.0}
115	HD 195965	19.90 ^{+0.05} _{-0.05}	20.18 ^{+0.05} _{-0.05}	18.09 ^{+0.09} _{-0.15}	17.31 ^{+0.26} _{-0.41}	15.43 ^{+0.16} _{-0.12}	14.55 ^{+0.04} _{-0.04}	< 13.90	6.4 ^{+0.9} _{-0.7}
116	HD 199579	20.23 ^{+0.10} _{-0.10}	20.19 ^{+0.10} _{-0.10}	17.96 ^{+0.31} _{-0.30}	17.38 ^{+0.32} _{-0.27}	15.95 ^{+0.16} _{-0.10}	15.47 ^{+0.06} _{-0.05}	14.30 ^{+0.08} _{-0.08}	13.2 ^{+0.9} _{-1.0}
117	HD 201345	18.83 ^{+0.10} _{-0.10}	19.02 ^{+0.10} _{-0.10}	16.89 ^{+0.40} _{-0.39}	16.49 ^{+0.27} _{-0.27}	15.00 ^{+0.06} _{-0.06}	14.57 ^{+0.04} _{-0.04}	< 13.60	7.4 ^{+0.9} _{-1.1}
118	HD 201638	17.67 ^{+0.10} _{-0.10}	18.08 ^{+0.10} _{-0.10}	16.09 ^{+0.22} _{-0.22}	15.62 ^{+0.23} _{-0.13}	14.30 ^{+0.04} _{-0.04}	< 14.30	< 14.30	6.5 ^{+0.8} _{-0.9}
119	HD 203374A	20.32 ^{+0.10} _{-0.10}	20.42 ^{+0.10} _{-0.10}	18.09 ^{+0.24} _{-0.24}	17.24 ^{+0.37} _{-0.37}	15.22 ^{+0.09} _{-0.08}	14.71 ^{+0.04} _{-0.04}	< 14.00	8.0 ^{+0.9} _{-1.0}
120	HD 206267	20.65 ^{+0.10} _{-0.10}	20.52 ^{+0.10} _{-0.10}	18.17 ^{+0.25} _{-0.20}	17.43 ^{+0.63} _{-0.48}	15.93 ^{+1.22} _{-0.21}	15.21 ^{+1.10} _{-0.14}	14.03 ^{+0.11} _{-0.11}	5.7 ^{+1.0} _{-2.4}
121	HD 206773	20.05 ^{+0.05} _{-0.05}	20.22 ^{+0.05} _{-0.05}	18.10 ^{+0.07} _{-0.12}	17.35 ^{+0.18} _{-0.33}	15.44 ^{+0.08} _{-0.08}	14.70 ^{+0.04} _{-0.03}	13.62 ^{+0.15} _{-0.15}	5.7 ^{+0.7} _{-0.5}
122	HD 207198	20.61 ^{+0.10} _{-0.10}	20.43 ^{+0.10} _{-0.10}	18.42 ^{+0.08} _{-0.08}	17.63 ^{+0.20} _{-0.29}	16.65 ^{+0.64} _{-0.64}	16.68 ^{+0.11} _{-0.17}	14.04 ^{+0.11} _{-0.11}	3.8 ^{+1.0} _{-1.3}
123	HD 207308	20.52 ^{+0.10} _{-0.10}	20.38 ^{+0.10} _{-0.10}	18.28 ^{+0.13} _{-0.13}	17.03 ^{+0.73} _{-0.55}	15.35 ^{+0.79} _{-0.12}	14.77 ^{+0.11} _{-0.05}	< 14.30	5.2 ^{+1.0} _{-2.0}
124	HD 208440	19.94 ^{+0.05} _{-0.05}	20.00 ^{+0.05} _{-0.05}	17.73 ^{+0.20} _{-0.27}	17.26 ^{+0.34} _{-0.37}	15.37 ^{+0.08} _{-0.06}	14.91 ^{+0.05} _{-0.04}	< 14.30	8.1 ^{+0.9} _{-0.9}
125	HD 209339	19.80 ^{+0.05} _{-0.05}	19.97 ^{+0.05} _{-0.05}	17.19 ^{+0.43} _{-0.48}	16.44 ^{+0.54} _{-0.37}	15.15 ^{+0.14} _{-0.08}	14.69 ^{+0.07} _{-0.04}	< 14.10	6.8 ^{+1.0} _{-1.0}
126	HD 210809 ^b	19.54 ^{+0.05} _{-0.05}	19.74 ^{+0.05} _{-0.05}	16.36 ^{+0.40} _{-0.40}	16.46 ^{+0.40} _{-0.40}	15.56 ^{+0.03} _{-0.03}	15.09 ^{+0.03} _{-0.03}	14.15 ^{+0.06} _{-0.06}	5.0 ^{+1.0} _{-1.0}
	(blue)	14.72 ^{+0.06} _{-0.04}	14.33 ^{+0.04} _{-0.04}
	(red)	15.50 ^{+0.06} _{-0.05}	15.01 ^{+0.04} _{-0.04}
127	HD 210839	20.51 ^{+0.10} _{-0.10}	20.45 ^{+0.10} _{-0.10}	18.06 ^{+0.45} _{-0.43}	16.85 ^{+0.08} _{-0.29}	15.78 ^{+0.18} _{-0.10}	15.30 ^{+0.18} _{-0.10}	14.31 ^{+0.06} _{-0.06}	10.0 ^{+1.0} _{-1.0}
128	HD 216044	19.75 ^{+0.10} _{-0.10}	20.00 ^{+0.10} _{-0.10}	17.66 ^{+0.26} _{-0.31}	17.36 ^{+0.35} _{-0.35}	15.56 ^{+0.18} _{-0.12}	15.15 ^{+0.11} _{-0.08}	13.99 ^{+0.11} _{-0.11}	8.7 ^{+0.9} _{-1.0}
129	HD 216532 ^c	20.85 ^{+0.15} _{-0.15}	20.74 ^{+0.15} _{-0.15}	15.78 ^{+0.30} _{-0.11}	15.48 ^{+0.18} _{-0.08}	14.46 ^{+0.08} _{-0.08}	...
130	HD 216898	20.66 ^{+0.10} _{-0.10}	20.78 ^{+0.10} _{-0.10}	18.77 ^{+0.36} _{-0.36}	17.69 ^{+0.28} _{-0.31}	16.03 ^{+0.11} _{-0.07}	15.52 ^{+0.08} _{-0.06}	14.20 ^{+0.11} _{-0.11}	9.8 ^{+0.9} _{-1.0}
131	HD 217305	20.65 ^{+0.10} _{-0.10}	20.61 ^{+0.10} _{-0.10}	18.93 ^{+0.17} _{-0.17}	17.67 ^{+0.28} _{-0.33}	16.19 ^{+0.25} _{-0.14}	15.46 ^{+0.10} _{-0.07}	14.29 ^{+0.10} _{-0.10}	8.8 ^{+0.9} _{-1.0}
132	HD 217312	20.43 ^{+0.10} _{-0.10}	20.54 ^{+0.10} _{-0.10}	18.44 ^{+0.13} _{-0.13}	17.26 ^{+0.37} _{-0.37}	15.91 ^{+0.14} _{-0.11}	15.27 ^{+0.06} _{-0.08}	14.16 ^{+0.08} _{-0.08}	9.4 ^{+0.9} _{-1.0}
133	HD 218915	19.78 ^{+0.10} _{-0.10}	19.94 ^{+0.10} _{-0.10}	17.95 ^{+0.18} _{-0.30}	17.50 ^{+0.28} _{-0.37}	15.54 ^{+0.12} _{-0.10}	14.87 ^{+0.05} _{-0.05}	13.83 ^{+0.10} _{-0.10}	8.2 ^{+0.9} _{-0.9}
134	HD 224151 ^b	20.12 ^{+0.10} _{-0.10}	20.32 ^{+0.10} _{-0.10}	18.15 ^{+0.13} _{-0.22}	17.66 ^{+0.22} _{-0.35}	15.66 ^{+0.31} _{-0.16}	14.94 ^{+0.03} _{-0.03}	14.06 ^{+0.16} _{-0.16}	...
	(blue)	15.69 ^{+0.16} _{-0.09}	15.36 ^{+0.13} _{-0.07}	14.59 ^{+0.04} _{-0.04}	14.32 ^{+0.04} _{-0.04}	13.84 ^{+0.15} _{-0.15}	...
	(red)	18.15 ^{+0.13} _{-0.22}	17.66 ^{+0.22} _{-0.35}	15.62 ^{+0.32} _{-0.19}	14.82 ^{+0.09} _{-0.04}	13.64 ^{+0.18} _{-0.18}	...
135	HD 224257 ^b	19.44 ^{+0.10} _{-0.10}	19.81 ^{+0.10} _{-0.10}	16.22 ^{+0.44} _{-0.20}	15.94 ^{+0.41} _{-0.19}	14.94 ^{+0.03} _{-0.03}	14.77 ^{+0.03} _{-0.03}	< 14.20	...
	(blue)	16.12 ^{+0.48} _{-0.30}	15.83 ^{+0.46} _{-0.29}	14.46 ^{+0.04} _{-0.04}	14.31 ^{+0.04} _{-0.04}	< 13.90	6.4 ^{+1.0} _{-1.0}
	(red)	15.53 ^{+0.04} _{-0.04}	15.28 ^{+0.04} _{-0.04}	14.76 ^{+0.04} _{-0.04}	14.59 ^{+0.04} _{-0.04}	< 13.90	19.5 ^{+0.5} _{-1.0}
136	HD 224868	20.02 ^{+0.10} _{-0.10}	20.18 ^{+0.10} _{-0.10}	17.09 ^{+0.41} _{-0.33}	16.56 ^{+0.37} _{-0.26}	15.11 ^{+0.08} _{-0.06}			

Table 3—Continued

ID	Target	log N(0)	log N(1)	log N(2)	log N(3)	log N(4)	log N(5)	log N(6)	b (km s ⁻¹)
	(blue)	16.39 ^{+0.40} _{-0.32}	16.63 ^{+0.37} _{-0.28}	15.55 ^{+0.10} _{-0.08}	7.7 ^{+0.9} _{-0.9}
	(red)	15.86 ^{+0.19} _{-0.12}	15.63 ^{+0.07} _{-0.04}	15.21 ^{+0.04} _{-0.04}	11.5 ^{+1.0} _{-1.0}
138	HD 308813	19.97 ^{+0.10} _{-0.10}	20.00 ^{+0.10} _{-0.10}	18.05 ^{+0.16} _{-0.17}	17.42 ^{+0.31} _{-0.36}	15.07 ^{+0.13} _{-0.06}	14.48 ^{+0.13} _{-0.13}	< 13.95	7.8 ^{+0.9} _{-1.0}
139	HD 332407	20.03 ^{+0.10} _{-0.10}	20.12 ^{+0.10} _{-0.10}	16.80 ^{+0.40} _{-0.40}	16.20 ^{+0.22} _{-0.14}	15.45 ^{+0.07} _{-0.06}	15.10 ^{+0.05} _{-0.04}	14.20 ^{+0.08} _{-0.08}	12.7 ^{+0.9} _{-1.0}

^aColumn densities, $N(J)$ (in cm⁻²), in rotational states J derived from curve-of-growth fitting with Doppler parameter (b in last column) and damping wings for lines from $J = 0$ and $J = 1$. No value is listed when b was poorly determined. Error bars on low- J states ($J = 0, 1$ and sometimes $J = 2, 3$) depend on data quality (see footnote in Table 3). In damping-wing fits, errors on log N typically range from ± 0.03 to ± 0.10 . Six targets had detectable column densities in $J = 7$: #48 with log $N(7) = 15.54 \pm 0.15$, #52 with log $N(7) = 14.47 \pm 0.05$, #88 with log $N(7) = 14.14 \pm 0.06$, #116 with log $N(7) = 14.29 \pm 0.11$, #127 with log $N(7) = 14.25 \pm 0.05$, and #137 with log $N(7) = 15.43 \pm 0.15$ (15.32 in blue component and 14.80 in red component).

^bIn 15 sight lines, multiple velocity components were observable and measured in high- J states. We report individual column densities, denoted as “blue and red” components, and sum them to find total column densities.

^cA few targets have no listed column densities $N(2)$ or $N(3)$. In several cases this was a result of poor data quality, so that lines from $J \geq 2$ could not be fitted accurately. In other cases, the accessible (unblocked) lines from $J = 2$ and $J = 3$ were highly saturated, with equivalent widths of 200-300 mÅ and large effective Doppler parameters ($b \geq 10$ km s⁻¹) likely produced by unresolved velocity components. When equivalent widths of all the accessible lines lie on the “flat portion” of the curve of growth, errors can exceed ± 0.40 for log $N = 16-17$ and ± 0.50 for log $N = 17-19$.

Table 4. Column Densities^a and Rotational Temperatures^b

ID	Target	$\log N_{\text{H}_2}$	T_{01} (K)	T_{02} (K)	T_{24} (K)	T_{35} (K)	$\log N_{\text{HI}}^c$	$\log N_{\text{H}}^c$	D_{phot}^d (kpc)	$\langle n_{\text{H}} \rangle^d$ (cm^{-3})	$f_{\text{H}_2}^d$	Notes ^a
1	BD 35°4258	19.56	125	125	222	247	21.24	21.26	2.51	0.22	0.040	2
2	BD 53°2820	20.04	107	52	473	590	21.35	21.39	4.27	0.17	0.089	2
3	CPD –59°2600	20.16	81	57	274	381	21.54	21.57	2.11	0.57	0.077	2
4	CPD –59°2603	20.13	87	99	141	595	21.43	21.47	2.60	0.37	0.091	1
5	CPD –69°1743	19.91	101	50	376	491	21.16	21.21	4.47	0.36	0.101	2
6	CPD –72°1184	20.07	115	73	173	...	20.90	21.01	9.85	0.034	0.228	2
7	HD 3827	17.48	159	159	274	348	20.55	20.55	1.88	0.061	0.0017	1
8	HD 5005A	20.22	86	92	172	277	21.40	21.45	2.89	1.03	0.117	1
9	HD 12323	20.31	93	85	181	236	21.19	21.29	3.04	0.21	0.209	2
10	HD 13268	20.47	111	85	181	288	21.34	21.44	2.80	0.32	0.212	2
11	HD 13745	20.59	75	98	156	260	21.34	21.47	2.81	0.34	0.262	2
12	HD 14434	20.54	117	123	141	303	21.45	21.55	2.98	0.39	0.197	2
13	HD 15137	20.27	119	76	215	274	21.24	21.32	3.00	0.23	0.176	1
14	HD 15558A	20.89	93	103	142	290	21.52	21.69	1.91	0.83	0.319	3
15	HD 15642	20.33	159	331	118	187	21.23	21.33	3.89	0.18	0.201	2
16	HD 34656	20.19	94	66	209	276	21.22*	21.29	1.99	0.32	0.157	1
17	HD 39680	19.53	90	73	148	273	21.30	21.31	2.67	0.25	0.033	1
18	HD 41161	20.02	96	81	178	221	21.01	21.09	1.16	0.34	0.170	3
19	HD 42088	20.51	82	71	190	257	21.15	21.31	1.97	0.34	0.314	1
20	HD 45314	20.60	89	77	158	204	21.04	21.28	0.80	0.77	0.421	1
21	HD 46150	20.64	97	55	273	383	21.26	21.43	1.47	0.59	0.324	1
22	HD 47360	20.38	88	74	192	329	21.46	21.53	1.24	0.89	0.143	2
23	HD 47417	20.52	89	71	188	243	21.13	21.30	1.23	0.53	0.329	1
24	HD 60369	20.48	67	74	187	219	21.26	21.38	2.54	0.31	0.249	1
25	HD 61347	20.60	81	99	145	237	21.53	21.62	4.44	0.30	0.190	2
26	HD 62866	20.24	104	58	329	426	21.23*	21.31	3.51	0.19	0.170	2
27	HD 63005	20.15	111	84	184	244	21.24	21.31	4.35	0.15	0.140	2
28	HD 64568	20.54	61	51	321	370	21.16*	21.33	5.75	0.12	0.324	2
29	HD 66695	20.11	75	96	208	277	21.12*	21.20	4.25	0.12	0.163	2
30	HD 66788	19.72	86	136	159	171	21.23	21.26	4.72	0.12	0.058	1
31	HD 69106	19.73	80	95	192	193	21.07	21.11	1.10	0.38	0.084	2
32	HD 73882	21.13	53	44	293	676	21.11	21.60	0.83	1.55	0.677	3
33	HD 74194	20.55	97	79	178	257	21.23*	21.38	2.25	0.35	0.295	2
34	HD 74920	20.26	117	55	306	390	21.15	21.25	2.05	0.28	0.205	1
35	HD 89137	19.99	110	54	304	400	21.03	21.10	4.04	0.10	0.154	1
36	HD 90087	19.91	92	83	206	284	21.19	21.23	2.52	0.22	0.095	1
37	HD 91597	19.70	69	56	378	463	21.40	21.42	4.29	0.20	0.038	2
38	HD 91651	19.07	82	72	412	400	21.15	21.16	3.98	0.12	0.016	1
39	HD 91824	19.83	65	86	186	237	21.12	21.22	2.75	0.20	0.204	1
40	HD 92554	18.93	40	61	419	519	21.34	21.34	6.61	0.11	0.0077	2
41	HD 93028	19.55	111	58	336	379	20.95	20.98	2.97	0.10	0.074	2
42	HD 93129A	20.21	129	76	254	238	21.47	21.52	2.21	0.49	0.099	2
43	HD 93146A	19.71	82	54	355	457	21.18	21.21	2.30	0.23	0.063	2
44	HD 93204	19.81	105	56	338	413	21.41	21.43	2.73	0.32	0.048	1
45	HD 93205	19.79	110	62	282	341	21.36	21.38	2.44	0.32	0.051	1
46	HD 93206	19.52	84	55	309	345	21.34	21.35	1.48	0.49	0.029	1
47	HD 93222	19.77	74	50	378	450	21.47	21.49	2.47	0.41	0.038	1
48	HD 93250	20.27	115	54	582	656	21.39	21.45	2.20	0.41	0.132	1
49	HD 93843	19.61	111	58	313	390	21.30	21.32	2.85	0.24	0.039	1
50	HD 96670	20.59	71	90	166	341	21.28*	21.43	2.67	0.33	0.290	2
51	HD 96715	20.62	57	85	163	256	21.20	21.38	3.15	0.25	0.345	2
52	HD 96917	20.25	64	21.23	21.31	2.46	0.27	0.173	2
53	HD 97471	19.90	67	69	245	299	21.20*	21.24	2.78	0.20	0.091	2
54	HD 97913	20.13	90	63	269	329	21.20*	21.27	2.52	0.24	0.145	2

Table 4—Continued

ID	Target	$\log N_{\text{H}_2}$	T_{01} (K)	T_{02} (K)	T_{24} (K)	T_{35} (K)	$\log N_{\text{HI}}^c$	$\log N_{\text{H}}^c$	D_{phot}^d (kpc)	$\langle n_{\text{H}} \rangle^d$ (cm^{-3})	$f_{\text{H}_2}^d$	Notes ^a
55	HD 99857	20.26	88	92	150	184	21.27	21.35	3.04	0.24	0.163	2
56	HD 99890	19.47	91	75	244	282	21.12	21.14	3.22	0.14	0.043	2
57	HD 100199	20.17	98	65	198	253	21.18	21.26	2.77	0.21	0.163	2
58	HD 100213	20.42	79	86	162	205	21.18	21.33	2.15	0.32	0.285	2
59	HD 100276	19.83	85	59	313	554	21.19	21.23	2.94	0.19	0.080	2
60	HD 101131	20.28	87	88	164	196	21.15*	21.25	1.78	0.32	0.212	1
61	HD 101190	20.42	64	86	149	181	21.15	21.35	2.09	0.35	0.232	1
62	HD 101205	20.26	79	103	155	181	21.24	21.29	1.64	0.39	0.187	3
63	HD 101298	20.45	65	56	259	180	21.26	21.28	2.58	0.24	0.237	2
64	HD 101413	20.51	63	98	143	200	21.23	21.37	2.13	0.36	0.276	2
65	HD 101436	20.54	61	88	155	197	21.23	21.28	1.85	0.33	0.290	1
66	HD 103779	19.82	117	59	300	507	21.17	21.21	3.99	0.13	0.082	2
67	HD 104705	19.99	98	92	175	214	21.15	21.21	4.18	0.13	0.122	1
68	HD 115071	20.64	84	82	254	304	21.39	21.42	1.87	0.46	0.262	2
69	HD 116781	20.06	119	94	172	206	21.21	21.27	1.79	0.34	0.124	2
70	HD 116852	19.78	74	53	317	322	20.96	21.01	4.88	0.068	0.117	1
71	HD 118571	20.44	94	86	172	193	20.98*	21.18	2.70	0.18	0.366	1
72	HD 124314A	20.47	77	78	185	265	21.41	21.50	1.25	0.82	0.187	1
73	HD 124979	20.41	93	88	172	230	21.27	21.30	3.09	0.21	0.258	2
74	HD 148422	20.13	63	21.24	21.30	8.26	0.078	0.134	3
75	HD 152218	20.57	69	82	185	253	21.34	21.47	1.42	0.67	0.254	2
76	HD 152233	20.29	73	92	311	222	21.29	21.37	1.52	0.50	0.167	2
77	HD 152248	20.29	73	95	285	217	21.27*	21.44	1.61	0.55	0.143	2
78	HD 152314	20.51	68	21.35*	21.46	1.44	0.65	0.224	2
79	HD 152623	20.21	82	55	325	381	21.28	21.35	1.04	0.70	0.145	2
80	HD 152723	20.29	79	87	176	203	21.43	21.49	1.94	0.52	0.127	2
81	HD 153426	20.30	93	77	195	264	21.34	21.41	1.83	0.46	0.154	2
82	HD 154368	21.17	55	21.00	21.60	1.08	1.20	0.747	3
83	HD 156292	20.81	94	72	180	345	21.29*	21.51	1.51	0.69	0.398	2
84	HD 157857	20.62	78	88	150	207	21.30	21.45	2.56	0.36	0.295	2
85	HD 158661	20.17	73	99	192	265	21.28*	21.34	4.08	0.17	0.134	2
86	HD 161807	19.86	121	95	171	213	21.08*	21.13	1.94	0.23	0.108	1
87	HD 163758	19.86	80	96	215	219	21.23	21.27	4.11	0.15	0.079	2
88	HD 163892	20.58	62	69	230	319	21.32	21.46	1.37	0.68	0.267	2
89	HD 164816	20.00	78	78	177	239	21.18	21.23	1.08	0.51	0.117	2
90	HD 165052	20.20	99	83	187	213	21.36	21.42	1.37	0.62	0.122	1
91	HD 165246	20.16	83	45	429	503	21.41	21.46	1.38	0.68	0.101	2
92	HD 166546	20.32	83	82	191	252	21.19*	21.29	1.46	0.43	0.212	2
93	HD 166716	20.23	74	21.27*	21.34	2.73	0.26	0.154	2
94	HD 167402	20.13	66	45	396	519	21.13	21.21	7.61	0.069	0.167	2
95	HD 167659	20.55	99	68	277	257	21.30	21.43	1.87	0.47	0.262	2
96	HD 167771	20.67	72	109	134	190	21.08	21.33	1.40	0.49	0.438	1
97	HD 167971	20.87	68	69	152	...	21.60	21.74	1.42	1.25	0.271	3
98	HD 168076	20.65	63	21.65	21.73	1.97	0.88	0.167	3
99	HD 168941	20.10	74	83	211	227	21.18	21.25	3.72	0.15	0.143	2
100	HD 172140	19.25	74	57	360	370	21.11	21.12	6.54	0.065	0.027	2
101	HD 175754	19.54	113	79	221	262	21.04	21.07	2.55	0.15	0.059	2
102	HD 175876	19.47	117	77	250	311	21.04	21.06	2.57	0.14	0.051	1
103	HD 177989	20.12	61	74	203	225	20.99	21.09	5.14	0.078	0.202	2
104	HD 178487	20.47	76	81	169	197	21.22	21.35	5.22	0.14	0.262	2
105	HD 179406	20.62	64	73	164	230	21.23	21.40	0.21	3.88	0.329	2
106	HD 179407	20.22	83	95	234	193	21.20	21.28	7.72	0.080	0.173	2
107	HD 185418	20.71	113	87	166	209	21.19	21.41	0.78	1.07	0.398	2
108	HD 187459	20.39	73	68	212	250	21.31*	21.40	1.68	0.48	0.194	2

Table 4—Continued

ID	Target	$\log N_{\text{H}_2}$	T_{01} (K)	T_{02} (K)	T_{24} (K)	T_{35} (K)	$\log N_{\text{HI}}^{\text{c}}$	$\log N_{\text{H}}^{\text{c}}$	$D_{\text{phot}}^{\text{d}}$ (kpc)	$\langle n_{\text{H}} \rangle^{\text{d}}$ (cm^{-3})	$f_{\text{H}_2}^{\text{d}}$	Notes ^a
109	HD 190429A	20.22	83	53	473	364	21.33*	21.39	2.38	0.33	0.134	2
110	HD 190918	19.80	117	64	357	379	21.40	21.42	2.39	0.36	0.048	2
111	HD 191495	20.07	94	62	343	356	21.32*	21.37	1.69	0.45	0.101	2
112	HD 191877	20.02	75	76	202	258	21.03	21.11	2.07	0.20	0.163	2
113	HD 192035	20.66	76	84	156	292	21.20	21.40	2.29	0.36	0.366	2
114	HD 192639	20.65	91	82	176	326	21.32	21.47	2.14	0.45	0.300	2
115	HD 195965	20.37	110	88	175	219	20.92	21.11	1.03	0.41	0.360	1
116	HD 199579	20.51	74	75	225	307	21.04	21.24	0.92	0.61	0.371	2
117	HD 201345	19.24	97	84	237	306	21.00	21.01	2.50	0.13	0.034	2
118	HD 201638	18.23	136	97	249	...	20.80*	20.80	8.98	0.023	0.0054	2
119	HD 203374A	20.68	87	76	163	237	21.20	21.41	0.78	1.07	0.377	2
120	HD 206267	20.89	68	70	204	268	21.22	21.51	0.73	1.44	0.483	2
121	HD 206773	20.45	94	84	175	227	21.09	21.24	0.69	0.82	0.314	1
122	HD 207198	20.83	65	77	251	564	21.28	21.51	1.04	1.01	0.415	2
123	HD 207308	20.76	68	75	160	263	21.20	21.44	0.76	1.17	0.421	2
124	HD 208440	20.27	83	76	195	254	21.24	21.32	1.04	0.65	0.176	1
125	HD 209339	20.19	94	67	222	332	21.20	21.28	1.08	0.57	0.163	1
126	HD 210809	19.95	98	57	482	413	21.31	21.35	3.88	0.18	0.080	1
127	HD 210839	20.78	73	70	201	370	21.24	21.47	0.87	1.21	0.409	2
128	HD 216044	20.20	105	79	216	269	21.28*	21.35	2.57	0.28	0.123	2
129	HD 216532	21.10	70	21.38*	21.69	0.94	1.69	0.512	3
130	HD 216898	21.03	89	86	170	273	21.44*	21.65	0.91	1.59	0.438	2
131	HD 217035	20.94	74	92	170	269	21.46	21.67	0.72	2.10	0.377	2
132	HD 217312	20.79	88	82	183	296	21.48	21.63	0.60	2.30	0.290	2
133	HD 218915	20.17	93	88	191	229	21.20	21.27	3.62	0.17	0.157	2
134	HD 224151	20.53	98	83	185	222	21.35	21.46	0.91	1.03	0.232	2
135	HD 224257	19.96	127	57	332	473	21.08*	21.14	2.05	0.22	0.132	2
136	HD 224868	20.41	93	61	228	304	21.16*	21.29	3.03	0.21	0.262	2
137	HD 303308	20.23	131	68	569	1358	21.41	21.46	2.66	0.35	0.117	2
138	HD 308813	20.29	80	85	157	206	21.20	21.30	3.45	0.19	0.197	2
139	HD 332407	20.38	86	56	317	499	21.24	21.35	2.56	0.28	0.216	2

^aAll column densities, N_{H_2} , N_{HI} , and $N_{\text{H}} = N_{\text{HI}} + 2N_{\text{H}_2}$ are in cm^{-2} , with errors on $\log N_{\text{HI}}$ discussed in Table 2 and Section 3.2. Values of $N(0)$ and $N(1)$ come from fitting damping-wing Voigt profiles of R(0), R(1), and P(1) lines. Their errors depend on data quality. Notes in last column refer to three levels of S/N ratio: (1) $S/N \geq 15$ with errors of $\pm 0.03 - 0.05$ on $\log N$; (2) $5 \leq S/N \leq 15$ with errors of $\pm 0.05 - 0.10$; (3) $S/N \leq 5$, with errors of $\pm 0.10 - 0.20$.

^bThe rotational excitation temperature T_{01} is determined from the ratio N_1/N_0 of column densities of the $J = 1$ and $J = 0$ rotational states. Similar excitation temperatures T_{02} , T_{24} and T_{35} follow from ratios N_2/N_0 , N_4/N_2 , and N_5/N_3 of populations in levels $J = 0, 2, 4$ (para- H_2) and $J = 3, 5$ (ortho- H_2) respectively, as described in Sections 3.4 and 3.5.

^cNeutral hydrogen column densities N_{HI} are taken from previous surveys by Diplás & Savage (1994), Jenkins (2019), Fitzpatrick & Massa (1990), and several individual papers. Details are discussed in Section 2.1 and Table 2. For 26 sight lines with no Ly α fits, labeled with asterisks after $\log N_{\text{HI}}$, we use the relation, $N_{\text{H}} = (5.8 \times 10^{21} \text{ cm}^{-2} \text{ mag}^{-1}) E(B - V)$ from the *Copernicus* survey (Savage et al. 1977), with $N_{\text{HI}} = N_{\text{H}} - 2N_{\text{H}_2}$. Updated values of color excess $E(B - V)$ for all 139 target stars are listed in Table 1, taken from Shull & Danforth (2019).

^dMean total hydrogen density along each sight line, $\langle n_{\text{H}} \rangle = N_{\text{H}}/D_{\text{phot}}$, is estimated from stellar photometric distances D_{phot} in Table 1. The molecular fraction is defined by $f_{\text{H}_2} = 2N_{\text{H}_2}/[N_{\text{HI}} + 2N_{\text{H}_2}]$.

Table 5. Observational Averages from *FUSE* Survey^a

Quantity	Units	$D \leq 2$ kpc	$D \leq 5$ kpc	All
Sample	# Stars	56	129	138
$\langle D \rangle$	kpc	1.31	2.27	2.62
$\langle n_{\text{HI}} \rangle$	cm^{-3}	0.553	0.364	0.344
$\langle n_{\text{H}_2} \rangle$	cm^{-3}	0.261	0.136	0.129
$\langle n_{\text{H}} \rangle$	cm^{-3}	0.814	0.500	0.472
$\langle f_{\text{H}_2} \rangle$...	0.268	0.202	0.200
$\langle E(B - V)/D \rangle$	mag kpc ⁻¹	0.434	0.260	0.246
$\langle N_{\text{H}}/E(B - V) \rangle$	cm ⁻² mag ⁻¹	6.00×10^{21}	6.06×10^{21}	6.07×10^{21}

^aMean values of total hydrogen density, $n_{\text{H}} = N_{\text{H}}/D_{\text{phot}}$, and molecular fraction f_{H_2} along the sightlines for stars in the full *FUSE* survey and for sub-samples within two photometric distance limits (Shull & Danforth 2019). The averages are column density-weighted (see Section 3.1). Column 3 is for 56 stars with $D_{\text{phot}} \leq 2$ kpc, Column 4 is for 129 stars with $D_{\text{phot}} \leq 5$ kpc, and Column 5 is for the full sample, omitting HD 3827 (uncertain $E(B - V)$). Statistics for $N_{\text{H}}/E(B - V)$ omit 26 stars without Ly α profile fits for H I.